2009

Inversion-based feedforward-feedback control: theory and implementation to high-speed atomic force microscope imaging

Ying Wu
Iowa State University

Inversion-based feedforward-feedback control:

theory and implementation to high-speed atomic force microscope imaging

by

Ying Wu

A dissertation submitted to the graduate faculty

in partial fulfillment of the requirements for the degree of

DOCTOR OF PHILOSOPHY

Major: Mechanical Engineering

Program of Study Committee:
Qingze Zou, Major Professor
Atul Kelkar
Sriram Sundararajan
Murti V. Salapaka
Ping Lu

Iowa State University

Ames, Iowa

2009

DEDICATION

To my husband Yuan Li, and my parents,

for their trust, support, encouragement, and love.

TABLE OF CONTENTS

LIST OF TABLES

LIST OF FIGURES

ACKNOWLEDGEMENTS

I would like to take this opportunity to express my thanks to those who helped me with various aspects of conducting research and the writing of dissertation.

I have been very fortunate to have Dr. Zou as my major professor and be his first student. I would like to thank him for his guidance, support and encouragement. During my research, I experienced joy and small successes, as well as failures and frustrations. Dr. Zou has been always there to help and give advices. Without his patience and support, I could not overcome so many crisis situations and finish this dissertation.

I was also fortunate to have other remarkable teachers like Dr. Murti V. Salapaka and Dr. Sriram Sundararajan. I learned a lot from Dr. Salapaka's linear and robust control courses, which inspired my work reported in Chapter 3 of this dissertation. I am indebted to him for his guidance and help.

I would like to particularly thank Dr. Atul Kelkar, Dr. Ping Lu, along with Dr. Murti V. Salapaka and Dr. Sriram Sundararajan, for being in my committee and for their efforts and contributions to this work.

Dr. Chanmin Su, an outstanding researcher in Veeco Instrument Inc., gave me a lot of practical advices. I would like to thank him and his colleagues at Veeco Instrument Inc. for their support during my internship. In particular, I would like to thank Jian Shi, who worked with me on coupling correction for several months, for his suggestions and help. Even short, it is

fun and great working with him.

Many friends have helped me through these years. Their support and care helped me to stay focused on my graduate study. Especially, I would like to thank Hui Wang and Jia Wang, for their kindness help, in my difficult time.

Finally I would like to thank my parents and my husband for all their love and unconditional support. To them I dedicate this thesis.

ABSTRACT

In this dissertation, a suite of inversion-based feedforward-feedback control techniques are developed and applied to achieve high speed AFM imaging. In the last decade, great efforts have been made in developing the inversion-based feedforward control as an effective approach for precision output tracking. Such efforts are facilitated by the fruitful results obtained in the stable-inversion theory, including, mainly, the bounded inverse of nonminimum-phase systems, the preview-based inversion method that quantified the effect of the future desired trajectory on the inverse input, the consideration of the model uncertainties in the system inverse, and the integration of inversion with feedback and iterative control. However, challenges still exist in those inversion-based approaches. For example, although it has been shown that the inversion-based iterative control (IIC) technique can effectively compensate for the vibrational dynamics during the output tracking in the repetitive applications, however, compensating-for both the hysteresis effect and the dynamics effect simultaneously using the IIC approach has not been established yet. Moreover, the current design of the inversion-based feedforward-feedback two-degree-of-freedom (2DOF) controller is ad-hoc, and the minimization of the model uncertainty effects on the feedforward control has not been addressed. Furthermore, although it is possible to combine system inversion with both iterative learning and feedback control in the so-called current cycle feedback iterative learning control (CCF-ILC) approach, the current controller design is limited to be casual and the use of such CCF-ILC approach for rejecting slowly varying periodic disturbance has not been explored. These challenges, as magnified in applications such as high-speed AFM imaging, motivate the research of this dissertation. Particularly, it is shown that the IIC approach can effectively compensate for both the hysteresis and vibrational dynamics effects of smart actuators. The convergence of

the IIC algorithm is investigated by capturing the input-output behavior of piezo actuators with a cascade model consisting of a rate-independent hysteresis at the input followed by the dynamics part of the system. The size of the hysteresis and the vibrational dynamics variations that can be compensated for (by using the IIC method) has been quantified. Secondly, a novel robust-inversion has been developed for single-input-single-output (SISO) LTI systems, which minimized the dynamics uncertainty effect and obtained a guaranteed tracking performance for bounded dynamics uncertainties. Based on the robust-inversion approach, a systematic design of inversion-based two-degree-of-freedom (2DOF)-control was developed. Finally, the robust-inversion-based current cycle feedback iterative learning control approach was developed for the rejection of slow varying periodic disturbances. The proposed CCF-ILC controller design utilizes the recently-developed robust-inversion technique to minimize the model uncertainty effect on the feedforward control, as well as to remove the causality constraints in other CCF-ILC approaches. It is shown that the iterative law converges, and attains a bounded tracking error upon noise and disturbances. In this dissertation, these techniques have been successfully implemented to achieve high-speed AFM imaging of large-size samples. Specifically, it is shown that precision positioning of the probe in the AFM lateral (x-y) scanning can be successfully achieved by using the inversion-based iterative-control (IIC) techniques and robust-inversion-based 2DOF control design approach. The AFM imaging speed as well as the sample estimation can be substantially improved by using the CCF-ILC approach for the precision positioning of the probe in the vertical direction.

CHAPTER 1. Introduction

In the last decade, great efforts have been made in developing the inversion-based feedforward control as an effective approach for precision output tracking. Such efforts are facilitated by the fruitful results obtained in the stable-inversion theory, including, mainly, the bounded inverse of nonminimum-phase systems, the preview-based inversion method that quantified the effect of the future desired trajectory on the inverse input, the consideration of the model uncertainties in the system inverse, and the integration of inversion with feedback and iterative control. However, challenges still exist in those inversion-based approaches.

For example, it is shown that the inversion-based iterative control (IIC) technique can effectively compensate for the vibrational dynamics during the output tracking in the repetitive applications and it was successfully utilized for the precision positioning of piezo actuator with small displacement range [1, 2]. However, there exists nonlinear hysteresis during the large range operation of piezo actuator and compensating-for both hysteresis effect and the dynamics effect simultaneously using the IIC approach has not been established yet.

System inversion can also be utilized in feedforward-feedback two-degree-of-freedom (2DOF) system for output tracking. It is noted that the development of the stable inversion methodology [5, 6] has demonstrated the efficacy of combining the inversion-based feedforward control and feedback control in output tracking (e.g., [7]). The performance of the inverse feedforward control, however, can be limited by system dynamics uncertainties and disturbances [8], and the dynamics uncertainty effect has not been explicitly addressed in existing system inversion methods [5, 9, 7]. Moreover, existing 2DOF approach design feedforward and feedback

controllers separately and a systematic approach is sought to design the feedback control to complement the inversion-based feedforward control.

By combining system inversion with both iterative learning and feedback control, the so-called current cycle feedback iterative learning control (CCF-ILC) approach can be utilized for disturbance rejection. In the CCF-ILC framework, the iterative control input is generated online by using the tracking results from the previous iteration (i.e., previous cycle), and is augmented to the feedback control input during the current iteration (i.e., current cycle, called "current-cycle-feedback" as in literature [10]). The convergence of CCF-ILC approach was proved when the disturbance is repetitive. It is noted that, for the slow varying periodic disturbance, this feedforward feedback control framework can also improve tracking when the cycle-to-cycle variation is small. However, the convergence of the approach was not explored for slow varying periodic disturbance, and the allowable cycle-to-cycle variation for the tracking enhancement was not quantified. Moreover, in the existing CCF-ILC design, since the feedforward controller is limited to be causal, the constraints posed by the nonminimum-phase dynamics cannot be overcomed.

These challenges as magnified in applications of high-speed AFM imaging, motivate the research work of this dissertation.

The rest of this dissertation is organized as follows.

In Chapter 2,the inversion-based iterative control (IIC) technique was utilized to compensate for both the hysteresis and vibrational dynamics effects of piezo actuators. The convergence of the IIC algorithm is investigated by capturing the input-output behavior of piezo actuators with a cascade model consisting of a rate-independent hysteresis at the input followed by the dynamics part of the system. The size of the hysteresis and the vibrational dynamics variations that can be compensated for (by using the IIC method) is quantified. The IIC approach is il-

lustrated through experiments on a piezotube actuator used for positioning on an AFM system.

A novel robust-inversion-based two-degree-of-freedom (2DOF)-control approach for output tracking is developed in Chapter 3. A robust-system-inversion based approach is proposed to directly account for and minimize the dynamics uncertainty effect when finding the feedforward controller. Therefore, a guaranteed tracking performance was achieved for bounded dynamics uncertainties. Then this quantified bound of the tracking error is utilized in designing robust feedback controller to complement the feedforward control. Based on the concept of Bode's integral, it is shown that the feedback bandwidth can be improved from that obtained by using feedback alone. The proposed approach is also illustrated by implementing it in experiments on a piezotube actuator of an atomic force microscope for precision positioning.

Then in chapter 4 and 5, we proposed a novel current cycle feedback (CCF) iterative learning control (ILC) approach to achieve high-speed imaging in the vertical z-axis direction on atomic force microscope (AFM). The proposed CCF-ILC approach aims at achieving high-speed imaging of relatively-smooth samples, where the sample variation from one scanline to the next is relatively small. The idea is to use the proposed CCF-ILC approach to repetitively image on the first scanline, then apply the converged input to image the rest of scanlines without iteration, thereby achieving high-speed imaging. Chapter 4 – as the first step – is to show that the CCF-ILC controller can achieve precision tracking of the sample profile on one scanline. It is shown in Chapter 4 that the iterative law converges, and attains a bounded tracking error upon noise and disturbances without line-to-line sample variation. Then in Chapter 5, we extend this CCF-ILC approach to the entire imaging of samples. The main contribution of the chapter is the analysis and the use of the CCF-ILC approach for tracking sample profiles with variations between scanlines (called line-to-line sample variations). The convergence (stability) of the CCF-ILC system is analyzed for the general case where the line-to-line sample variation occurs at each iteration. The allowable line-to-line sample profile variation is quantified. The performance improvement of the CCF-ILC is discussed by comparing the tracking error of the

CCF-ILC technique to that of using feedback control alone. The proposed CCF-ILC control approach is illustrated by implementing it to the z-axis direction control in AFM imaging. Experimental results show that the imaging speed can be significantly increased by using the proposed approach.

The dissertation is concluded in Chapter 6.

CHAPTER 2. Iterative control approach to compensate for the hysteresis and the vibrational dynamics effects of piezo actuators

A paper published in IEEE Transactions on Control Systems Technology

Ying Wu [1] and Qingze Zou [2]

Abstract

In this chapter, the compensation for both the nonlinear hysteresis and the vibrational dynamics effects of piezo actuators is studied. Piezo actuators are the enabling device in many applications such as atomic force microscopy (AFM) to provide nano- to atomic-levels precision positioning. During high-speed, large-range positioning, however, large positioning errors can be generated due to the combined hysteresis and dynamics effects of piezo actuators, making it challenging to achieve precision positioning. The main contribution of this chapter is the use of an inversion-based iterative control (IIC) technique to compensate for both the hysteresis and vibrational dynamics effects of piezo actuators. The convergence of the IIC algorithm is investigated by capturing the input-output behavior of piezo actuators with a cascade model consisting of a rate-independent hysteresis at the input followed by the dynamics part of the system. The size of the hysteresis and the vibrational dynamics variations that can be compensated for (by using the IIC method) is quantified. The IIC approach is illustrated through experiments on a piezotube actuator used for positioning on an AFM system. Experimental results show that high-speed, large-range precision positioning can be achieved by using the proposed IIC technique. Furthermore, the proposed IIC algorithm is also applied to experi-

[1]Primary researcher and author
[2]Corresponding author

mentally validate the cascade model and the rate-independence of the hysteresis effect of the piezo actuator.

2.1 Introduction

This chapter studies the compensation for both the hysteresis and the vibrational dynamics effects of piezo actuators during high-speed, large-range, periodic motions. Piezo actuators are the enabling device to provide nano- to atomic-levels precision positioning in systems such as atomic force microscope (AFM) (e.g., to position the AFM-probe relative to the sample during the imaging process, e.g., [11]). However, during high-speed, large-range positioning, the positioning precision is complicated by the nonlinear hysteresis behavior [3, 12] and the linear vibrational dynamics (e.g., [3, 7]) of piezo actuators, resulting in large positioning errors. It is challenging, however, to compensate-for both hysteresis and vibrational dynamics effects of piezo actuators. The main contribution of this chapter is the use of an inversion-based iterative control (IIC) technique [1] to compensate for both the hysteresis and vibrational dynamics effects of piezo actuators. Convergence of the IIC technique is investigated and experimental results are presented to demonstrate that by using this technique, high-speed, large-range precision positioning of a piezo actuator can be achieved.

High-speed, large-range precision positioning of piezo actuators requires the compensation of both the hysteresis effect and the vibrational dynamics effects. *Smart materials* such as magnetostrictive, shape memory alloys, and piezoelectric ceramics [3, 13, 14] tend to present a nontrivial nonlinear hysteresis behavior in their input-output relation. As a result, positioning errors as large as 15% of the total displacement range can be generated [15]. Large positioning errors can also be generated in high-speed motion when the vibrational dynamics of piezo actuator is excited. Furthermore, during high-speed, large-range motions, both the hysteresis and the vibrational dynamics of smart materials will effect the positioning of piezo actuators, resulting in larger positioning errors (than under either effect alone) [7]. Large-range, high-speed precision positioning, however, is needed in applications such as the use of AFM to interrogate rapid biological processes like the migration of living cell [16], where the displacement range is

large (i.e., the cell size at $\sim$100 μm is close to the full displacement range of the piezoactuator), and the required scan speed is high. Therefore, there exist needs to account for both the hysteresis effect and the vibrational dynamics of piezo actuators.

These two adverse effects (hysteresis and dynamics) of piezo actuators can be compensated for by using control techniques, for example, the PID-type of control used on commercial AFM system. The low-gain margin of piezo actuators, however, limits the performance of the *ad hoc* PID-type of control in achieving high-speed positioning [7, 17, 18]. More advanced feedback control [7, 17, 19] can be used to alleviate such low gain margin limit and increase the bandwidth of the piezo positioning system. In feedback-based approaches, the hysteresis effect is treated as the *unknown disturbance* to the system, thereby *a priori* knowledge of the hysteresis effect was not explored. Whereas the inversion-type of feedforward approach [3, 12] explored such *a priori* knowledge of hysteresis by modeling the hysteresis effect and inverting it to obtain the control input to "cancel" the hysteresis effect. Such idea of inverse was also employed in the stable-inversion based technique [3, 20] to address the vibrational dynamics effect of piezo actuators. The successful implementation of these model-based inversion techniques, however, requires an accurate modeling (of the hysteresis or the vibrational dynamics), which is time-intensive and prone to errors. These modeling-related issues are avoided in the development of the iterative learning control (ILC). For example, recently, an ILC technique based on Preisach model approach [13, 4] was proposed to compensate for the hysteresis effect, while a dynamics inversion-based iteration control (IIC) algorithm [1, 2] was developed to tackle the vibrational dynamics effect. The ILC technique is particularly useful in applications involving *repetitive* operations, for example, the lateral scanning process during AFM imaging. Compensating-for *both* hysteresis effect and the dynamics effect simultaneously using the ILC approach, however, has not been established yet.

In this chapter, it is shown that the IIC technique [1, 2] can compensate-for both the nonlinear hysteresis and the linear dynamics effects of piezo actuators. We capture the input-output behavior of the piezo actuator by a cascade model which consists of a rate-independent, nonlinear-hysteresis at the input followed by the linear dynamics model. Then such a cascade model is

used to study the convergence of the IIC algorithm in L^2-norm, and accordingly, quantify the size of the hysteresis effect and the dynamics variations that can be compensated-for by using the IIC algorithm. We illustrate the use of the proposed IIC technique (to compensate-for both the hysteresis and dynamics effects) through experiments on a piezotube scanner of an AFM system. The experiment results show that high-speed, large-range precision positioning can be achieved. Moreover, the proposed IIC algorithm is applied to experimentally validate i) the cascade model of the piezo actuator; and ii) the rate-independence of the hysteresis effect. We note that although with the recent efforts [21, 22], the charge-control based approach becomes practically efficient for hysteresis compensation, such an approach may be restricted to piezo actuators only. On the contrary, the proposed IIC technique can also be applied to other smart actuators (with similar hysteresis characteristics as piezo actuators). We also note that the tracking performance of the proposed IIC technique can be further improved, in general, by augmenting with the feedback control [7]. This chapter, however, is focused on the use of the IIC technique for high-speed, large-range precision positioning of piezo actuators.

2.2 Hysteresis & Vibrational Dynamics Compensation: IIC Approach

In this section, we will show that a recently developed inversion-based iterative-control (IIC) technique [1, 2] can be used to compensate for both the nonlinear hysteresis and the linear dynamics effects of piezo actuators. We start with a brief review of the IIC technique.

2.2.1 Inversion-based Iterative Control (IIC) [1, 2]

The IIC control law can be described in frequency domain as follows

$$\begin{aligned} u_0(j\omega) &= 0, \\ u_{k+1}(j\omega) &= u_k(j\omega) + \rho(\omega) G_{a,m}^{-1}(j\omega)[x_d(j\omega) - x_k(j\omega)] \end{aligned} \tag{2.1}$$

where $G_{a,m}(j\omega)$ is the frequency response model of the system, $\rho(\omega) \in \Re$ is the frequency-dependent iterative coefficient, and $u_k(j\omega)$ and $x_k(j\omega)$ are the Fourier transform of the input and the output at the k^{th} iteration, $u_k(t)$ and $x_k(t)$, respectively. The convergence of this IIC algorithm (2.1) is given by the following lemma [1]:

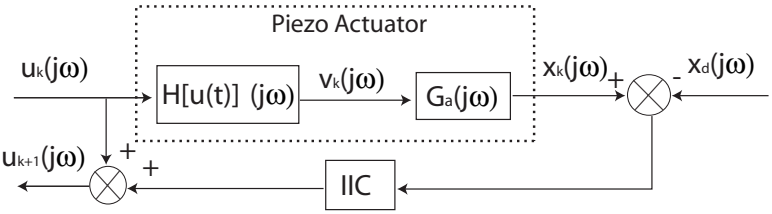

Figure 2.1 The block diagram of the IIC algorithm, where the input-output relation of the piezo actuator is captured by a cascade model [3] (Assumption 1).

Lemma 1 *For any given frequency value ω, let the actual system's vibrational dynamics $G_a(j\omega)$ and its model $G_{a,m}(j\omega)$ be stable and hyperbolic (i.e., have no zeros on the $j\omega$ axis), also let the linear dynamics variation $\Delta G(j\omega)$ be described by*

$$\Delta G(j\omega) \quad = \quad \frac{G_a(j\omega)}{G_{a,m}(j\omega)} = \frac{r_a(\omega)e^{j\theta_a(\omega)}}{r_{a,m}(\omega)e^{j\theta_{a,m}(\omega)}} = \Delta r(\omega)e^{j\Delta\theta(\omega)}. \tag{2.2}$$

Then the iterative law (2.1) will converge at frequency ω, i.e., $\lim_{k\to\infty} x_k(j\omega) = x_d(j\omega)$, if and only if

1. *The magnitude of the phase variation is less than $\pi/2$, i.e., $|\Delta\theta(\omega)| < \pi/2$, and*
2. *The iteration coefficient $\rho(\omega)$ is chosen as $0 < \rho(\omega) < \frac{2cos(\Delta\theta(\omega))}{\Delta r(\omega)}$.*

Lemma 1 implies that the IIC algorithm (2.1) can be implemented to compensate-for the effect of vibrational dynamics in output-tracking, as experimentally demonstrated in [1, 23]. Next, we discuss the use of this IIC technique to compensate-for both the hysteresis and the vibrational dynamics effects of piezo actuators.

2.2.2 Compensation for both the Hysteresis and the Vibrational Dynamics Effects

We begin by assuming that [3]

Assumption 1 *The input-output mapping, $u(t) \to x(t) : \Re \to \Re$, of a piezo actuator can be captured by using a cascade model consisting of the rate-independent, nonlinear hysteresis operator $\mathbf{H}[u(t)]$ at the input followed by the linear vibrational dynamics, $G_a(j\omega)$, such that $x(j\omega) = G_a(j\omega)\mathbf{H}[u(\cdot)](j\omega)$ (see Fig. 2.1).*

Assumption 2 *The hysteresis effect of the system is rate-independent [14, 4].*

Therefore, Assumptions 1, 2 decouple the time-independent (i.e., the hysteresis) effect from the time-dependent(i.e., the vibrational dynamics) effect in the input-output relation of a piezo actuator. In Sec. 2.3.3, we will experimentally validate Assumptions 1, 2 on a piezotube actuator. Next we employ the Preisach model of hysteresis [24] that effectively captures the range (amplitude)-dependent nature of the hysteresis effect [7]. Specifically, we say that the system has the same *initial condition in hysteresis* (ICH) if the system has the same memory curve on the Preisach plane [4] for modeling the hysteresis, i.e., the initial values of the internal states of the Preisach model are the same.

Remark 1 *The same ICH requirement can be satisfied, for example, by using the initialization process as discussed in [4]: Before each iteration, slowly increase the input to its upper bound needed to track the desired output v_d, then slowly decrease the input to the value corresponding to the initial desired output $v_d(t_0)$. In the following, such an initialization process is applied when implementing the IIC algorithm.*

Then we consider that the hysteresis part of the cascade model, $u(t) \to v(t)$ (see Fig. 2.1), satisfies,

Assumption 3 *For the piezo system having the same ICH condition at the initial time instant t_i, the difference in the hysteresis output, $v_2(\cdot) - v_1(\cdot)$, can be bounded by the input difference, $u_2(\cdot) - u_1(\cdot)$, as*

$$\begin{aligned} & \int_{-\infty}^{\infty} |f(t) + (v_1(t) - v_2(t))|^2 \, dt \\ \leq \; & \int_{-\infty}^{\infty} |f(t) + \eta_1(u_1(t) - u_2(t))|^2 \, dt + \int_{-\infty}^{\infty} |f(t) + \eta_2(u_1(t) - u_2(t))|^2 \, dt \end{aligned} \tag{2.3}$$

where $\eta_1, \eta_2 > 0$ are constants, $u_1(\cdot), u_2(\cdot) \in C \cap L^\infty$ are two continuous, bounded inputs applied from time instant t_i, and the function $f(t) \in L^2 \cap L^\infty \cap C$ is also square integrable, and has the same sign as the input difference, $u_1(t) - u_2(t)$, in the integration sense, i.e.,

$$\int_{-\infty}^{\infty} f(t) \, (u_1(t) - u_2(t)) \, dt > 0. \tag{2.4}$$

Remark 2 *For inputs $u_1(\cdot)$ and $u_2(\cdot)$ being both monotonic, the above Assumption 3 can be satisfied if the hysteresis operator is strictly piecewise increasing as assumed in [13] or satisfies a Lipschitz like condition as in [4]. In both cases, the above Assumption 3 is less stringent.*

Remark 3 *For a linear time invariant system (e.g., the vibrational dynamics part of the piezo actuator), the input and output will have the same-sign in the integration sense (i.e., satisfy (2.4)) if the phase change of the dynamics is less than $\frac{\pi}{2}$ [25].*

Lemma 2 *Let Assumptions 1 to 3 be satisfied, and the desired trajectory $x_d(t) \in C$ be continuous and have a compact support $S = [t_i,\ t_f]$. Also, let the following conditions be satisfied,*

1. *There exist a compact set of frequency, Ω, such that for all frequency $\omega \in \Omega$,*

   (a) *both the system's actual linear dynamics $G_a(j\omega)$ and its model $G_{a,m}(j\omega)$ are stable and hyperbolic (i.e., both have no zeros on $j\omega$ axis, and thereby $\Delta r(\omega) > 0$);*

   (b) *the phase variation is bounded as*

   $$|\Delta\theta(\omega)| \leq \theta_1 \triangleq \arccos\left[\sqrt{\frac{\eta_1^2 + \eta_2^2}{(\eta_1 + \eta_2)^2}}\right] \tag{2.5}$$

   (c) *there exists a constant $\epsilon > 0$, such that under the hysteresis effect, $\Delta\mathbf{H}$, and the effect of the system dynamics variations, $\Delta\mathbf{G}_L(j\omega)$ and $\Delta\mathbf{G}_H(j\omega)$,*

   $$\sup_{\omega\in\Omega}(\rho_\ell(\omega)) + \epsilon \quad < \quad \inf_{\omega\in\Omega}(\rho_h(\omega)) \tag{2.6}$$

   with $\rho_\ell(\omega) \triangleq \Delta\mathbf{H} \times |\Delta\mathbf{G}_L(j\omega)|$,
   $\rho_H(\omega) \triangleq \Delta\mathbf{H} \times |\Delta\mathbf{G}_H(j\omega)|$ and

   $$\begin{aligned} \Delta\mathbf{H} &\triangleq \frac{\eta_1 + \eta_2}{\eta_1^2 + \eta_2^2}, \\ \Delta\mathbf{G}_{H,L}(j\omega) &\triangleq \frac{\cos\Delta\theta(\omega) \pm \sqrt{\cos^2\Delta\theta(\omega) - \cos^2\Delta\theta_1}}{\Delta r(\omega)} \end{aligned} \tag{2.7}$$

2. *The iteration coefficient ρ in the iterative control law (2.1) is chosen as $\rho = 0$ for $\omega \notin \Omega$, and a constant for $\omega \in \Omega$ from*

   $$\rho \in \left(\sup_{\omega\in\Omega}(\rho_\ell(\omega)),\quad \inf_{\omega\in\Omega}(\rho_h(\omega))\right). \tag{2.8}$$

Then the iteration law (2.1) will converge in L^2-norm to the desired input $u_d(j\omega) = G_a(j\omega)\mathbf{H}[u_d(\cdot)](j\omega)$ with restrict to the set Ω:

$$\lim_{k\to\infty} \|u_k(\cdot) - \hat{u}_d(\cdot)\|_2 = \lim_{k\to\infty} \left[\int_{-\infty}^{\infty} |u_k(\tau) - \hat{u}_d(\tau)|^2 d\tau\right]^{1/2} = 0, \tag{2.9}$$

where $\hat{u}_d(j\omega) = u_d(j\omega)$ for $\omega \in \Omega$, and $\hat{u}_d(j\omega) = 0$ otherwise.

Proof By Assumption 1, the input-output mapping of a piezo actuator can be modeled by using the cascade model, i.e., $x(j\omega) = G_a(j\omega)\mathbf{H}[u(\cdot)](j\omega)$ (see Fig. 2.1). Thus, the iterative control law (2.1) can be rewritten as

$$\begin{aligned} u_{k+1}(j\omega) &= u_k(j\omega) + \rho \cdot G_{a,m}^{-1}(j\omega)\,[x_d(j\omega) - x_k(j\omega)] \\ &= u_k(j\omega) + \rho \cdot G_{a,m}^{-1}(j\omega) \cdot [G_a(j\omega)v_d(j\omega) - G_a(j\omega)v_k(j\omega)] \\ &= u_k(j\omega) + \rho \cdot \Delta G(j\omega)\,[v_d(j\omega) - v_k(j\omega)] \end{aligned} \tag{2.10}$$

where $v_d(t)$ and $v_k(t)$ are hysteresis outputs for inputs $u_d(t)$ and $u_k(t)$ respectively (see Fig. 2.1). Next, we consider the tracking of the frequency components in set Ω only (given by Eqs. (2.5,2.6)), by choosing $\rho = 0$ for all $\omega \notin \Omega$—$u_k(j\omega) = 0$ for $\forall k$, and $\forall \omega \notin \Omega$. Thus, the above equation is equivalent to

$$u_{k+1}(j\omega) = u_k(j\omega) + \rho \cdot \Delta\hat{G}(j\omega)\,[v_d(j\omega) - v_k(j\omega)]\,, \tag{2.11}$$

with $\Delta\hat{G}(j\omega) = \Delta G(j\omega)$ for $\omega \in \Omega$, and $\Delta\hat{G}(j\omega) = 0$ otherwise. Since both the actual linear dynamics $G_a(j\omega)$ and its model $G_{a,m}(j\omega)$ are hyperbolic, $\Delta\hat{G}(j\omega)$ is invertible for $\omega \in \Omega$, and (2.11) leads to

$$\begin{aligned} &\Delta\hat{G}^{-1}(j\omega)\,[u_{k+1}(j\omega) - u_d(j\omega)] \\ =&\Delta\hat{G}^{-1}(j\omega)\,[u_k(j\omega) - u_d(j\omega)] + \rho \cdot \Delta\hat{G}^{-1}(j\omega)\Delta\hat{G}(j\omega)\,[v_d(j\omega) - v_k(j\omega)] \\ =&\Delta\hat{G}^{-1}(j\omega)\,[u_k(j\omega) - u_d(j\omega)] + \rho \cdot [v_d(j\omega) - v_k(j\omega)] \end{aligned} \tag{2.12}$$

Taking the square of 2-norm in (2.12),

$$\begin{aligned}
& \left\| \Delta \hat{G}^{-1}(j\omega)\,[u_{k+1}(j\omega) \;-\; u_d(j\omega)] \right\|_2^2 \\
= & \int_{-\infty}^{\infty} \left| \Delta\; \hat{G}^{-1}(j\omega)\,[u_{k+1}(j\omega) - u_d(j\omega)] \right|^2 d\omega \\
= & \int_{\omega\in\Omega} |\Delta \hat{G}^{-1}(j\omega)\,[u_k(j\omega) - u_d(j\omega)] + \rho \cdot [v_d(j\omega) - v_k(j\omega)]\,|^2 d\omega \\
= & \int_{-\infty}^{\infty} |\phi(t) \otimes [u_k(t) - u_d(t)] + \rho\,[v_d(t) - v_k(t)]|^2\, dt \\
& \text{(by Parseval's Theorem [26].)}
\end{aligned} \tag{2.13}$$

where $\phi(t)$ denotes the impulse response of $\Delta\hat{G}^{-1}(j\omega)$ and '$\otimes$' denotes the convolution operation. Note in (2.13), the inputs $u_d(\cdot)$ and $u_k(\cdot)$ are continuous and bounded functions (more precisely, we choose the continuous function from the equivalent class [26] of the inverse Fourier transform of $u_d(j\omega)$ and $u_k(j\omega)$, respectively). Therefore, the output of the dynamics variation for the input difference $u_k(t) - u_d(t)$, $g(t) \triangleq \phi(t) \otimes [u_k(t) - u_d(t)]$, belongs to $L^2 \cap L^\infty \cap C$ [27]. Furthermore, Condition 1(b) (Eq. (2.5)) implies that the phase change of the dynamics variation $\Delta\hat{G}^{-1}(j\omega)$, $|\Delta\theta(\omega)|$, is less than $\pi/2$ (i.e., $\theta_1 \leq \arccos[\sqrt{1/2}] < \pi/4$). As a result, the output $g(t)$ of the dynamics variation $\Delta\hat{G}^{-1}(j\omega)$ has the same sign as the input in the integration-sense (see Remark 3), i.e.,

$$\int_{-\infty}^{\infty} g(t)\,(u_k(t) - u_d(t)) = \int_{-\infty}^{\infty} \{\phi(t) \otimes [u_k(t) - u_d(t)]\}\,(u_k(t) - u_d(t)) > 0 \tag{2.14}$$

From the Preisach model of the hysteresis, the continuity and boundness of the inputs, $u_d(\cdot)$ and $u_k(\cdot)$, implies that the hysteresis outputs, $v_d(\cdot)$ and $v_k(\cdot)$, are also bounded and continuous [24]. Thus, all the conditions in Assumption 3 are satisfied, and Assumption 3 implies that for any

given positive constant ρ, (2.13) leads to

$$
\begin{aligned}
&\left\|\Delta\hat{G}^{-1}(j\omega)\left[u_{k+1}(j\omega)-u_d(j\omega)\right]\right\|_2^2\\
=&\int_{-\infty}^{\infty}\left|\phi(t)\otimes\left[u_k(t)-u_d(t)\right]\right|^2dt\\
\leq&\int_{-\infty}^{\infty}\left|\phi(t)\otimes\left[u_k(t)-u_d(t)\right]+\rho\cdot\eta_1\cdot\left[u_d(t)-u_k(t)\right]\right|^2\\
&+\left|\phi(t)\otimes\left[u_k(t)-u_d(t)\right]+\rho\cdot\eta_2\cdot\left[u_d(t)-u_k(t)\right]\right|^2dt\\
=&\int\left|\Delta\hat{G}^{-1}(j\omega)\left[u_k(j\omega)-u_d(j\omega)\right]+\rho\eta_1\left[u_d(j\omega)-u_k(j\omega)\right]\right|^2\\
&+\left|\Delta\hat{G}^{-1}(j\omega)\left[u_k(j\omega)-u_d(j\omega)\right]+\rho\eta_2\left[u_d(j\omega)-u_k(j\omega)\right]\right|^2d\omega\\
=&\int_{\omega\in\Omega}\left|\Delta\hat{G}^{-1}(j\omega)\left[u_k(j\omega)-u_d(j\omega)\right]\right|^2\left[\left|1-\rho\eta_1\Delta\hat{G}(j\omega)\right|^2+\left|1-\rho\eta_2\Delta\hat{G}(j\omega)\right|^2\right]d\omega\\
\leq&\sup_{\omega\in\Omega}\left[\left|1-\rho\eta_1\Delta\hat{G}(j\omega)\right|^2+\left|1-\rho\eta_2\Delta\hat{G}(j\omega)\right|^2\right]\int_{\omega\in\Omega}\left|\Delta\hat{G}^{-1}(j\omega)\left[u_k(j\omega)-u_d(j\omega)\right]\right|^2d\omega\\
&\cdots\\
\leq&\left\{\sup_{\omega\in\Omega}\left[\left|1-\rho\eta_1\Delta\hat{G}(j\omega)\right|^2+\left|1-\rho\eta_2\Delta\hat{G}(j\omega)\right|^2\right]\right\}^{k+1}\int_{\omega\in\Omega}\left|\Delta\hat{G}^{-1}(j\omega)\left[u_0(j\omega)-u_d(j\omega)\right]\right|^2d\omega\\
=&\left\{\sup_{\omega\in\Omega}\left[\left|1-\rho\eta_1\Delta\hat{G}(j\omega)\right|^2+\left|1-\rho\eta_2\Delta\hat{G}(j\omega)\right|^2\right]\right\}^{k+1}\left\|\Delta\hat{G}^{-1}(j\omega)\left[u_0(j\omega)-u_d(j\omega)\right]\right\|_2^2 \quad (2.15)
\end{aligned}
$$

Note that $\left|\Delta\hat{G}^{-1}(j\omega)\right|>0$ for any $\omega\in\Omega$, thus the above (2.15) shows that the input law $u_k(\cdot)$ will converge to the desired input $u_d(\cdot)$ with restrict to the set Ω (see (2.9)) if there exists a constant ρ, such that

$$\sup_{\omega\in\Omega}\left[\left|1-\rho\eta_1\Delta\hat{G}(j\omega)\right|^2+\left|1-\rho\eta_2\Delta\hat{G}(j\omega)\right|^2\right]<1 \quad (2.16)$$

Next we show that such a constant $\rho>0$ exists if Conditions 1-2 are satisfied. Equation (2.16) can be rewritten as

$$\left[\Delta r(\omega)^2(\eta_1^2+\eta_2^2)\right]\rho^2-\left[2\cos\left(\Delta\theta(\omega)\right)\Delta r(\omega)\ (\eta_1+\eta_2)\ \right]\rho+1<0,\quad \text{for } \forall\omega\in\Omega. \quad (2.17)$$

A positive ρ satisfying the above (2.17) exists provide that the coefficients of the quadratic polynomial of ρ on the left side of (2.17) satisfying

$$4\cos^2\Delta\theta(\omega)\Delta r(\omega)^2(\eta_1+\eta_2)^2-4\Delta r^2(\omega)(\eta_1^2+\eta_2^2)>0 \quad (2.18)$$

Simplifying (2.18) leads to Condition 1. b) (2.5). Under Condition 1. b), the range of the iteration coefficient ρ to guarantee the convergence can be obtained by finding the roots of

the polynomial of ρ in (2.17) as $\rho_{H,\ell} = \Delta\mathbf{H} \times |\Delta\mathbf{G}_{H,\ell}(j\omega)|$ with $\Delta\mathbf{H}, \Delta\mathbf{G}_{H,L}$ given by (2.7). Therefore, a desired positive constant ρ can be found (given by (2.8), Condition 2) provided Condition 1 (i.e., (2.6)) is satisfied, This completes the proof. ■

Remark 4 *The bound of the iteration coefficient ρ, as given by (2.7, 2.8), reflects the cascade model of the piezo actuator: it is a multiplication of one term reflecting the hysteresis effect, $\Delta\mathbf{H}$, with the other term reflecting the dynamics effect, $\Delta\mathbf{G}_{L,H}(j\omega)$.*

Remark 5 *Compared with the use of the IIC algorithm to compensate for the dynamics effects only, the converged frequency range, as well as the bound of the iterative coefficient ρ, becomes smaller, due to the effort to also combat the hysteresis effect: As shown in (2.5), the allowed phase variation of the converged frequency range Ω is reduced from $\pi/2$ (when only compensating for the dynamics, see Lemma 1) to $\pi/4$. Moreover, the bound of the iterative coefficient ρ is also smaller than that for dynamics compensation only. As shown in (2.6–2.8), the range of ρ approaches to that for dynamics compensation only (see Lemma 1) when the converged frequency range $\Delta\theta_1$ approaches to $\pi/2$—only possible when there is no hysteresis effect.*

Remark 6 *The use of the dynamics model $G(j\omega)$ in the proposed IIC algorithm is essential for compensating for both the hysteresis and the vibrational dynamics effects. On the contrary, a constant iteration coefficient (i.e., remove $G^{-1}(j\omega)$ in (1)) is used in the IIC algorithm proposed in [13, 4] for hysteresis compensation. Note in the low frequency, $G(j\omega)$ approaches to the DC-Gain of the system, therefore, the IIC algorithm in [13, 4] can be regarded as a special case of the proposed IIC algorithm in the low-frequency range.*

Remark 7 *It can be shown that under the effect of system noise (e.g., measurement noise), the error between the converged iterative control input and the desired input (in 2-norm) is bounded above by a constant that is proportional to the square-root of i) the system noise level, ii) the iterative coefficient ρ, and iii) the size of the system dynamics variation.*

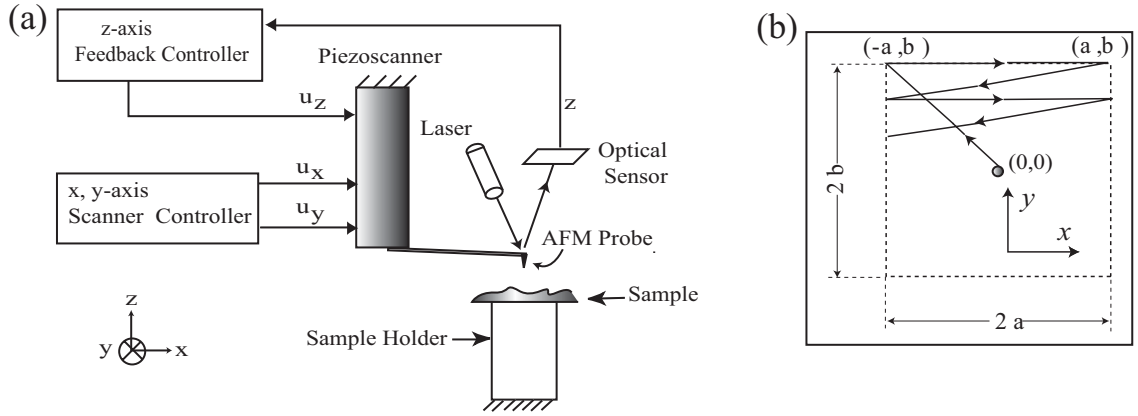

Figure 2.2 a) the schematic diagram of AFM operation, and b) the top view of the typical scanning trajectories for AFM imaging[1, 4].

2.3 Example: High-speed Large-Range Scanning for AFM Imaging

The IIC approach is applied to control the piezotube actuator on an AFM system. The goal is to experimentally demonstrate that high-speed, large-range precision positioning can be obtained by using the proposed IIC algorithm. We begin by describing the use of the piezotube actuator in the AFM operation.

2.3.1 The experimental AFM system

The AFM system ($Dimension^{TM}$ 3100, Veeco Inc) studied in this chapter utilizes piezotube actuators to position the AFM probe with respect to the sample during the imaging (see Fig. 2.2 (a)), in both parallel (along the x-y axes) and perpendicular (along the z-axis) directions. Positioning errors of the probe relative to the sample will generate large image distortions [3, 20], and further damage the probe [28], the sample [29], or both. Such large positioning errors can be generated in both lateral scanning x-axis and vertical z-axis direction when imaging relatively-large samples at high-speed. In this experiment, we will use the IIC algorithm to the output tracking of the *periodic* scanning along the x-axis direction (see Fig. 2.2 (b)).

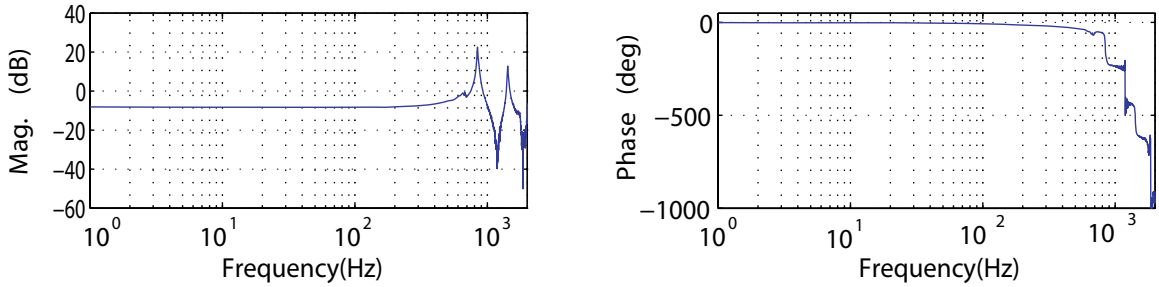

Figure 2.3 The experimentally measured frequency response of the piezo actuator in the x-axis direction (up to the frequency of 2kHz).

2.3.2 Experimental Implementation of the IIC Algorithm

Model the Linear, Vibrational Dynamics of the Piezotube Actuator We first experimentally measured the frequency response of the piezotube actuator in the lateral scanning (x-axis) direction, $G_{a,m}(j\omega)$, by using a dynamic signal analyzer (DSA, HP35665A). To measure the frequency response $G_a(j\omega)$, a sinusoidal input voltage u(t) generated by the DSA is applied to the piezo actuator through a power amplifier and the x-axis sensor output voltage of the actuator x(t) is measured (using an inductive sensor) and fed back to the DSA. Measurements with several different input amplitudes (all were kept small to avoid the hysteresis effect) were obtained and averaged to obtain the nominal frequency response up to 2 KHz (see Fig. 2.3). The bode plot presents a sharp resonant peak at 840.2 Hz—a dramatic increase in magnitude accompanied by a rapid drop in phase. As a result, the piezotube actuator has a very low gain margin at only -20.4 dB, which, in turn, limits the performance of PID control. Also note that the frequency response data can be used directly in the computation of the proposed IIC algorithm in frequency-domain, thereby avoiding possible modeling errors from the curve-fitting process to obtain a low-order transfer function model.

Quantify the linear vibrational dynamics variation $\Delta r(j\omega)$, $\Delta\theta(j\omega)$ (see (2.2)) Next we will quantify the iterative coefficient ρ used in the proposed IIC algorithm. We start with quantifying the linear dynamics variation experimentally, by measuring the frequency

responses of the piezo actuator with different input amplitudes (0.1, 0.125, 0.15V) with a DSA as described in Section 2.3.2. Then the magnitude variation and the phase variation at each measured frequency, $\Delta r(\omega)$ and $\Delta\theta(\omega)$, were computed from the three obtained frequency responses, as shown in Fig. 2.4 (a), (b).

Quantify the hysteresis effect constants η_1, η_2 (see (2.3)) Next, we quantify the hysteresis effect constants η_1, η_2 needed to determine the iterative coefficient ρ (see (2.5–2.8)). We modeled the nonlinear hysteresis behavior by using the Preisach approach as in [4, 30], and estimated the constants η_1 and η_2 in Assumption 3 by using the monotonic increasing portion of the hysteresis output (see Remark 2). The procedure detailed in [4, 30] was followed. First, the Preisach plane was obtained experimentally and partitioned in Q sub-regions. Then, the weighting function $\mu(\alpha, \beta)$ used in the Preisach model (e.g., [4]) was estimated by using a least-square approach [4, 30]. The obtained weighting function $\mu(\alpha, \beta)$ was then used to estimate the constants η_1 and η_2 (see [4, 30] for the details). For the piezotube actuator used in our AFM system, $\eta_1 = 0.334$ and $\eta_2 = 2.329$ were obtained experimentally.

Choose the iteration coefficient ρ (Eq. (2.7)) The estimated phase and magnitude variations, $|\Delta\theta(\omega)|$ and $|\Delta r(\omega)|$, and the estimated hysteresis constants, η_1 and η_2,, were used to determine the trackable frequency range Ω (see Lemma 2, Eq. (2.5)), and correspondingly, the upper and lower bounds of the iterative coefficient, $\rho_\ell(\omega)$ and $\rho_h(\omega)$ (see (2.7)), as shown in Fig. 2.4 (b). It can be seen from Fig. 2.4 (c) that a constant iterative coefficient $\rho = 0.5$ can be found in the frequency range [0, 1.8] kHz—Conditions 1, 2 are satisfied, and the frequency components in this frequency range are trackable by using the IIC algorithm.

Experimental Implementation of the IIC Algorithm (2.1) The quantified iterative coefficient ρ and the measured nominal frequency response $G(j\omega)$ (Fig. 2.7) was used to find the iterative control input for tracking a triangle trajectory at four different scan rates, 10 Hz, 50 Hz, 150 Hz, and 300 Hz. The amplitude of the trajectory at 80 μm was chosen below

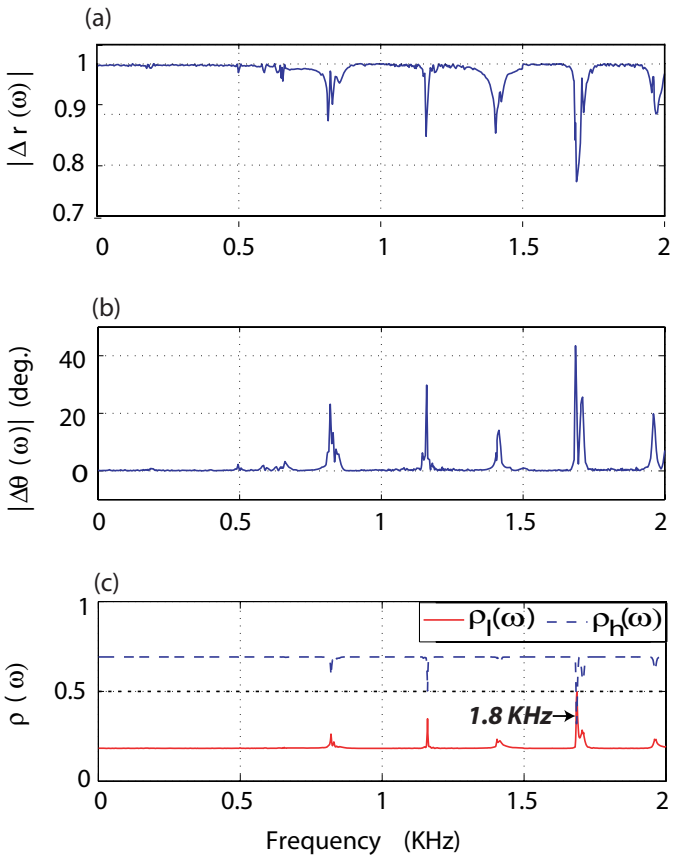

Figure 2.4 The experimentally measured magnitude variation (a), phase variation $\Delta\theta(\omega)$ (b), and the estimated upper bound, lower bound, and the chosen constant of the iterative coefficient, $\rho_h(\omega)$, $\rho_l(\omega)$ and ρ (dotted line), respectively (c),

the full displacement range of the piezotube at 90 μm, because the needed input amplitude for tracking outputs of larger amplitude at high scan rate of 300 Hz exceeds the voltage limit of the data acquisition system used in the experiments. The iterative control law was numerically computed using MATLAB (using commands "`fft`" and "`ifft`"), and applied by using MATLAB xPC-target package. After each iteration, the maximum error E_M (along with the relative maximum error $\widehat{E}_M$), given by

$$\begin{aligned} E_M(\mu m) &= max_{t\in[0,T]}|x_d(t) - x(t)|, \\ \widehat{E}_M(\%) &= \frac{E_M}{max_{t\in[0,T]}|x_d|} \times 100\%, \end{aligned} \tag{2.19}$$

was measured and used to terminate the iteration—when the maximum error did not decrease further. In (2.19), T is the period of the triangle trajectory.

2.3.3 Tracking results and Discussion

Experimental tracking results The tracking results for scan rates of 10 Hz and 300 Hz are compared in Fig. 2.5 with the tracking results obtained by using the *DC-Gain* method, where the input was obtained by scaling the desired output with the DC-Gain K_{dc} of the system (adjusted with the output amplitude). Hence, the DC-Gain method does not address either the hysteresis or the vibrational dynamics effect, and the comparison with the tracking of the DC-Gain method demonstrates the amount of the tracking error caused by the hysteresis and vibration dynamics effects. The tracking errors (E_M and $\widehat{E}_M$) for the four chosen scan rates are also compared in Table 2.1, where the iteration numbers used in the IIC algorithm are listed.

Hysteresis and vibrational dynamics effects lead to the loss of precision in positioning The experimental results show that the effect of the piezotube actuator′s vibrational dynamics on the output tracking is small when the scan rate is low. Fig. 2.5 (a1) and (a2) showed that at scan rate of 10 Hz, no obvious oscillations were observed, instead, the hysteresis-effect-caused positioning error is pronounced, expressed as the parabolic-shape bowing curve in the output. Such hysteresis-caused positioning errors were augmented to the dynamics-induced

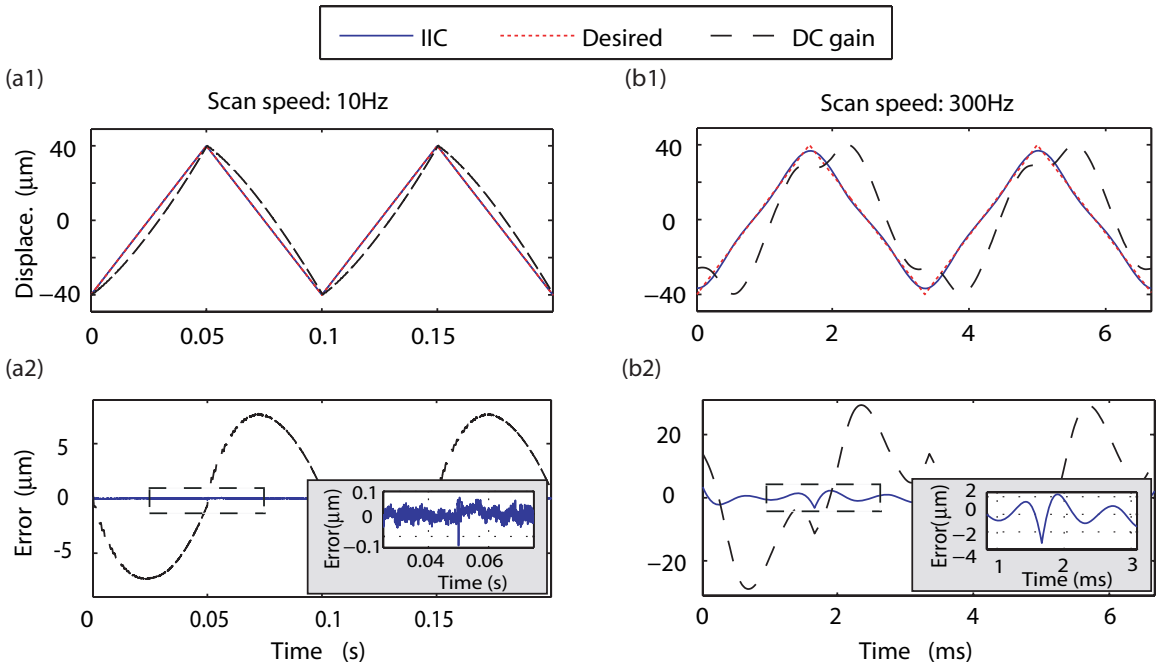

Figure 2.5 The experimental tracking results (a1, b1) and tracking errors (a2, b2) obtained by using the IIC technique and DC-gain method for scan rates of 10Hz, and 300Hz, the insets in (a2, b2) are the zoomed-in view of the positioning errors from the IIC technique within the dashed window.

vibrations as the scan rate was increased. When the scan rate was increased to 300 Hz, the output obtained by using the DC-Gain method has large high-frequency oscillations, resulting in a large relative tracking error at $\hat{E}_M(\%) = 36.5\%$ (see Fig. 2.5 (d1) and (d2)). Therefore, hysteresis and vibrational dynamics must be compensated-for to achieve high-speed and large-range tracking in AFM operation.

IIC approach can compensates for the hysteresis effect The experimental results showed that the hysteresis effect can be effectively compensated for by using the IIC algorithm. At large-range (80 μm), slow-speed (scan rate of 10 Hz) tracking, the pronounced hysteresis-caused positioning errors were significantly reduced by using the IIC algorithm after 6 times iteration (see Fig. 2.5 (a1, a2) and Table. 2.1). The equivalent voltage of the maximum error $\widehat{E}_M$ is only about 25.5 mV, which is close to the noise level of the experimental system at 20.1 mV (measured as peak-to-peak value). Therefore, the experimental results demonstrate that the proposed IIC approach can effectively compensate for the hysteresis effect.

We note that the noise of the experimental system is mainly generated by the BNC cable connecting the data acquisition card to the AFM controller (The noise-level within the AFM controller is over 1 order smaller). The noise effect on the control precision, however, can be reduced with the use of the IIC algorithm: multiple periods of the tracking results obtained at each k^{th} iteration can be averaged to represent the tracking of the k^{th} iteration in the IIC algorithm, thereby various averaging techniques for noise reduction can be utilized—Note that when the converged iterative feedforward control input is applied, sensor signal is not required. Such average-based noise reduction method, however, is not possible in feedback-based control approaches.

IIC approach can compensate for both the hysteresis and the vibrational dynamics effects Our experimental results also demonstrate that the proposed IIC algorithm can significantly reduce large tracking errors caused by the hysteresis and the vibrational dynamics effects during high-speed, large-range positioning, as shown in Fig. 2.5 (b1) and (b2) and Table

2.1. At the scan rate of 50 Hz, the tracking error is reduced by over 1.24 times (compared with the DC-Gain method), and was small by using the IIC approach as the scan rate further increased. For example, at the scan rate of 300 Hz, the tracking error with the IIC approach is still less than 5% of the scan range. Such tracking results compare well with the previous results using the inversion-based feedforward-feedback control (with a high-gain PID control enabled by a notch filter as the feedback controller) in [7], and the results from robust feedback control in [31]. For example, at the scan rate of 50 Hz, the proposed IIC algorithm reduced the maximum tracking error to 0.89% of the scan size at 80 μm, compared to the tracking error of 1.46% of the scan size at 32 μm in [7], and 1.6% of the scan size at 19 μm. Furthermore, note that in [7], the tracking error was measured against an optimal triangle trajectory obtained by using the optimal inversion technique [20] that smoothes out the turn-around corner—where exactly the maximum tracking error occurs (see Fig. 2.5 (b1, b2)), and a sinusoidal trajectory was used in [31]. Whereas the triangle trajectory *without any modification* was used in this experiment. Therefore, the experimental results show that the IIC approach effectively compensate-for both the hysteresis and the vibrational dynamics effects.

We further verified that the residual tracking errors obtained by using the IIC algorithm at

Table 2.1 Comparison of the tracking errors obtained by using the IIC technique and the DC-Gain method at different scan rates, where the Iteration numbers used in the IIC technique are also listed.

Scan Rate	$E_M(\mu m)$		$\hat{E}_M(\%)$		**Iter.**
(Hz)	**DC-gain**	**IIC**	**DC-gain**	**IIC**	**NO.**
10	7.73	0.15	9.64	0.19	6
50	9.82	0.72	12.25	0.89	6
150	15.65	1.94	19.53	2.43	4
300	29.34	3.38	36.5	4.21	4

high-speed (300 Hz) mainly consist of high frequency components outside the trackable frequency range [0, 1.8] kHz of the IIC algorithm. We estimated, by using MATLAB, the power spectrum $P_e(j\omega)$ of the tracking error obtained with the IIC algorithm when tracking the 300

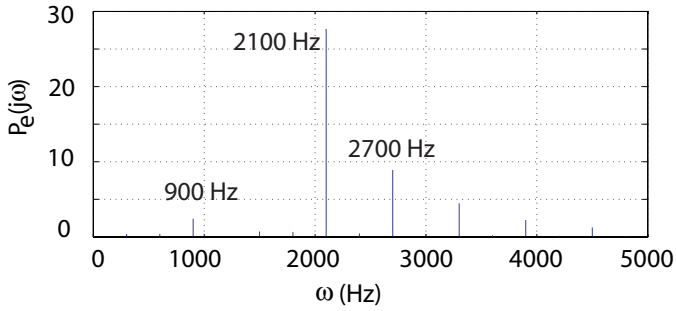

Figure 2.6 The estimated power spectrum of the tracking error $e_y(t)$ obtained by using the inversion-based iterative control for scan rate of 300 Hz. The frequency values where the first three large peaks of the power spectrum appears are indicated.

Hz triangle signal (see $e_x(t)$ shown in Fig. 2.5 (b2)),

$$P_e(j\omega) = \lim_{T\to\infty} \frac{1}{T} e_y^*(j\omega) \times e_y(j\omega) \tag{2.20}$$

where $e_y(j\omega)$ is the fourier transform of the tracking error signal in period T. As shown in Fig. 2.6, the energy (i.e., the power spectrum) of the tracking error is mainly concentrated in the high frequencies outside the trackable frequency range: the power spectrum value at frequency 2.1 kHz (outside [0, 1.8] KHz interval) is 11.44 times larger than the value at 900 Hz. Furthermore, by expanding the Fourier series of the input update term (since the signal is periodic), $\rho G^{-1}(j\omega)(x_d(j\omega) - x_k(j\omega))$, we find that after four iterations, the amplitude of the frequency component of the input updating at 900 Hz is only 20 mV, which is close to the peak-to-peak noise-size of the system at ∼20.1 mV. This implies that further updating of the iterative control input will be "swallowed" by the noise of the signal. Therefore, the experimental results illustrate that the IIC technique can achieve precision positioning of piezo actuators during high-speed, large-range positioning.

Experimental Investigation of Assumptions 1, 2 To experimentally verify that the input-output relation of the piezo actuator can be captured by a cascade model (Assumption 1), we used the IIC algorithm to obtain the control input to compensate-for ("cancel") the hysteresis effect only when tracking a large-range (50 μm), triangle trajectory at high scan

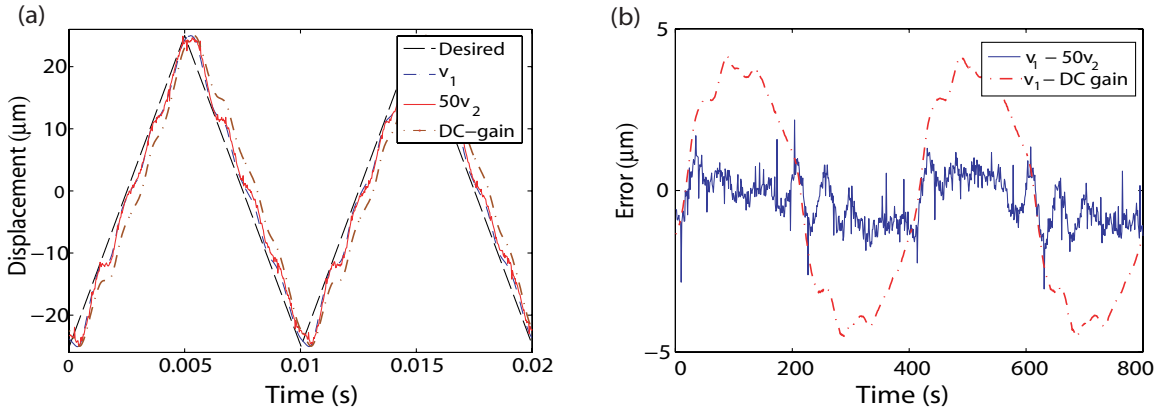

Figure 2.7 (a) compares the experimental tracking obtained by compensating for the hysteresis effect only during the large-range, high--speed (100 Hz) tracking ($v_1(t)$) with the tracking obtained by scaling-up the output obtained at high-speed (100 Hz), small--range (1 μm) tracking ($50v_2$), and the tracking using DC-Gain method; (b) shows the difference of the hysteresis-compensated output $v_1(t)$ with respect to the scale-up output $50v_2(t)$, and the DC-Gain output.

rate of 100 Hz (The readers are referred to [32] for details of the experimental procedure). The obtained tracking results are compared with the scaled-up output tracking obtained at small-range (1 μm) and at the same scan rate (100 Hz) in Fig. 2.7 (a). Since the hysteresis effect is negligible at small range (i.e., hysteresis effect is range dependent [7]), if Assumption 1 holds, these two outputs should resemble each other, as can be seen from Fig. 2.7 (a), where the tracking obtained by using the *DC-Gain* method is also compared. Fig. 2.7 (b) shows that the difference between the hysteresis-compensated output $v_1(t)$ and the DC-Gain output (dashed-line) is much larger than the difference between the output $v_1(t)$ and the scaled-up output 50 $v_2(t)$ (solid line), even though the scaled-up output tracking 50 $v_2(t)$ was effected by relatively-large noises (due to the drop of signal to noise ratio (S/N) in small-range measurement). Therefore, our experimental results show that the piezotube actuator can be modeled by using the cascade approach.

Similarly, to show the rate-independence of the hysteresis effect, the IIC algorithm was also used to, from the output, remove the dynamics effect only when tracking a large-range

(50μm) sinusoidal signal at different scan rates, $x_d(t) = A\sin(2\pi ft)$ with $A = 50\mu m$ and $f = 10, 50, 100, 150$ Hz (The readers are referred to [32] for the details of the experimental procedure). The obtained tracking results are compared in Fig. 2.8 (a), and the difference between the outputs (at different scan rates) and the desired path $y_d(t)$ are compared in Fig. 2.8 (b). Figure 2.8 shows that the maximum difference between the tracking at different scan rates (occurring between the scan rate of $f = 10$ Hz and $f = 100$ Hz) is small—only 7.9% of the maximum tracking error caused by the hysteresis. Furthermore, to maximize the removal of the vibrational dynamics effect by using the IIC algorithm, sinusoidal signals were used in this experiment, because other types of signals such as the triangle signals have higher frequency components (other than the fundamental frequency) of which some are outside the trackable frequency range of the IIC algorithm. Therefore, our experimental results demonstrated that the hysteresis effect is rate-independent.

2.4 Conclusion

This chapter demonstrated the use of iterative leaning control and inversion-based control to achieve high speed AFM imaging. In particular, inversion-based iterative control (IIC) is utilized to compensate for both the nonlinear hysteresis and the linear vibrational dynamics of piezotube actuators. The convergence of the iterative approach was investigated by capturing the hysteresis and the vibrational dynamics effects with a casecade model consisting of the rate-independent hysteresis at the input followed by the linear dynamics of the piezo actuator. The size of the hysteresis effect and the vibration dynamics variation that can be compensated for by using the IIC method is quantified. The implementation of the IIC algorithm on a piezotube actuator of an AFM system were presented to 1) show that high-speed, large-range precision positioning can be achieved; and 2) validate the cascade model of the piezo actuator, and the rate-independence of the hysteresis effect of the piezo actuator.

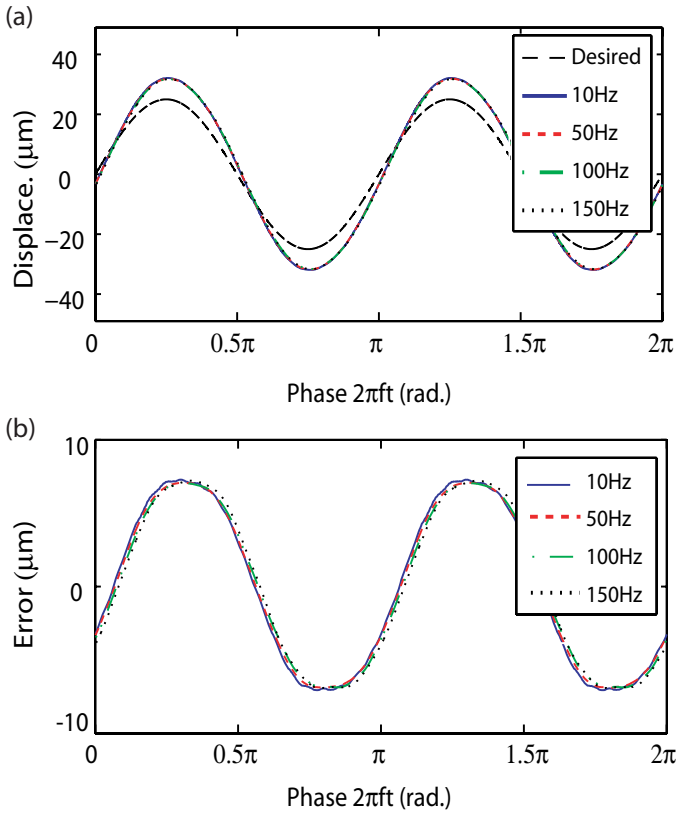

Figure 2.8 Comparison of the outputs effected by hysteresis only (a) and the corresponding tracking errors (b) at different sinusoidal frequencies, after removing the dynamics effect only from the outputs. The x-axis is the phase of the signal $A\sin(f2\pi t)$ with f the frequency of the signal.

CHAPTER 3. Robust-inversion-based 2DOF-control design for output tracking: piezoelectric actuator example

A paper published in IEEE Transactions on Control Systems Technology

Ying Wu [1] and Qingze Zou [2]

Abstract

In this chapter, a novel robust-inversion-based two-degree-of-freedom (2DOF)-control approach for output tracking is proposed. Inversion-based feedforward control techniques have been successfully implemented in various applications. Usually to account for adverse effects such as dynamics variations and disturbances, the inverse feedforward control is applied by augmenting it with a feedback control. However, such effects has not been directly addressed in existing system inversion methods, and the integration of the feedback control with the inversion-based feedforward control is performed in an *ad-hoc* manner, which may not lead to an optimal complement of the inversion-based feedforward control with the feedback control (for example, optimal closed-loop bandwidth). The contribution of this chapter is the development of (1) a novel robust-system-inversion approach to directly account for and then minimize the dynamics uncertainty effect when finding the inversion-based feedforward controller, and (2) a systematic integration (of such a feedforward controller) with a robust feedback controller. The proposed robust-inversion method achieves a guaranteed tracking performance of the feedforward control for bounded dynamics uncertainties. Then the quantified bound of the tracking error of the feedforward control is utilized in designing a H_∞ robust feedback

[1] Primary researcher and author
[2] Corresponding author

controller to complement the feedforward control. Based on the concept of Bode's integral, it is shown that the feedback bandwidth can be improved from that obtained by using feedback alone. We illustrate the proposed approach by implementing it in experiments on a piezotube actuator of an atomic force microscope for precision positioning.

3.1 Introduction

this chapter, we propose a novel robust-inversion feedforward-feedback two-degree-of-freedom (2DOF) controller design. It is noted that the development of the stable inversion methodology [5, 6] has demonstrated the efficacy of the inversion-based feedforward control in output tracking (e.g., [33, 20, 7]). The performance of the inverse feedforward control, however, can be limited by system dynamics uncertainties and disturbances [8], and the dynamics uncertainty effect has not been explicitly addressed in existing system inversion methods [5, 9, 20]. Moreover, to combat these adverse effects, usually the inverse feedforward input is augmented with a feedback controller [20, 7]. However, the integration of the inversion-based feedforward control with the feedback control is performed in an *ad-hoc* manner. Challenges arise when a systematic approach is sought to design the feedback control to complement the inversion-based feedforward control for output tracking. Thus, the contribution of this chapter is the development of (1) a novel robust-system-inversion approach to directly account for and then minimize the dynamics uncertainty effect when finding the inversion-based feedforward controller, and (2) a systematic integration (of such a feedforward controller) with a robust feedback controller. The proposed control design approach is illustrated through the experimental implementation on a piezoelectric actuator for high-speed precision positioning of an atomic force microscope (AFM).

In the proposed robust-system-inversion based 2DOF control approach, issues unaddressed in the system-inversion theory are considered. The development of the stable-inversion technique [5, 6] has solved the challenging problem of achieving exact output-tracking for nonminimum-phase systems, and the preview-based approach [20, 34] further extends such a stable-inversion

methodology for online implementations. The efficacy of the stable-inversion technique has also been successfully demonstrated in various applications, including aircraft guidance [35], flexible structure tracking [36], and nanopositioning of piezo actuators for scanning probe microscope [20, 7]. In practical applications, however, adverse effects such as dynamics uncertainties and input saturation must be accounted when finding the inverse input. Although these effects are considered in the optimal inversion technique [20, 9], the dynamics uncertainty was not directly accounted for in the optimal inversion process, and its effect on the tracking performance of the inversion-based feedforward control, therefore, was not quantified. Moreover, the presence of the feedback control as well as the interaction between the inverse feedforward control and the feedback control were also neglected. Such feedforward-feedback interaction is studied in [8], and the size of allowable dynamics variations in the system inversion—for the inverse feedforward control to improve the tracking performance—is quantified. The focus of the study in [8], however, is not to quantify the tracking performance of the inversion-based feedforward controller in the presence of dynamics, nor to optimize the interaction between the inverse feedforward control with the feedback control. Therefore, there is a need to improve the inversion-based feedforward controller in the presence of dynamics uncertainties, and to further develop an integrated design approach to the inversion-based feedforward-feedback 2DOF control system.

Such an integrated design method—of the inversion-based feedforward-feedback control system—is fundamentally different from the existing two-degree-of-freedom (2DOF) design approaches (e.g., [37]-[42]). We note that the advantages of the 2DOF control over the feedback (or feedforward) control alone has long been recognized [37, 42, 43]. The philosophy of existing 2DOF approaches is to first, design a feedback controller to satisfy the regulation requirements (e.g., internal stability, attenuation of disturbances/noise effects) then secondly, design a *causal*, stable feedforward controller to improve the tracking performance [38, 42] by using, for example, optimal control techniques [38, 43]. On the contrary, the proposed design method starts with designing a robust-*inversion-based* feedforward controller—thereby the structure of the

feedforward controller is chosen—to fully exploit the knowledge of the system dynamics. In a second stage, a feedback controller is designed to complement the feedforward controller. Therefore, the feedback controller is designed for improving tracking as well as the closed-loop regulation properties. Moreover, rather than limiting the choice of the feedforward controller to be causal, the proposed 2DOF design method will allow the inversion-based feedforward controller to be *non-causal*. We note that the stable-inversion theory [5] has shown that for nonminimum-phase systems, the *non-causal* feedforward controller is necessary, in general, for achieving exact-output tracking. Whereas tracking performance limits exist when using feedback control alone [44]. The proposed design method will utilize the recently-developed preview-based stable-inversion technique [34] to enable the online implementation of the non-causal feedforward controller. Therefore, the proposed 2DOF design technique broadens the existing 2DOF design tools by introducing the stable-inversion into the 2DOF controller design.

The contribution of this chapter is the development of a novel robust system-inversion technique for single-input-single-output (SISO) linear time invariant system, along with a systematic approach to integrate the inversion-based feedforward control with the feedback control. A frequency-dependent gain-modulation to the system inverse is introduced, and the robust system-inverse is obtained by solving a minimax optimization problem to seek the optimal modulation gain in the presence of dynamics uncertainties of known bound. Then to complement the inversion-based feedforward control with the feedback control, the guaranteed feedforward tracking-error is utilized to shape the desired feedback sensitivity, which is further realized using H_∞ robust feedback control framework [45] to design the feedback controller. We note that although the integration of these two control approaches (the stable-inversion-based feedforward control and the H_∞ robust feedback control), can be proceeded through a careful tuning, the tuning process tends to be *ad hoc*. On the contrary, the proposed control design method represents one of the first attempts to systematically merge these two control approaches together. We illustrate the proposed control technique by implementing it to control a piezoelectric actuator for AFM imaging applications. The experimental results show that

compared with the feedback controller designed without considering the feedforward controller, the feedback-bandwidth is increased by over 28% by using the proposed control method. As a result, high-speed precision-output tracking can be achieved.

The rest of the chapter is organized as follows. The design of a robust-inversion-based 2DOF control system is formulated and solved in Section 3.2, where the robust-system-inversion is proposed and developed, followed by the design of the complementary feedback controller. In Section 3.3, the implementation of the proposed approach to the output tracking of the piezoelectric actuator is described, where the experimental results are presented and discussed. Our conclusions are given in Section 3.4.

3.2 Robust-Inversion-Based 2DOF Control System Design

3.2.1 Problem Formulation

We consider the inversion-based 2DOF control system depicted in Fig. 3.1, where $G_o(j\omega) : \Re \to \Re$ is the transfer function of a single-input-single-output (SISO) plant, $G_{FF}(j\omega)$ and $G_{FB}(j\omega)$ are the feedforward and the feedback controllers, respectively, $r(j\omega)$ is the input to the entire 2DOF system, $v(j\omega)$ is the system output, and $u_{FF}(j\omega)$ and $u_{FB}(j\omega)$ are the feedforward and the feedback inputs to the plant, respectively. Then the transfer function of the entire system, from the input $r(j\omega)$ to the output $v(j\omega)$, can be represented as

$$G_{total}(j\omega) = \left[G_{FF}(j\omega) + G_{FB}(j\omega)\right] G_o(j\omega)S(j\omega), \tag{3.1}$$

where $S(j\omega)$ and $T(j\omega)$ are the closed-loop sensitivity and the closed-loop complementary sensitivity, respectively, i.e.,

$$S(j\omega) = \frac{1}{1 + G_{FB}(j\omega) \cdot G_o(j\omega)}, \quad T(j\omega) = \frac{G_{FB}(j\omega) \cdot G_o(j\omega)}{1 + G_{FB}(j\omega) \cdot G_o(j\omega)}. \tag{3.2}$$

In the following, we design the feedforward controller based on the inverse of the system dynamics,

$$G_{FF}(j\omega) = \hat{G}_o^{\,-1}(j\omega), \tag{3.3}$$

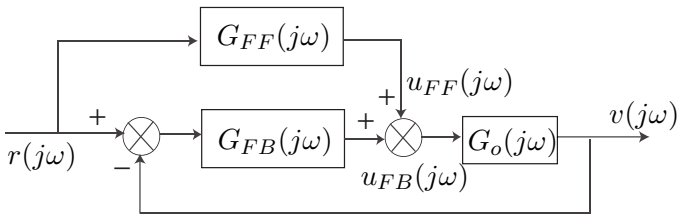

Figure 3.1 The block diagram of the 2DOF control system.

where $\hat{G_o}^{-1}(j\omega)$ denotes the modified inverse of the plant $G_o(j\omega)$. Such a choice of feedforward controller is motivated by the successful implementations of the inversion-based control in various applications [5, 6, 46].

To clarify the design problem of the robust-inversion-based 2DOF controller, we start with decoupling the gain-error of the entire 2DOF system (3.1) with respect to the unit gain as follows,

Lemma 3 *[8] The gain-error of the entire 2DOF system $\epsilon(\omega)$ can be decoupled as the gain-error of the feedforward path, $\left|1 - \hat{G_o}^{-1}(j\omega)G_o(j\omega)\right|$, multiplied with the feedback sensitivity gain, $|S(j\omega)|$,*

$$\epsilon(\omega) \triangleq |1 - G_{total}(j\omega)| = \left|1 - \hat{G_o}^{-1}(j\omega)G_o(j\omega)\right| \cdot |S(j\omega)| \tag{3.4}$$

In the following, we call $\epsilon(\omega)$ the *total gain-error*, and $\left|1 - \hat{G_o}^{-1}(j\omega)G_o(j\omega)\right|$ the *feedforward gain-error.*

Remark 8 *[8] Note that the feedback sensitivity $S(j\omega)$ also represents the feedback gain-error with absence of feedforward control. Therefore, Lemma 3 implies that the feedforward controller will enhance the tracking of the entire 2DOF system,* if and only if *the feedforward gain-error is less than 1, i.e.,*

$$\left|1 - \hat{G}_o^{-1}(j\omega)G_o(j\omega)\right| < 1. \tag{3.5}$$

The above sufficient and necessary Condition (3.5) holds regardless the type of the feedback controller (provided that the feedback-loop is stable).

Note that practical constraints exist in both feedforward and feedback designs: the feedforward control is limited by modeling error and dynamics uncertainty [8], while the feedback control must possess certain stability robustness properties [45]. Thus, we formulate the robust-inversion-based 2DOF controller design problem as below.

The Robust-Inversion-based 2DOF Controller Design Design the inversion-based 2DOF control system such that at the frequency ω where the overall tracking performance can be improved by using the feedforward control (such a frequency will be specified later through the development), the following two objectives are satisfied:

1. The tracking-error of the feedforward control at the frequency ω, measured by the feedforward gain-error $\epsilon_{ff}(\omega)$, is minimized in the presence of the worst dynamics uncertainties of given bound, i.e.,

$$\min \sup_{\Delta G(j\omega)} \epsilon_{ff}(\omega) \triangleq \min \sup_{\Delta G(j\omega)} \left| 1 - \hat{G_o}^{-1}(j\omega) G_o(j\omega) \right|, \quad \text{at frequency } \omega; \tag{3.6}$$

   where $\Delta G(j\omega)$ is the dynamics uncertainty as defined below

$$\Delta G(j\omega) = \frac{G_o(j\omega)}{G_{o,m}(j\omega)} = \Delta r(\omega) \cdot e^{j\Delta\theta(\omega)}. \tag{3.7}$$

   In (3.7), $G_{o,m}(j\omega)$ denote the model of the system plant $G_o(j\omega)$, and it is assumed that both the system plant $G_o(j\omega)$ and its model $G_{o,m}(j\omega)$ are hyperbolic. $\Delta r(\omega)$ and $\Delta\theta(\omega)$ denotes the magnitude and the phase variation, respectively.

2. The feedback controller i) complements the inversion-based optimal feedforward controller by increasing the bandwidth of the closed-loop system, and also ii) attains the desired requirements for robustness such that the sensitivity $S(j\omega)$ and the complementary sensitivity $T(j\omega)$ of the feedback control satisfy the given stability and robustness requirements, i.e.,

$$\left\| \begin{array}{c} W_P(j\omega)S(j\omega) \\ W_T(j\omega)T(j\omega) \\ W_u(j\omega)K(j\omega)S(j\omega) \end{array} \right\|_\infty \leq 1 \tag{3.8}$$

where $\|G(j\omega)\|_\infty$ denotes the H_∞ norm of the transfer function $G(j\omega)$ [45], $K(s)$ denotes the feedback controller, and $W_P(s)$, $W_T(s)$, and $W_u(s)$ are user-defined weighting functions to impose the requirements for the bandwidth and tracking performance ($W_p(s)$), the robustness against model uncertainties ($W_T(s)$), and the input magnitude ($W_u(s)$), respectively [45].

Our approach to solve the above control system design problem is based on the well-known *Bode's Integral*, which is stated and discussed as follows.

Lemma 4 Bode's Sensitivity Integral [45] *Suppose the open-loop system plant $G_o(j\omega)$ has a relative degree larger than one (i.e., has at least two more poles than zeros), and $G_o(j\omega)$ has N_p right-half-plan (RHP) poles at locations p_i. Then the closed-loop sensitivity function must satisfy*

$$\int_0^\infty ln\,|S(j\omega)|\,d\omega = \pi \cdot \sum_{i=1}^{N_p} Re(p_i) \tag{3.9}$$

where $Re(p_i)$ denotes the real part of p_i.

Remark 9 *In practice, the frequency response of the open-loop transfer function $G_o(j\omega)$ has to roll off at frequencies above the bandwidth frequency ω_c. Thus, if the open-loop system plant $G_o(j\omega)$ is stable, Bode's Integrals is reduced to an integral over a finite frequency interval as follows [45],[47]*

$$\int_0^{\omega_c} ln\,|S(j\omega)|\,d\omega = 0. \tag{3.10}$$

Moreover, for a stable system with a single real RHP-zero z, the Bode's integral can be approximately as [45]

$$\int_0^{z} ln\,|S(j\omega)|\,d\omega \approx 0. \tag{3.11}$$

Bode's integral applies to every feedback controller, no matter how it is designed. It implies that a reduction of the feedback sensitivity in one frequency range must be paid off with an increase of the feedback sensitivity in another frequency range. Therefore, small sensitivity

and large bandwidth cannot be achieved simultaneously. However, combined with Lemma 3, Bode's Integral also implies that with the help of a small feedforward gain-error (for example, in the low-frequency range), an increase of the feedback-sensitivity in one frequency range (for example, the low-frequency range) can be utilized to lower the feedback-sensitivity in another frequency range (for example, the middle-frequency range). As a result, the feedback bandwidth can be increased, leading to better disturbance rejection and/or output tracking. This idea is explored in the following development of the robust-inversion-based 2DOF controller design.

3.2.2 Robust-Inversion-Based Feedforward Control

We introduce a frequency-dependent gain-modulation into the system-inversion, as follows

$$G_{FF}(j\omega) = \hat{G_o}^{-1}(j\omega) = \alpha(\omega) \cdot G_{o,m}^{-1}(j\omega) \tag{3.12}$$

With this gain-modulated system-inverse as the feedforward controller, the goal for the feedforward controller design (3.6) is now transformed to seeking the optimal gain coefficient $\alpha(\omega)$, i.e. Equation (3.6) is transformed to

$$\min_{\alpha(\omega)} \sup_{\Delta G} \epsilon_{ff}(\omega) = \min_{\alpha(\omega)} \sup_{\Delta G} \left|1 - \alpha(\omega)\Delta G(j\omega)\right| \tag{3.13}$$

The solution to the above minimax problem (3.13) is given by the following Theorem.

Theorem 1 *At any given frequency ω, let the magnitude variation of the system dynamics $\Delta r(\omega)$ (defined in (3.7)) be bounded below and above by constants $\Delta r_{\min}(\omega) \in (0,\ 1]$ and $\Delta r_{\max}(\omega) \geq 1$, respectively. Then*

1. *The gain-modulated inversion-based feedforward controller (3.12) will enhance the tracking of the entire 2DOF control system if and only if*

   (a) *the size of the phase variation of the system dynamics, $\Delta\theta_m(\omega)$, is less than $\pi/2$, i.e., $\left|\Delta\theta(\omega)\right| \leq \Delta\theta_m(\omega) < \pi/2$; and*

   (b) *the gain coefficient $\alpha(\omega)$ is chosen as*

$$0 < \alpha(\omega) < \frac{2\cos(\Delta\theta_m(\omega))}{\Delta r_{\max}(\omega)};$$

2. *Particularly, the solution to the robust system-inversion problem (3.13) for all dynamics variations bounded by the constants* $\Delta r_{\min}(\omega), \Delta r_{\max}(\omega)$, *and* $\Delta\theta_m(\omega)$, *is given by*

$$\alpha_{opt}(\omega) = \frac{2\cos\left(\Delta\theta_m(\omega)\right)}{\Delta r_{\min}(\omega) + \Delta r_{\max}(\omega)}. \tag{3.14}$$

3. *By using the robust-inversion-based feedforward controller,* $\alpha_{opt}(\omega)G_{o,m}^{-1}(j\omega)$, *the feedforward gain-error is bounded above by the following constant* $\epsilon_{ff}^*(\omega)$,

$$\epsilon_{ff}^*(\omega) = \min_{\alpha(\omega)} \sup_{\Delta G} \left|1 - \alpha(\omega)\Delta G(j\omega)\right| = \sqrt{1 - \frac{4\cos^2\left(\Delta\theta_m(\omega)\right)\Delta r_{\min}(\omega)\Delta r_{\max}(\omega)}{\left(\Delta r_{\min}(\omega) + \Delta r_{\max}(\omega)\right)^2}}. \tag{3.15}$$

Proof Result 1 follows directly by substituting the gain-modulated inverse feedforward controller $\hat{G}^{-1}(j\omega) = \alpha(\omega)G_{o,m}^{-1}(j\omega)$ into (3.5), and quantifying the allowable dynamics variations, $\Delta r(\omega)$, $\Delta\theta_m(\omega)$, as well as the allowable range of the gain coefficient $\alpha(\omega)$. See Lemma 1 in Ref. [1] for details.

To show Result 2, we rewrite (3.13), at any given frequency ω, as follows

$$\begin{aligned}
\epsilon_{ff}^*(\omega)^2 &= \min_{\alpha} \sup_{\Delta r, \Delta\theta} |1 - \alpha\Delta G(j\omega)|^2 \\
&= \min_{\alpha} \sup_{\Delta r, \Delta\theta} |1 - \alpha\Delta r \cdot [\cos(\Delta\theta) + i\sin(\Delta\theta)]|^2 \\
&= \min_{\alpha} \sup_{\Delta r, \Delta\theta} |1 - \alpha\Delta r \cdot \cos(\Delta\theta) - i\alpha\Delta r \sin(\Delta\theta)|^2 \\
&= \min_{\alpha} \sup_{\Delta r, \Delta\theta} \left\{\alpha^2\Delta r^2\cos^2(\Delta\theta) + \alpha^2\Delta r^2\sin^2(\Delta\theta) + 1 - 2\alpha\Delta r \cdot \cos(\Delta\theta)\right\} \\
&= \min_{\alpha} \sup_{\Delta r, \Delta\theta} \Big\{[\alpha\Delta r - 1]^2 + 2\alpha\Delta r(1 - \cos(\Delta\theta))\Big\} \\
&= \min_{\alpha} \sup_{\Delta r} \Big\{[\alpha\Delta r - 1]^2 + 2\alpha\Delta r(1 - \cos(\Delta\theta_m))\Big\} \\
&\quad (\text{since } |\Delta\theta| \le \Delta\theta_m < \pi/2.)
\end{aligned} \tag{3.16}$$

where the dependence of the variables on the frequency ω has been omitted for economy. Since the function

$$f(\Delta r, \alpha) = [\alpha\Delta r - 1]^2 + 2\alpha\Delta r(1 - \cos(\Delta\theta_m)) \tag{3.17}$$

is quadratic of Δr with the coefficient for the 2-order term Δr^2 being positive ($\alpha^2 > 0$), the supremum of the function $f(\Delta r, \alpha)$ can only be achieved at the two boundary points, i.e., $\Delta r = \Delta r_{\max}$ or $\Delta r = \Delta r_{\min}$. Thus, Equation (3.16) is reduced to

$$\epsilon_{ff}^*(\omega)^2 = \min_{\alpha} \ \max\left\{f(\Delta r_{\max}, \alpha),\ f(\Delta r_{\min}, \alpha)\right\} \tag{3.18}$$

The above minimax problem is solved by seeking the optimal gain coefficient α_{opt} such that the two values in (3.18) equal to each other, i.e.,

$$\begin{aligned} f(\Delta r_{\max}, \alpha_{opt}) &= [\alpha_{opt}\Delta r_{\max} - 1]^2 + 2\alpha_{opt}\Delta r_{\max}(1 - \cos(\Delta\theta_m)) \\ &= [\alpha_{opt}\Delta r_{\min} - 1]^2 + 2\alpha_{opt}\Delta r_{\min}(1 - \cos(\Delta\theta_m)) = f(\Delta r_{\min}, \alpha_{opt}) \end{aligned} \quad (3.19)$$

Solving (3.19) leads to the optimal gain coefficient $\alpha_{opt}(\omega)$ in (3.14). Such a choice of the gain coefficient α is optimal, because for any given $\alpha \geq \alpha_{opt}$, the function $f(\Delta r_{\max}, \alpha)$, as a quadratic function of α as well, achieves its minimum value at $\alpha_1 = \cos(\Delta\theta_m)/\Delta r_{\max}$. By (3.14), it can be easily verified that $\alpha \geq \alpha_{opt} \geq \alpha_1$, and the function $f(\Delta r_{\max}, \alpha)$ is monotonically increasing with α when $\alpha \geq \alpha_1$, this implies that the quadratic function $f(\Delta r_{\max}, \alpha) \geq f(\Delta r_{\max}, \alpha_{opt})$ for all $\alpha \geq \alpha_{opt}$, i.e.,

$$\sup_{\Delta r} f(\Delta r, \alpha_{opt}) \leq \max\big\{f(\Delta r_{\max}, \alpha),\ f(\Delta r_{\min}, \alpha)\big\}, \quad \text{when } \alpha \geq \alpha_{opt}. \quad (3.20)$$

Similarly, for any given $\alpha \leq \alpha_{opt}$, we can show that $f(\Delta r_{\min}, \alpha) \geq f(\Delta r_{\min}, \alpha_{opt})$, which implies that

$$\sup_{\Delta r} f(\Delta r, \alpha_{opt}) \leq \max\big\{f(\Delta r_{\max}, \alpha),\ f(\Delta r_{\min}, \alpha)\big\}, \quad \text{when } \alpha \leq \alpha_{opt}. \quad (3.21)$$

Result 3 is obtained by substituting the optimal gain coefficient (3.14) back into either side of (3.19), and noticing that $\cos(\Delta\theta_m) > 0$. This completes the proof. ■

Remark 10 Geometric interpretation of Theorem 1 *As depicted in Fig. 3.2(a), for the magnitude variation $\Delta r \in [r_{\min}, r_{\max}]$ and the phase variation $\Delta\theta \in [-\theta_m, \theta_m]$, the shadowed area represents the set of all possible values of the feedforward gain-error vector $\overrightarrow{\epsilon_{ff}}(\omega, \Delta G, \alpha) = 1 - \alpha(\omega)\Delta G(j\omega)$. It is noted that the maximum feedforward gain-error $\left|\overrightarrow{\epsilon_{ff}}(\omega, \Delta G, \alpha)\right|$ can only be obtained at the two boundary points, i.e., $\overrightarrow{\epsilon_{ff,1}}$ or $\overrightarrow{\epsilon_{ff,2}}$ in Fig. 3.2 (a). For the case of $\left|\overrightarrow{\epsilon_{ff,1}}\right| > \left|\overrightarrow{\epsilon_{ff,2}}\right|$ depicted in Fig. 3.2 (a), the feedforward gain-error is bounded above by the magnitude of the vector $\overrightarrow{\epsilon_{ff,1}}$. Thus the gain coefficient $\alpha(\omega)$ needs to be decreased to reduce the feedforward gain-error. The decrease of the gain coefficient $\alpha(\omega)$, however, will increase the feedforward gain-error governed by the lower-bound of the dynamics*

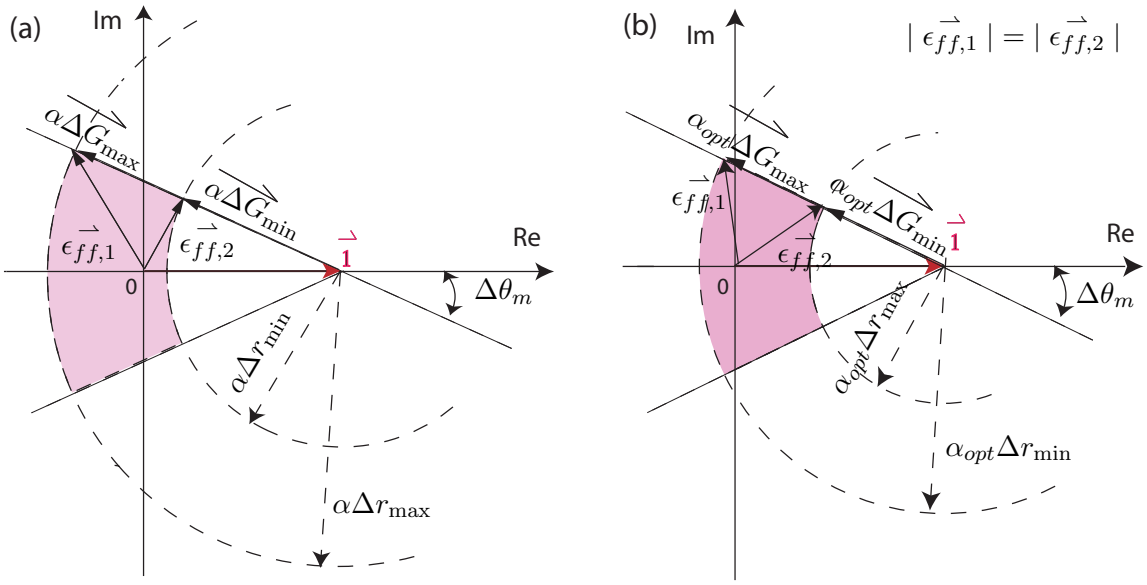

Figure 3.2 The geometric interpretation of the robust-system-inversion method: (a) the feedforward gain-error (shadowed area) for the dynamics uncertainties bounded by $\Delta r_{\min}, \Delta r_{\max}$, and $\Delta\theta_m$, with an arbitrarily chosen gain coefficient α, and (b) the minimized gain-error for the optimal gain coefficient α_{opt}.

variation, $\overrightarrow{\epsilon_{ff,2}}$. Therefore, the minimal supreme value of the feedforward gain-error is achieved when these two gain-errors are equal to each other, i.e., $\left|\overrightarrow{\epsilon_{ff,1}}\right| = \left|\overrightarrow{\epsilon_{ff,2}}\right|$, as depicted in Fig. 3.2 (b). By the law of cosines, the magnitudes of the two vectors $\overrightarrow{\epsilon_{ff,1}}$ and $\overrightarrow{\epsilon_{ff,2}}$ are given by the two expressions in (3.18), respectively (see Fig. 3.2 (a)). Thus, the above equivalence, $\left|\overrightarrow{\epsilon_{ff,1}}\right| = \left|\overrightarrow{\epsilon_{ff,2}}\right|$, is exactly the same as (3.19), which leads to the optimal gain coefficient as given in Theorem 1.

Remark 11 *It has been shown in Ref. [8] that when the exact inverse is used as the feedforward controller, i.e., $\alpha(j\omega) = 1$ in (3.12), the feedforward controller will enhance the tracking of the entire inversion-based 2DOF control system if and only if*

$$\left|G_o(j\omega) - G_{o,m}(j\omega)\right| < \left|G_o(j\omega)\right|. \tag{3.22}$$

Using the dynamics uncertainty as defined in (3.7), it can be verified that the above Condition is equivalent to requiring that the phase variation

$$\left|\Delta\theta_m(\omega)\right| < \cos^{-1}\left(\frac{1}{2\Delta r(\omega)}\right), \tag{3.23}$$

which is less than $\pi/2$. Therefore, a larger dynamics (phase) uncertainty can be allowed in the proposed robust inversion-feedforward controller—In implementations, the feedforward controller $\hat{G}_o^{-1}(j\omega)$ should set to zero at frequencies where the phase variation exceeds $\pi/2$.

Remark 12 Optimal Iterative Coefficient in the inversion-based iterative control (IIC) algorithm *[1, 23] We note that the same dynamics uncertainties allowed in Theorem 1 is also allowed in the recently-developed IIC algorithm [1] (to guarantee the convergence of the IIC algorithm). Moreover, the criteria for achieving the fastest possible convergence in IIC algorithm is also the same as that for achieving the optimal feedforward gain modulation (Eq. (3.13)). Therefore, the optimal gain coefficient $\alpha_{opt}(\omega)$ in Eq. (3.14) is also the optimal iterative coefficient to be used in the following IIC algorithm [1, 23]—for fastest guaranteed convergence rate in the presence of dynamics uncertainties bounded by $\Delta r_{\max}$, $\Delta r_{\min}$, and $\Delta\theta$:*

$$u_0(j\omega) \;=\; 0, \qquad u_{k+1}(j\omega) = u_k(j\omega) + \alpha(\omega)G_{a,m}^{-1}(j\omega)[x_d(j\omega) - x_k(j\omega)], \quad \textit{for } k \geq 1. \tag{3.24}$$

Corollary 1 *The robust-inverse feedforward controller $G_{FF}(j\omega)$ has no poles on the $j\omega$ axis, provided that the model of the system plant $G_{o,m}(j\omega)$ is hyperbolic (i.e., has no poles/zeros on the $j\omega$ axis).*

Proof We proceed by contradiction. Assume that the robust-inverse feedforward controller $G_{FF}(j\omega)$ has a pair of poles on the $j\omega$ axis, $\pm ja$ (with $a \in \Re$), then the frequency response of the feedforward controller $G_{FF}(j\omega)$ approaches to infinity as the frequency ω approaches to a, i.e., $G_{FF}(j\omega) \to \infty$ as $w \to a$. However, the hyperbolicity of the system model $G_{o,m}(j\omega)$ implies that its inverse $G_{o,m}^{-1}(j\omega)$ is also hyperbolic. The gain modulation term $\alpha(\omega)$ is less than 2 (by (3.14)), and thereby bounded for all frequency ω. This implies that the robust-inverse feedforward controller $G_{FF}(j\omega)$ is also bounded at all frequencies ω—a contradiction. This completes the proof. ■

3.2.3 Time-Domain Realization

We note that the obtained robust-inverse feedforward controller,

$$G_{FF}(j\omega) = \alpha_{opt}(\omega) G_{o,m}^{-1}(j\omega) = \hat{G}_o^{-1}(j\omega), \tag{3.25}$$

might be unstable and un-proper and thus cannot be implemented online. The implementation of such an unstable and un-proper controller has been addressed in the development of preview-based system-inversion technique [20, 48]. For completeness, we summarize below the main steps to realize the feedforward controller (3.25) in the time domain, the readers are referred to Ref. [20] for details.

1. If the obtained robust-inverse feedforward controller $\hat{G}_o^{-1}(j\omega)$ is not proper, obtain a proper, robust-inverse feedforward controller $\hat{G}_{o,p}^{-1}(j\omega)$ by redefining the output as follows,

$$u(j\omega) = \hat{G}_o^{-1}(j\omega) y_d(j\omega) = \frac{n_f(j\omega)}{d_f(j\omega)} y_d(j\omega) = \frac{n_{f,a}(j\omega)}{d_f(j\omega)} n_{f,b}(j\omega) y_d(j\omega) \triangleq \hat{G}_{o,p}^{-1}(j\omega) n_{f,b}(j\omega) \hat{y}_d(j\omega), \tag{3.26}$$

where the order of the numerator $n_{f,b}(j\omega)$ equals to the order difference between the denominator $d_f(j\omega)$ and the numerator $n_f(j\omega)$ (i.e., $\text{Order}(n_{f,b}) = \text{Order}(n_f) - \text{Order}(d_f)$),

and $\hat{y}_d(j\omega)$ is the modified desired output consisting of the output and its derivatives (Note it is assumed that the desired trajectory $\hat{y}_d(\cdot)$ is sufficiently smooth [5, 20].) Since the time-domain realization of a proper, stable transfer function is straightforward, next we only consider the realization of an unstable robust-inverse feedforward controller $\hat{G}_{o,p}^{-1}(j\omega)$.

2. Decouple the robust-inverse feedforward controller as the summation of the stable part and the unstable part by partial fraction expansion as

$$\hat{G}_{o,p}^{-1}(j\omega) = G_{ff,s}(j\omega) + G_{ff,u}(j\omega), \tag{3.27}$$

where $G_{ff,s}(j\omega)$ and $G_{ff,u}(j\omega)$ are the stable and the unstable part of the controller with all their poles on the open-left and open-right complex plan, respectively. Note such a decoupling can be done because the original robust-inverse controller $\hat{G}_o^{-1}(j\omega)$ is hyperbolic (Corollary 1), so is the proper robust-inverse controller $\hat{G}_{o,p}^{-1}(j\omega)$ [20]. Then find the minimal state-space realization (e.g.,[49]) of the stable and the unstable parts of the feedforward optimal controller as

$$\begin{aligned} \big[G_{ff,s}(s)\big] \quad : \qquad & \dot{x}_s(t) = A_s x_s(t) + B_s \hat{y}_d(t) \\ & u_{ff}^s(t) = C_s x_s(t) + D_s \hat{y}_d(t) \end{aligned} \tag{3.28}$$

$$\begin{aligned} \big[G_{ff,u}(s)\big] \quad : \qquad & \dot{x}_u(t) = A_u x_u(t) + B_u \hat{y}_d(t) \\ & u_{ff}^u(t) = C_u x_u(t) + D_u \hat{y}_d(t) \end{aligned} \tag{3.29}$$

3. Obtain the bounded feedforward input as the summation of the input portion from the stable dynamics, $u_{ff}^s(t)$, and the input portion from the unstable dynamics, $u_{ff}^u(t)$. Particularly, the unstable dynamics $\big\{A_u,\ B_u,\ C_u,\ D_u\big\}$ will be solved through a preview-based stable-inversion approach [20, 34, 48], which finds the unstable portion of the inverse input, $u_{ff}^u(t)$, by using a finite-preview of the future desired trajectory:

$$u_{ff}^s(t) = C_s \int_{-\infty}^{t} e^{A_s(t-\tau)} B_s \hat{y}_d(\tau) d\tau + D_s \hat{y}_d(t) \tag{3.30}$$

$$u_{ff}^u(t) = -C_u \int_{t}^{t+T_p} e^{-A_u(\tau-t)} B_u \hat{y}_d(\tau) d\tau + D_u \hat{y}_d(t) \tag{3.31}$$

$$u_{ff}(t) = u_{ff}^s(t) + u_{ff}^u(t) \tag{3.32}$$

Note in (3.31), the bounded solution to the unstable dynamics is noncausal and is obtained by using the previewed future desired trajectory within a finite preview time T_p. It can be shown [20, 34, 48] that the computation error, due to the use of finite (instead of infinity) previewed desired trajectory, can be rendered arbitrarily small by having a large enough preview time T_p. Furthermore, the amount of preview-time (for ensuring the precision of the feedforward control) can be quantified by the characteristics of the unstable part of the robust-inverse feedforward controller (3.29). Readers are referred to Ref. [20] for details.

3.2.4 Complementary Robust Feedback Controller Design

We note that although the proposed robust inversion feedforward control can minimize the dynamics uncertainty effect on the output tracking, the feedforward controller itself cannot reduce the effects of measurement noise and disturbance. Thus, feedback control is needed to reduce such adverse effects on the control performance. We propose to design the complementary feedback controller by integrating the above robust-inverse feedforward control with the H_∞ robust feedback control [45]. First, we will determine the upper-bound of the feedback sensitivity gain $|S(j\omega)|$ in the absence of feedforward control to meet the requirements in tracking performance and robustness, called the general upper-bound of the feedback sensitivity gain, $B_g(\omega)$. The sensitivity gain needs to be i) small in the low-frequency range to ensure a good tracking performance, ii) large in the high-frequency range to reject the noise and dynamics uncertainty effects, and iii) bounded above by a constant M across all frequencies to satisfy the robust stability requirement (e.g., [45]), i.e.,

$$|S(j\omega)| \leq B_g(\omega) \leq M \quad \text{for some } M > 0 \text{ and } \forall\ \omega \geq 0. \tag{3.33}$$

A typical general upper-bound of the sensitivity transfer function is shown in Fig. 3.3.

Then, the designed upper-bound of the feedback sensitivity $B_\ell(\omega)$ will be shaped by using the minimized feedforward gain-error, obtained in Subsection 3.2.2, to design the complementary upper-bound of the feedback sensitivity, $B_c(\omega)$, i.e., with the effect of the robust-inverse

feedforward control being considered. We note that when there is no feedforward control, the feedback sensitivity also represents the system's gain-error (with respect to the unit gain). Therefore, combining Lemma 3 with Theorem 1, it becomes evident that by using the robust-inverse feedforward control in the 2DOF system, the same gain-error can be maintained when the feedback sensitivity is scaled-up with the inverse of the less-than-one feedforward gain-error $\epsilon^*_{ff}(\omega)$ (see (3.16)), $B_g(\omega)/\epsilon^*_{ff}(\omega)$. Such a scaled-up upper-bound of the feedback sensitivity gain is depicted in Fig. 3.3. Moreover, we shall maintain the same feedback robustness stability in the 2DOF control system as that with feedback only, i.e., (3.33) should be satisfied. Therefore, the complementary upper-bound of the feedback sensitivity in the robust-inversion-based 2DOF control is chosen as:

$$|S(j\omega)| \leq B_c(\omega) = \min\{B_g(\omega)/\epsilon^*_{ff}(\omega),\ M\} \tag{3.34}$$

Equations (3.33, 3.34) show that in the low-frequency range, the feedback sensitivity of the 2DOF control system ($|S(j\omega)|$ in Eq. (3.34)) can be larger than that of the feedback control alone ($|S(j\omega)|$ in Eq. (3.33))—while maintaining the same tracking precision in that frequency range. Therefore, by the fact that Bode's Integral is a constant (see Lemma 4), such an increase of the feedback sensitivity in the low-frequency will enable a reduction of the feedback sensitivity in the transition frequency range. This implies that the transition-band of the feedback sensitivity can be pushed further into the higher frequency range. As a result, the bandwidth of the feedback control, measured by the frequency where the desired feedback sensitivity crosses -3dB from below [19], is increased. Such a desired feedback-sensitivity function, for the robust-inversion-based 2DOF control system, can be obtained by using the H_∞ robust feedback control technique, as described below.

First, the weighting function $W_{P,h}(j\omega)$ for the sensitivity function used in the H_∞ robust control design is chosen such that $|1/W_{P,h}(j\omega)| \leq B_c(\omega)$, for all ω. Such a weighting function will ensure that the obtained feedback sensitivity function $S(j\omega)$ will be bounded above by its upper-bound $B_c(\omega)$ given in (3.34). This is because the H_∞ feedback control design will seek

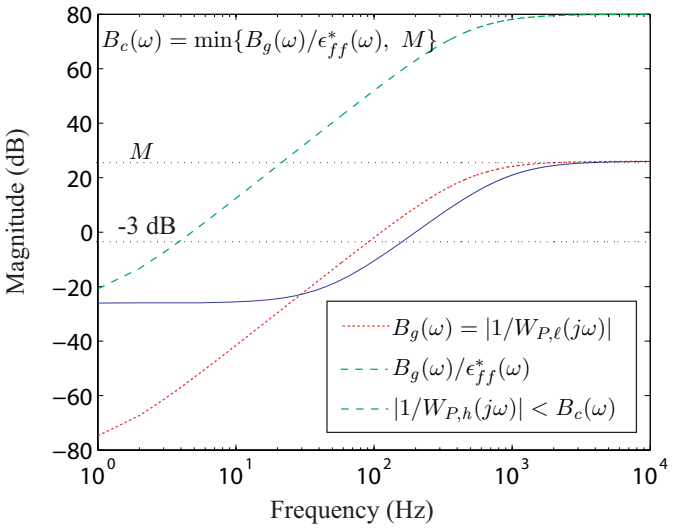

Figure 3.3 The illustrative plots of a general upper-bound of the feedback sensitivity which is designed without considering the feedforward control effect, $B_g(\omega) = |1/W_{P,\ell}(j\omega)|$, the scaled-up upper-bound with the minimized feedforward gain-error, $B_g(\omega)/\epsilon^*_{ff}(\omega)$, and the magnitude of the inverse of the sensitivity weighting function in the H_∞ control design that attains a larger feedback bandwidth, $|1/W_{P,h}(j\omega)|$. Note that for illustration purpose, the minimized feedforward gain-error $\epsilon^*_{ff}(\omega)$ is chosen as constant.

to achieve [45]

$$||W_{P,h}(j\omega)S(j\omega)||_\infty \leq 1.$$

Such a sensitivity weighting function $W_{P,h}(j\omega)$ is depicted in Fig. 3.3. As we expect, the sensitivity weighting function $W_{P,h}(j\omega)$ is reduced in the low frequency range, and thereby a larger feedback bandwidth is achieved (this is verified by our experimental example in Sec. 3.3). We note that if the disturbance d mainly appears in the low-frequency range, such a decrease of the weighting function may compromise the disturbance rejection of the closed-loop system. However, there exist applications where disturbances tend to be mainly occur in the high-frequency range. Thus for such cases, the weighting function $W_P(j\omega)$ can be reduced as described above. The resulted closed-loop bandwidth increase will improve both the tracking (of the reference trajectory r) and the rejection (of the disturbance d).

Second, to impose the closed-loop robustness and noise rejection on the complementary sensitivity transfer function $T(j\omega)$, the corresponding weighting function $W_T(j\omega)$ is chosen such that

$$||W_T(j\omega)T(j\omega)||_\infty \leq 1.$$

Finally, to impose the input saturation requirement on the loop transfer function $K(j\omega)S(j\omega)$, the weighting function on the input $W_u(j\omega)$ is chosen such that

$$||W_u(j\omega)K(j\omega)S(j\omega)||_\infty \leq 1.$$

It is noted that the weighting function $W_u(j\omega)$ can be designed by considering the saturation in the presence of both the feedforward and the feedback control. In the chapter, we simplify the design by only considering the feedback-caused saturation effect, and accounting for the feedforward control effect by setting the limit of the feedback control saturation to be an half of that for the total 2DOF system.

Once all the three weighting functions, $W_P(j\omega)$, $W_T(j\omega)$ and $W_u(j\omega)$, are chosen, the H_∞ feedback controller can be readily obtained by solving the H_∞ optimization robust feedback problem (3.8) by using existing methods, e.g., [45].

3.3 Example: Piezoelectric Actuator Design

Next, we illustrate the robust-inversion-based 2DOF controller design by implementing it to the piezoelectric actuator on an AFM. We start by describing the use of the piezo actuators in the AFM operation.

3.3.1 System Description

The AFM system ($Dimension^{TM}$ 3100, Veeco Inc) studied in this chapter utilizes piezotube actuators to position the AFM probe with respect to the sample during imaging (see Fig. 3.4 (a)), in both parallel (along the x-y axes) and perpendicular (along the z-axis) directions. The AFM probe motion signal is used to construct the topography of the sample, and/or to interrogate the sample properties [50]-[53]. Therefore, positioning errors of the probe relative to the sample will generate large image distortions [20, 3], and further damage the probe [28], the sample [29], or both. Such large positioning errors can be generated in both lateral scanning x-axis and vertical z-axis direction when imaging relatively-large samples at high-speed. In the experiment, inversion-based robust 2DOF control is used for the *periodic* scanning along the lateral x-axis direction (Fig. 3.4 (b)).

3.3.2 Design of the Robust-Inversion-Based Feedforward Controller

We experimentally measured the frequency response of the piezotube actuator in the lateral scanning (x-axis) direction, $\hat{G}_o(j\omega)$, and quantified the model uncertainties $\Delta G(j\omega)$ (as defined in (3.7)) by using a data acquisition system along with MATLAB toolboxes (System Identification Toolbox, Simulink and xPC Target). To measure the frequency response $G_o(j\omega)$, a band-limited white noise signal $u(t)$ generated using MATLAB-Simulink was applied to the piezo actuator through a power amplifier, and the x-axis displacement of the actuator $x(t)$ was measured (using an inductive sensor) and utilized to obtain the frequency response $G_o(j\omega)$ (by using the MATLAB-System Identification Toolbox). To experimentally quantify the model uncertainties, the frequency responses of the x-axis piezotube actuator were measured at three different input levels (60mV, 70mV, 80mV) around seven different initial

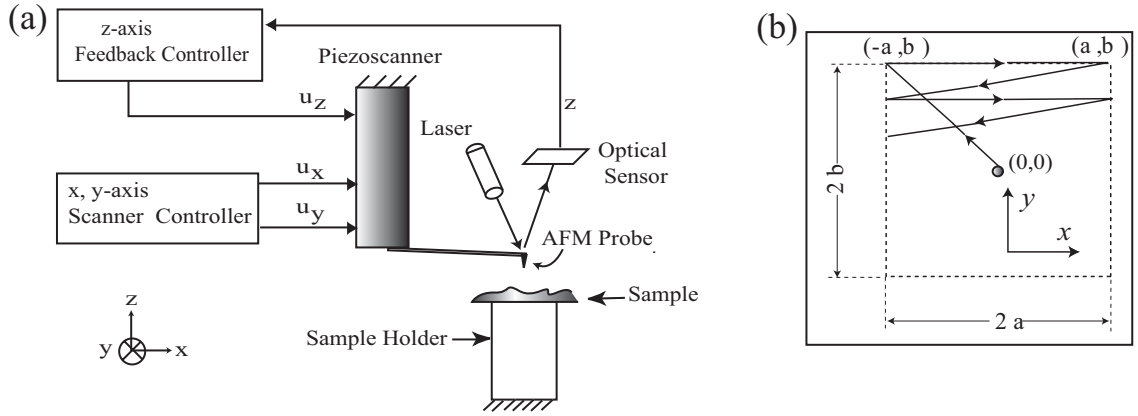

Figure 3.4 (a) the schematic diagram of the AFM operation, and b) the top view of the typical scanning trajectories for AFM imaging [1].

positions (origin, $\pm 10\mu m$, $\pm 20\mu m$, $\pm 30\mu m$). The total of 21 frequency responses measured are plotted in Fig. 3.5, from which the bound of the gain uncertainty, $\Delta r_{\max}(\omega)$ and $\Delta r_{\min}(\omega)$, and the phase uncertainty, $\Delta\theta(\omega)$, were estimated by finding the minimum and the maximum variations among the experimental frequency responses, as shown in Fig. 3.6(a) (b). Then the nominal frequency response used in the robust-inversion-based 2DOF design, $G_{o,m}(j\omega)$, was obtained by averaging these measured frequency responses.

The estimated bounds of magnitude and phase uncertainties were used, according to Theorem 1, to obtain the optimal gain coefficient, $\alpha_{opt}(\omega)$, and to further obtain the minimized upper-bound of the feedforward gain-error, $\epsilon^*_{ff}(\omega)$, as shown in Fig. 3.6 (c) and (d), respectively. Note that the feedforward gain-error is bounded above at 1.5% in the low frequency range till around 1100 Hz. As a result, Lemma 3 implies that the upper-bound of the feedback sensitivity, in the following feedback controller design part, can be increased by almost two orders of magnitude while still maintaining the same small gain-error of the entire 2DOF system in the low frequency range.

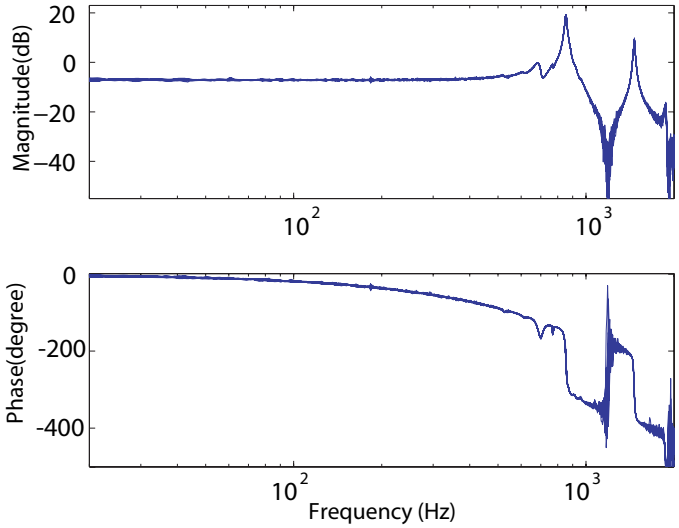

Figure 3.5 The experimentally measured frequency responses of the piezo actuator in the x-axis direction for different input voltage level and at different initial positions (up to 2KHz).

We note that although the feedforward gain-error (Fig. 3.6(c)) was small (except around the zero at 1179 Hz) till the frequency of 1800 Hz, the gain of the piezo actuator itself becomes much smaller than the DC-Gain as frequency increases beyond 1500 Hz (see Fig. 3.5). Therefore, in the experiment, the robust-inversion-based feedforward controller was chosen as

$$G_{FF,r}(j\omega) = \begin{cases} \alpha_{opt}(j\omega) G_{o,m}^{-1}(j\omega) & \omega \leq 1500 \text{ Hz} \\ 0 & \text{otherwise} \end{cases} \tag{3.35}$$

For comparison, the following exact-inverse feedforward controller was also implemented in the experiments (see Remark 11)

$$G_{FF,e}(j\omega) = \begin{cases} G_{o,m}^{-1}(j\omega) & \omega \leq 1100 \text{ Hz} \\ 0 & \text{otherwise} \end{cases} \tag{3.36}$$

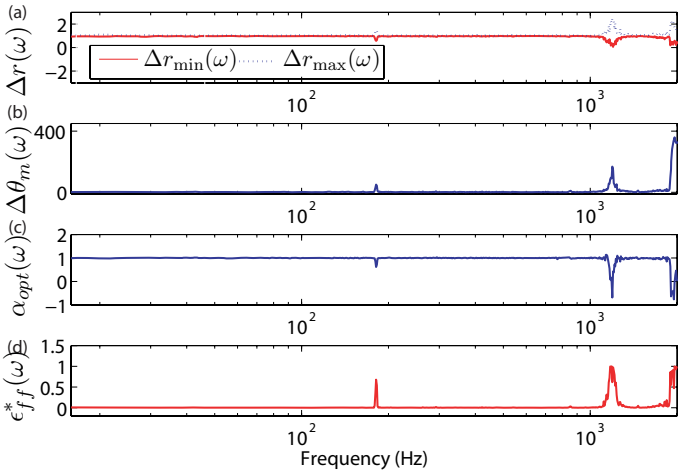

Figure 3.6 The experimentally measured magnitude variation $\Delta r_{\max}(\omega)$ and $\Delta r_{\min}(\omega)$ (a), and the phase variation $\Delta\theta_m(\omega)$ (b), and the calculated optimal gain $\alpha_{opt}(\omega)$ (c) and the minimized feedforward gain-error $\epsilon^*_{ff}(\omega)$ (d).

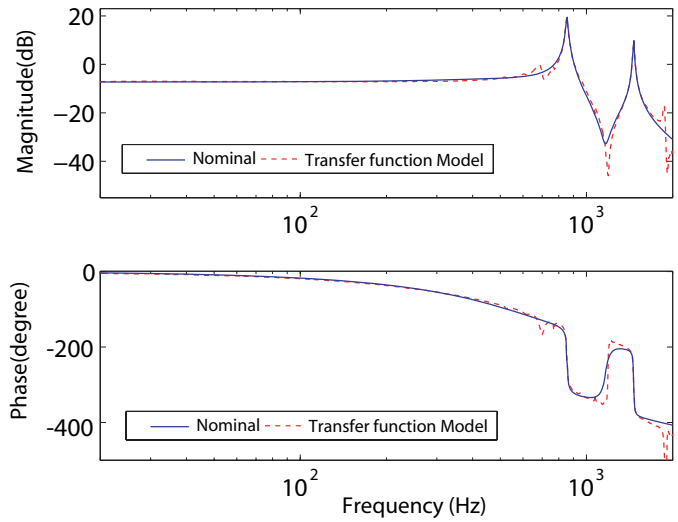

Figure 3.7 The comparison of experimentally-measured nominal frequency response with the frequency response of the transfer function model for the x-axis piezo actuator.

3.3.3 Complementary Robust Feedback Controller Design

We start by obtaining the transfer function of the x-axis piezo actuator, as given below, by curve fitting the nominal frequency response (MATLAB command "`invfreqs`"):

$$G_x(s) = \frac{8.942 \times 10^5 (s^2 - 3.39 \times 10^4 s + 3.11 \times 10^8)(s^2 + 411.7s + 5.357 \times 10^7)}{(s^2 + 5250s + 1.41 \times 10^7)(s^2 + 82.02s + 2.887 \times 10^7)(s^2 + 72.67s + 8.437 \times 10^7)} \quad (3.37)$$

The frequency response of the obtained model is compared with the nominal experimental responses in Fig. 3.7, which shows that the transfer function model captured the system dynamics closely till 1100 Hz. Next, we specify the general upper-bound of the feedback sensitivity function, $B_g(\omega)$, by choosing the following weighting function $W_{P,\ell}(s)$ for the feedback sensitivity,

$$W_{P,\ell}(s) = \frac{0.05s^2 + 309.1s + 4.777 \times 10^5}{s^2 + 13.82s + 47.77}. \quad (3.38)$$

Such a choice of weighting function leads to the general upper-bound of the feedback-sensitivity $B_g(\omega)$ as shown in Fig. 3.8, which has a gain as small as 0.1% for frequency < 1 Hz and smaller than 5% till around 100 Hz.

Next, the upper-bound of the feedback sensitivity in the robust-inversion-based 2DOF control system, $B_c(\omega)$, was obtained by shaping the above upper-bound of the feedback sensitivity $B_g(\omega)$. Particularly, it was noted that the minimized feedforward gain-error is less than 0.2% in the low frequency range ($< 10Hz$), and the general upper-bound $B_g(\omega)$ is bounded above at 26.02dB (or equivalently, 20). Therefore, by (3.34), we chose $B_c(\omega) = \min\{B_g(\omega)/0.002,\ 20\}$. For this complementary upper-bound $B_c(\omega)$, the feedback sensitivity weighting function $W_{P,h}(s)$ in the robust-inversion-based 2DOF control design was chosen as

$$W_{P,h}(s) = \frac{0.05s^2 + 562s + 1.579 \times 10^6}{s^2 + 562s + 7.896 \times 10^4}, \quad (3.39)$$

As shown in Fig. 3.8 (a), with such a choice of weighting function, the feedback sensitivity for the inversion-based 2DOF system is bounded above at 5% till around 160 Hz, and has the same robustness stability property as in the feedback-only design in the high-frequency range.

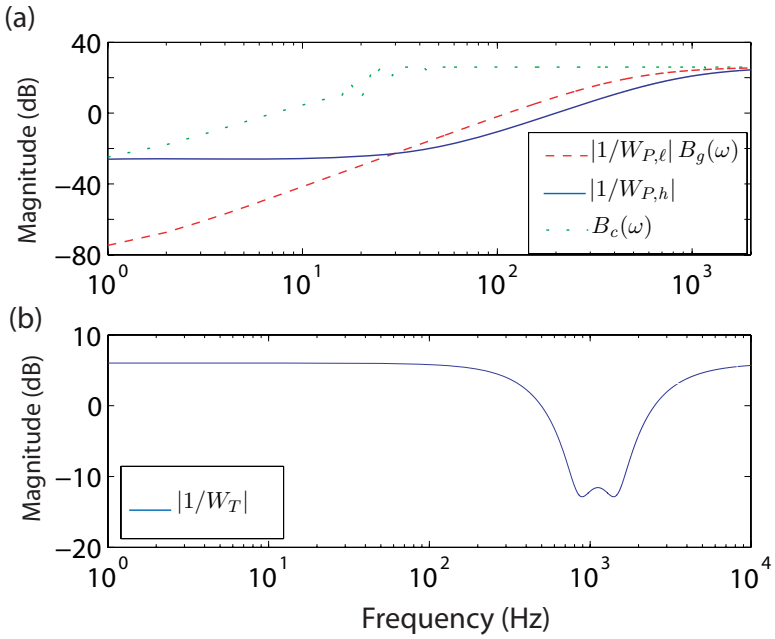

Figure 3.8 (a) Shows the desired upper-bound of feedback sensitivity designed without considering the effect of the feedforward control, $B_g(\omega)$, with considering the effect of the feedforward control, $B_c(\omega)$, and the corresponding inverses of the desired feedback sensitivities, $|1/W_{P,\ell}(j\omega)|$ and $|1/W_{P,h}(j\omega)|$; (b) shows the weighting function on the feedback complementary sensitivity transfer function, $W_T(j\omega)$.

To satisfy the robust performance requirement and account for the model uncertainty around the resonant peaks, the weighting function for the complimentary transfer function, $W_T(s)$ (as shown in Fig. 3.8 (b)), was chosen to be

$$W_T(s) = \frac{0.5s^4 + 1.213 \times 10^4 s^3 + 1.252 \times 10^8 s^2 + 5.988 \times 10^{11} s + 1.218 \times 10^{15}}{s^4 + 4853s^3 + 1.187 \times 10^8 s^2 + 2.395 \times 10^{11} s + 2.436 \times 10^{15}}. \quad (3.40)$$

It is noted that an analog low pass filter was added after the raw sensor signal to attenuate the noise effect in our experimental system. The cut-off frequency at 2 KHz was much higher than the closed-loop bandwidth, thereby for simplicity, its dynamics was ignored when designing the weighting function $W_T(s)$.

Moreover, to prevent the input saturation, the weighting function for the input, $W_u(s)$, is selected to be a constant $W_u(s) = 0.5$. Using these weighting functions $W_{P,h}(s)$, $W_T(s)$, and $W_u(s)$ in the robust criteria (3.8), the robust feedback controller was obtained numerically in MATLAB (MATLAB command "`hinfsyn`") as follows

$$\begin{aligned} G_{FB,h}(s) &= \frac{k \cdot \prod_{i=1}^{11}(s - z_i)}{\prod_{j=1}^{12}(s - p_j)} \quad \text{with} \quad k = 5.48 \times 10^6, \text{and} \\ z_i &= \{-810.13, -36.336 \pm 9185.1i, -1530. \pm 9056.8i, \\ &\quad -41.012 \pm 5372.6i, -895.51 \pm 5297.9i, -2624.9 \pm 2685.4i\} \\ p_i &= \{-2 \times 10^6, -7008, -889 \pm 9980i, -1522 \pm 8694i, \ . \\ &\quad -724.34 \pm 6840.8i, -1252.1 \pm 5005i, -281, -281\} \end{aligned} \quad (3.41)$$

For comparison, we also designed the feedback controller without considering the effect of the feedforward controller. By using the specified sensitivity weighting function $W_{P,\ell}(s)$ as in (3.38), and the same weighting functions on complementary sensitivity and the input, $W_T(s)$ as given by (3.40), and $W_u = 0.5$, the non-complementary controller transfer function was

obtained as follows

$$G_{FB,\ell}(s) = \frac{k \cdot \prod_{i=1}^{11}(s - z_i)}{\prod_{j=1}^{12}(s - p_j)} \quad \text{with} \quad k = 2.98 \times 10^6, \text{and}$$

$$\begin{aligned} z_i = \{&-36 \pm 9185i, -1531 \pm 9057i, -41 \pm 5373i, \\ &-896 \pm 5298i, -2625 \pm 2685i, -305.49\} \\ p_i = \big\{&-1.24 \times 10^6, -6874, -887 \pm 9965i, -1516 \pm 8690i, \\ &-725 \pm 6830i, -1255 \pm 4989i, -6.91, -6.91\} \end{aligned} \tag{3.42}$$

The frequency responses of the closed-loop sensitivity $S(j\omega)$ by using the two feedback controllers, respectively, were simulated in MATLAB, and also experimentally measured. As compared in Fig. 3.9 (a), (b), the experimentally measured feedback sensitivities were close to their simulation counterparts. Moreover, the experimental results showed that the proposed robust-inversion-based 2DOF control design can achieve a larger feedback bandwidth: the feedback bandwidth of the complementary feedback controller $G_{FB,h}(j\omega)$ at 164 Hz was over 28% times higher than the feedback bandwidth of the non-complementary robust feedback controller $G_{FB,\ell}(j\omega)$ at 128 Hz. Furthermore, we also note that the phase of the feedback sensitivity for the complementary feedback controller $G_{FB,h}(j\omega)$, i.e., the phase error of the output tracking, was smaller, in the low-frequency range (till $\sim$ 110 Hz), than that for the non-complementary robust feedback controller.

It is noted that the experiments might be further improved by designing the weighting functions more carefully through the noise and disturbance analysis. We further note that the same weighting functions $W_T(s)$ and $W_u(s)$ were used to design the feedback controllers in both cases (the proposed complementary design, and the general 2DOF design), therefore such a more careful design of the weighting functions $W_T(s)$ and $W_u(s)$ will benefit the performance of both controller designs.

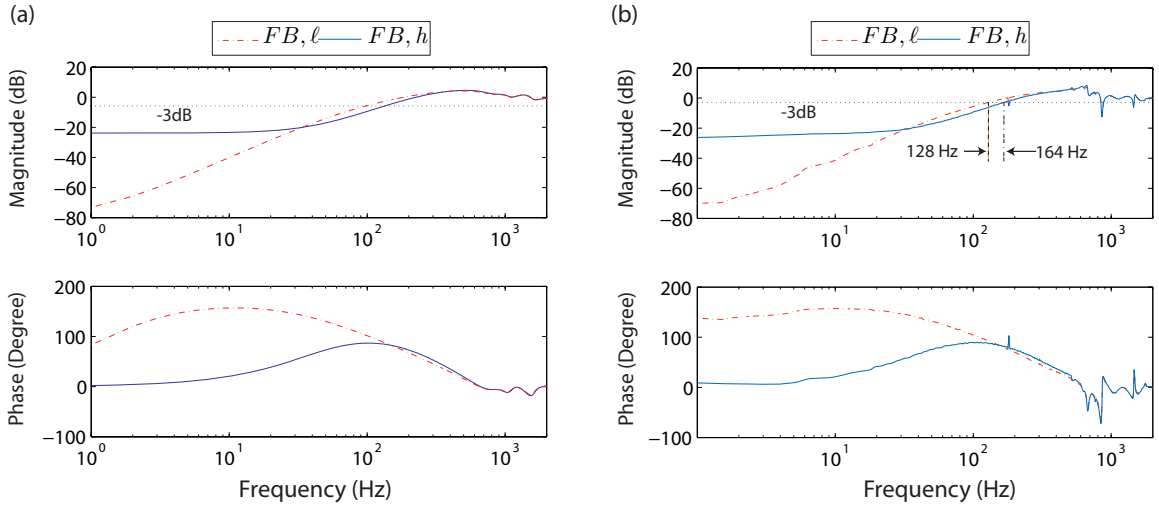

Figure 3.9 Comparison of the simulation (a) and the experimentally measured frequency response (b) of the feedback sensitivity by using the complementary robust feedback controller ('FB, h') with that by using the non-complementary robust feedback controller ('FB, ℓ').

3.3.4 Experimental Results and Discussion

Experiments were conducted to track a triangular trajectory at seven different frequencies (10Hz, 50Hz, 100Hz, 150Hz, 200Hz, 250Hz and 300Hz) by using three different control approaches: 1). the feedback controller $G_{FB,\ell}(s)$ alone; 2). the exact inverse feedforward controller $G_{FF,e}(s)$ in (3.36) along with the non-complementary robust feedforward controller $G_{FB,\ell}(s)$ in (3.42); and 3). the robust-inversion-based 2DOF robust approach, i.e., the robust-inverse feedforward controller $G_{FF,r}(s)$ in (3.35) along with the complementary robust feedback controller $G_{FB,h}(s)$ in (3.41). The output range was chosen at 5 μm. The obtained tracking results for the triangular signal frequencies at 10, 100, and 250 Hz are compared in Fig. 3.10. The tracking performance of the three different control approaches for all seven triangular signal frequencies are compared in Table 3.1 in terms of the RMS error E_{RMS}, the maximum

error E_M, and the relative maximum error $\widehat{E}_M$, where

$$\begin{aligned} E_{RMS}(\mu m) &= \sqrt{\frac{(\sum_{k=1}^{n}(x_d[k]-x[k])^2)}{n}}, \\ E_M(\mu m) &= \max_{k\in[0,n]}|x_d[k]-x[k]|, \\ \widehat{E}_M(\%) &= \frac{E_M}{\max_{k\in[0,n]}|x_d|}\times 100\%. \end{aligned} \tag{3.43}$$

Table 3.1 Comparison of the tracking errors obtained by using the feedback controller $G_{FB,\ell}$ only (A), the exact-inverse feedback controller $G_{FF,e}$ with the non-complementary robust feedback controller $G_{FB,\ell}$ (B), and the proposed robust-inversion-based 2DOF control ($G_{FB,h}+G_{FF,r}$) (C). Displacement range: 5 μm.

triangular Rate	$E_{RMS}(\mu m)$			$E_M(\mu m)$			$\hat{E}_M(\%)$		
(Hz)	**(A)**	**(B)**	**(C)**	**(A)**	**(B)**	**(C)**	**(A)**	**(B)**	**(C)**
10	0.0315	0.0136	0.0149	0.1852	0.0724	0.0734	3.70	1.45	1.47
50	0.3085	0.0191	0.0160	0.7824	0.0829	0.0625	15.65	1.66	1.25
100	0.7748	0.0430	0.0331	1.3634	0.1332	0.1216	27.27	2.66	2.43
150	N/A	0.0593	0.0426	N/A	0.1478	0.1079	N/A	2.96	2.16
200	N/A	0.0773	0.0532	N/A	0.1772	0.1497	N/A	3.54	2.99
250	N/A	0.1129	0.0891	N/A	0.2724	0.2063	N/A	5.45	4.13
300	N/A	0.1341	0.0958	N/A	0.3772	0.2642	N/A	7.54	5.28

The experimental results show that when the triangular rate was low, precision output tracking can be achieved with the feedback controller alone. As shown in Fig. 3.10, at the signal frequency of 10 Hz, the relative maximum tracking error by using the feedback controller $G_{FB,\ell}(s)$ was 3.70%. As the signal speed was increased, however, the tracking error became much larger. Particularly, at the signal frequency of 100 Hz, the main frequency components of the desired signal other than the fundamental frequency component were outside the bandwidth of the feedback control system at 128 Hz (see Fig. 3.9). As a result, large tracking errors occurred–the relative maximum error was over 27.27% for 100Hz tracking. Therefore, output tracking by using the non-complementary feedback controller $G_{FB,\ell}(j\omega)$ alone was not proceeded in experiments for triangular signals with frequency higher than 100 Hz.

The output tracking performance can be significantly improved by using the inversion-based 2DOF control technique (including both the proposed robust-inversion-based 2DOF control and the inverse-based feedforward control with the non-complementary feedback control). As shown in Fig. 3.10 and Table 3.1, for the triangular signal at 10 Hz, the maximum tracking error achieved by using the inversion-based 2DOF controller was only about 0.0724 μm (the equivalent voltage equals to 12.1 mV), which was close to the noise level of the experimental system (at 10.1 mV, measured as the maximum value with respect to its mean value). For triangular trajectory with higher frequencies, the tracking error achieved with the inversion-based 2DOF control techniques was also significant smaller than using the feedback controller alone. For example, at the triangular frequency of 100 Hz, the tracking error achieved by using the inversion-based 2DOF controller was about 10 times smaller than using the feedback controller alone. Even for the high-speed triangular signal of 250 Hz, the obtained relative maximum tracking error was still less than 6%.

The experimental results also show that the proposed robust-inversion-based 2DOF control, $G_{FF,r}(s) + G_{FB,h}(s)$, can further improve the tracking at high-speed, compared with the exact- inverse feedforward, non-complementary robust-feedback 2DOF control, $G_{FF,e}(ss) + G_{FB,\ell}(s)$. As described in Sec. 3.3.2, the designed robust-inversion-based feedforward controller $G_{FF,r}(j\omega)$ in (3.35) achieved smaller feedforward gain-error as well as larger frequency range for precision output tracking than the exact feedforward control (Remark 11); Moreover, as described in Sec. 3.3.3, the complementary robust feedback controller $G_{FB,h}(j\omega)$ achieved a higher feedback bandwidth than the non-complementary feedback controller $G_{FB,\ell}(j\omega)$ (see Fig. 3.9). Therefore, the 2DOF controller $G_{FF,r}(s)+G_{FB,h}(s)$ obtained by using the proposed approach attained a larger "total" bandwidth than the 2DOF controller $G_{FF,e}(ss)+G_{FB,\ell}(s)$, which, in turn, results in higher tracking precision at high-speed. As shown in Table 3.1, the proposed robust-inversion-based 2DOF controller achieved higher tracking precision for all triangular frequencies but 10 Hz than the non-complementary inversion-based 2DOF controller.

For example, at the triangular trajectory of 250 Hz, the tracking error obtained by using the proposed robust-inversion-based 2DOF controller was 25% smaller than that obtained by the controller $G_{FF,e}(ss) + G_{FB,\ell}(s)$.

To further evaluate the proposed control approach, the two inversion-based 2DOF controllers were also applied to track triangular trajectories at a much larger displacement range of 50 μm. It is noted that the nonlinear hysteresis effect is pronounced at this large displacement range [54], and the quantification of the dynamics variation obtained in Sec. 3.3.2 did not adequately account for the range-dependent hysteresis effect (To do so, a much larger input level in the measured frequency range of 2 KHz needs to be applied to the piezo actuator, which can potentially damage the piezo actuator, thereby was not pursued in the experiments). However, the experimental results show that the proposed control approach can still achieve precision tracking at high-speed for such large output-range. As shown in Table 3.2 and Fig. 3.11, for the triangular signal at 10 Hz, the relative maximum tracking error $\hat{E}_M(\%)$ is only $\sim 0.67\%$ of the displacement range; even when the frequency of the triangular signal was increased to 100 Hz, the tracking error was still small at $\hat{E}_M(\%) = 3.60\%$, only 1/7 of the error when using feedback alone. Therefore, the experimental results demonstrate that the proposed robust-inversion-based 2DOF control approach can achieve precision output-tracking at high-speed.

Table 3.2 Comparison of the tracking errors for large-range tracking (50 μm) obtained by using the feedback control $G_{FB,\ell}$ alone (A), the inverse 2DOF control $G_{FF,e}(s)+G_{FB,\ell}(s)$ (B), and the proposed 2DOF control $G_{FF,r}(s) + G_{FB,h}$ (C).

triangular Rate	$E_{RMS}(\mu m)$			$E_M(\mu m)$			$\hat{E}_M(\%)$		
(Hz)	**(A)**	**(B)**	**(C)**	**(A)**	**(B)**	**(C)**	**(A)**	**(B)**	**(C)**
10	0.2401	0.0487	0.1591	1.4505	0.2854	0.3384	2.90	0.57	0.67
50	2.4482	0.4268	0.3313	7.0059	0.9869	0.9428	14.01	1.97	1.88
100	6.2142	1.1114	0.8070	13.2612	1.9651	1.7994	26.52	3.93	3.60
150	N/A	1.9025	1.5903	N/A	3.0362	3.3377	N/A	6.07	6.68

3.4 Conclusion

A robust-inversion-based 2DOF control design approach for output tracking was proposed in this chapter. A novel robust-inversion technique is developed, which, when used as a feedforward control, achieved a guaranteed tracking precision in the presence of bounded dynamics variations from the feedforward control. The bounded feedforward gain-error was then used in the H_∞ robust feedback control to design a robust feedback controller to complement the feedforward control and increase the feedback bandwidth under the robust stability requirements. Therefore, the proposed approach, for the first time, systematically integrated the system-inversion-based feedforward control with the H_∞ robust feedback control together. The implementation of the proposed method on piezotube actuator of an AFM is presented to show that 1) the proposed approach achieved a larger feedback-bandwidth of the entire system than that by using the regular robust H_∞ design; and 2) high-speed precision output tracking can be achieved by using the proposed robust-inversion-based 2DOF control technique.

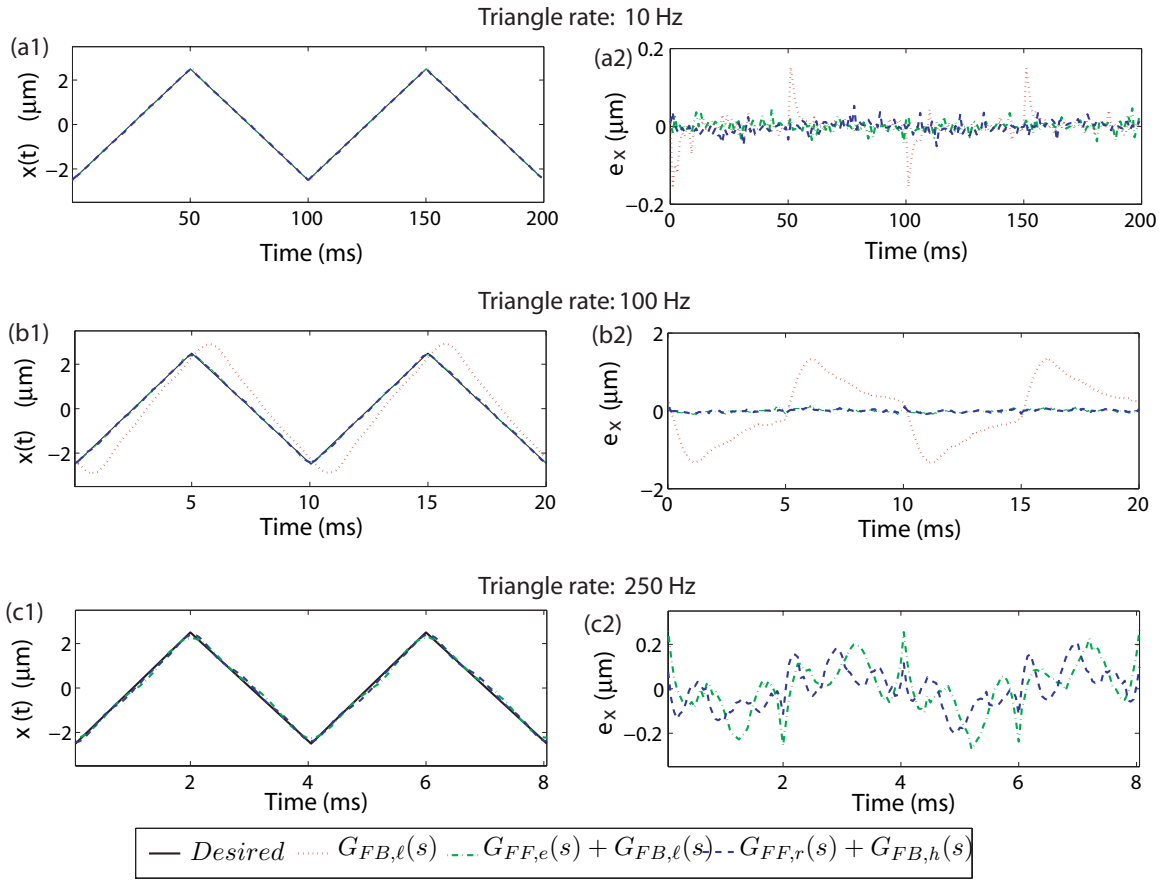

Figure 3.10 Comparison of the experimental tracking results (left column) and the tracking errors (right column) obtained by using three different control approaches for tracking the triangular trajectory with frequencies of 10 Hz (a1, a2), 100 Hz (b1, b2), and 250 Hz (c1, c2). The displacement range is 5 μm.

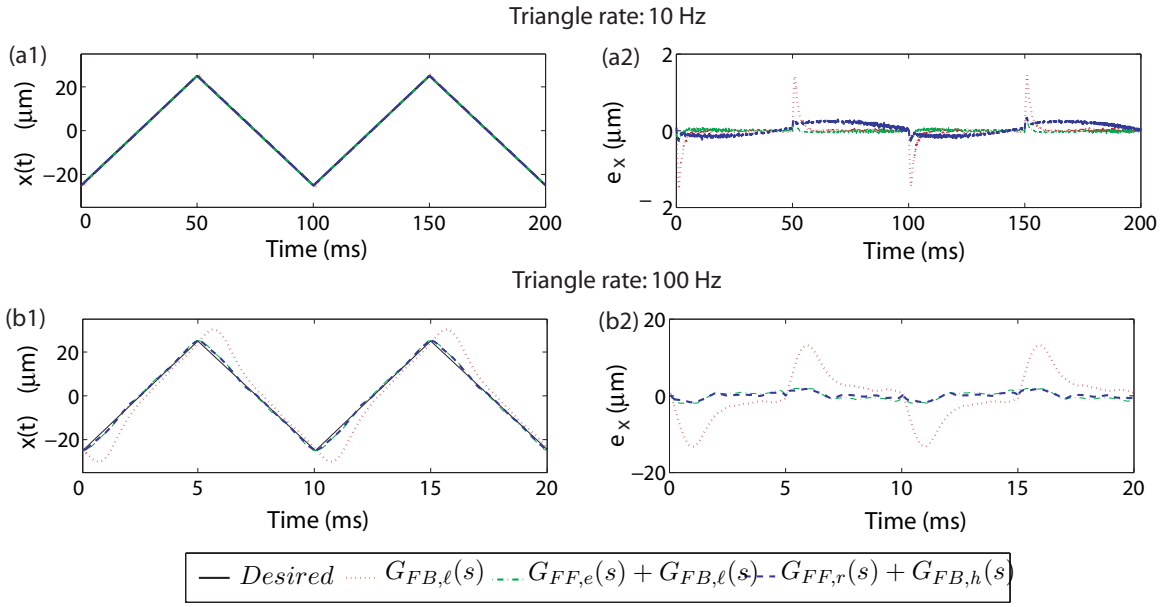

Figure 3.11 Comparison of the experimental tracking results (left column) and the tracking errors (right column) obtained by using three different control approaches for tracking the triangular trajectory with frequency 10 Hz (a1, a2), and 100 Hz (b1, b2). The displacement range is 50 μm.

CHAPTER 4. A current cycle feedback iterative learning control approach for AFM imaging

A paper published in IEEE Transactions on Nanotechnology

Ying Wu [1] and Qingze Zou [2]

Abstract

In this chapter, we proposed a novel current cycle feedback (CCF) iterative learning control (ILC) approach to achieve high-speed imaging on atomic force microscope (AFM). AFM-imaging requires precision positioning of the AFM probe relative to the sample in 3-D (x-y-z). It has been demonstrated that, with advanced control techniques such as the inversion-based iterative-control (IIC) technique, precision positioning of the AFM probe in the lateral (x-y) scanning can be successfully achieved. Precision positioning of the probe in the vertical z-axis direction, however, is still challenging because of the issues such as the sample topography is unknown in general, the probe-sample interaction is complicated, and the probe-sample position is sensitive to the probe-sample interaction. The main contribution of this chapter is the development of the CCF-ILC approach to the AFM z-axis control, which decouples the robustness of the feedback control from the tracking precision of the feedforward control. Particularly, the proposed CCF-ILC controller design utilizes the recently-developed robust-inversion technique to minimize the model uncertainty effect on the feedforward control, and to remove the causality constraints in other CCF-ILC approaches. It is shown that the iterative law converges, and attains a bounded tracking error upon noise and disturbances. The proposed

[1] Primary researcher and author
[2] corresponding Author

method is illustrated through experimental implementation and the experimental results show an increase of imaging speed.

4.1 Introduction

In this chapter, we propose a current circle feedback (CCF) iterative learning control (ILC) approach for tracking the unknown sample topography during AFM imaging. The nanoscale resolution of AFM has made AFM an enabling tool to image as well as to manipulate matter at nano-scale (e.g., [55, 56]). Current AFM, however, is slow and AFM imaging is time consuming. Such slow speed of AFM has also hindered the use of AFM to interrogate nanoscale dynamic phenomena [57, 58]. AFM imaging requires the precision positioning of the probe relative to the sample in all three axes (x, y, z). It has been demonstrated that with advanced control techniques [54, 17, 18] such as the inversion-based iterative control (ILC) [54], precision positioning of the AFM probe at high speed can be successfully achieved in the lateral (x, y-axes) scanning. Challenges, however, must be overcomed to achieve the precision positioning of the probe in the vertical z-axis because of the issues such as the sample topography is unknown in general, the probe-sample interaction is complicated due to the nonlinear dependence of the interaction force on the probe-sample position as well as the deformation/reaction of the sample [59, 60], and the relative probe-sample position is sensitive to the probe-sample interaction [60]. Therefore, there exists a need to achieve precision positioning of the AFM-probe in the vertical z-axis to achieve high-speed AFM imaging.

Currently, the low imaging speed has become one of the barriers in AFM imaging technology. For example, AFM enables the imaging of live biological samples under bio-friendly environment (i.e., the liquid environment for the live biological sample to maintain its physiological condition and/or biological function). However, the AFM imaging time of at least several minutes is too slow to capture rapid biological phenomena happening in seconds, such as the locomotion of living cells [16] and the dehydration process of collagen [61, 62]—because the first pixel and the last pixel in the obtained image are acquired at very different time instants.

As a result, large temporal errors occur in the obtained image. AFM is also used as a key metrology tool at nanoscale in the semiconductor industry, however, current AFM is too slow to meet the desired inspection throughput of over 100 wafers/hour (which is about 2 orders of magnitude higher than the throughput achievable on current AFM). Other areas where high-speed AFM is needed include in-situ characterization of the "interface" phenomena of thin films and polymer crystallization [63, 64, 65], high-throughput manufacturing of nanomaterials and nanodevices [56, 66, 67], and high-sensitivity, multiplex bioarrays [67, 68]. Thus, the development of high-speed AFM will generate a broad impact.

Control techniques are needed to achieve high-speed AFM imaging. We note that hardware improvements including the high-bandwidth piezoactuators [69, 70, 71], the small cantilever [72, 73], and the improved positioner structure [74] have led to the increase of AFM imaging speed. For example, by using high-bandwidth piezoactuator (over 200 KHz in [69], compared to $\sim$1 KHz bandwidth of the piezotube used on current AFMs), the scan rate of AFM imaging was increased $\sim$100 times [69] (from $\sim$10 Hz to 1.25 KHz). Such high-speed AFM imaging via hardware improvements, however, is very limited: the image size is only 2$\sim$10% of that of current AFM, and the sample can be imaged is also very flat (with sample asperities less than 30 nm [69, 71], which is also less than 1% of the sample asperities that can be imaged on current AFM). These limits arise because the displacement range of piezo actuators (without exciting the dynamics effect of the hardware) becomes much smaller as the bandwidth increases. Therefore, hardware improvement alone cannot achieve high-speed AFM imaging with no loss of imaging size (sample asperity) and spatial resolution. Control techniques need to be developed to fully exploit the hardware capability.

Various control approaches have been developed for the z-axis precision positioning of the probe during the AFM imaging. For example, PI-type of controllers have been widely used in commercial AFM systems. The performance of such *ad-hoc* controllers at high-speed, however, is poor [17] because of the low gain margin of the piezo actuators. Modern model-based feed-

back control approach increases the system bandwidth and achieves better robustness [17, 18]. However, the feedback-based approach is still limited by the fundamental trade-off of the bandwidth with the robustness of the control system. Moreover, for nonminimum-phase systems such as piezoelectric actuators on AFM [17, 20], the performance of feedback control is further limited [44]. These constraints of feedback approaches to the z-axis control of AFM imaging can be alleviated by combining the feedback control with the feedforward control in the two-degree-of-freedom (2DOF) control framework [43]. Limits, however, still exist in current 2DOF control design. Because the feedforward controller is causal, the constraints posed by the nonminimum-phase dynamics of piezo actuators cannot be overcomed, and the sample profile information from previous scan cannot be fully utilized; also, the "bandwidth" of the feedforward control is constrained. Therefore, there exists a need to better design the 2DOF control system for the z-axis positioning of AFM imaging.

The main contribution of this chapter is the development of a novel CCF-ILC approach to achieve z-axis precision positioning during the AFM imaging. In the CCF-ILC framework, the iterative control input is generated online by using the tracking results from the previous iteration (i.e., previous cycle), and is augmented to the feedback control input during the current iteration (i.e., current cycle, called "current-cycle-feedback" as in literature [10]). Particularly, we decouple the bandwidth requirement from the robustness requirement by designing the feedback controller mainly to enhance the robustness of the entire system, and the feedforward control to increase the bandwidth. The feedforward controller is designed to overcome the nonminimum-phase constraint of the piezo dynamics and to utilize the noncausality through iterations to improve the tracking. Specifically, the feedback controller is designed using the H_∞ robust control theory [45], and the robust-inverse [75] is introduced into the ILC filter design to explicitly account for the system dynamics uncertainty in the feedforward control. The proposed CCF-ILC control approach is illustrated by implementing it to the z-axis direction control in AFM imaging. Experimental results show that the imaging speed can be significantly increased by using the proposed approach.

4.2 Problem formulation and Analysis

In this section, we present the inversion-based CCF-ILC approach to the vertical z-axis positioning of the AFM probe during imaging. We start with a brief description of the z-axis feedback control for the AFM imaging.

The feedback control system for z-axis AFM probe positioning is shown in Fig. 4.1(a), where $G_z(s)$ denotes the dynamics model of the piezo actuator for the z-axis positioning, $G_c(s)$ denotes the cantilever-photodiode dynamics (from the output of the z-axis piezo to the cantilever deflection), $d_s(\cdot)$ denotes the sample profile, and $n_s(\cdot)$ denotes the system noise. The goal of the z-axis AFM probe positioning is to maintain a constant setpoint value (i.e., a constant normal force between the tip and the sample) during the scanning process. Then the image of the sample topography can be estimated using the control signal or the deflection error [76].

Unlike the above feedback-based approach to z-axis positioning, the proposed CCF-ILC approach integrates an online iterative-learning control (ILC) as feedforward to the z-axis feedback control. First, to simplify the presentation of the controller design, the unknown sample profile in the z-axis feedback control loop in Fig. 4.1 (a) is scaled with the DC-Gain of the cantilever-photodiode dynamics $G_c(0)$, and then right-shifted to the joint point at the cantilever deflection output (denoted using the same notation $d_s(\cdot)$ to simplify the notation), as shown in Fig. 4.1 (b) (Such a signal-shift is feasible because the bandwidth of the cantilever-photodiode dynamics tends to be much higher (over 10 times) than that of the z-axis piezo dynamics). Then, the proposed CCF-ILC controller is schematically shown in Fig. 4.1 (c), where $Q(j\omega)$ and $L(j\omega)$ are the ILC filters to be designed, `delay` $D(j\omega)$ denotes the one-scan-period delay, and $R(j\omega)$ denotes the observer to obtain the measured sample profile $d_e(j\omega)$. Specifically, the objectives of the proposed CCF-ILC design are to:

1. Guarantee the convergence of the CCF-ILC approach, i.e., the feedforward control input

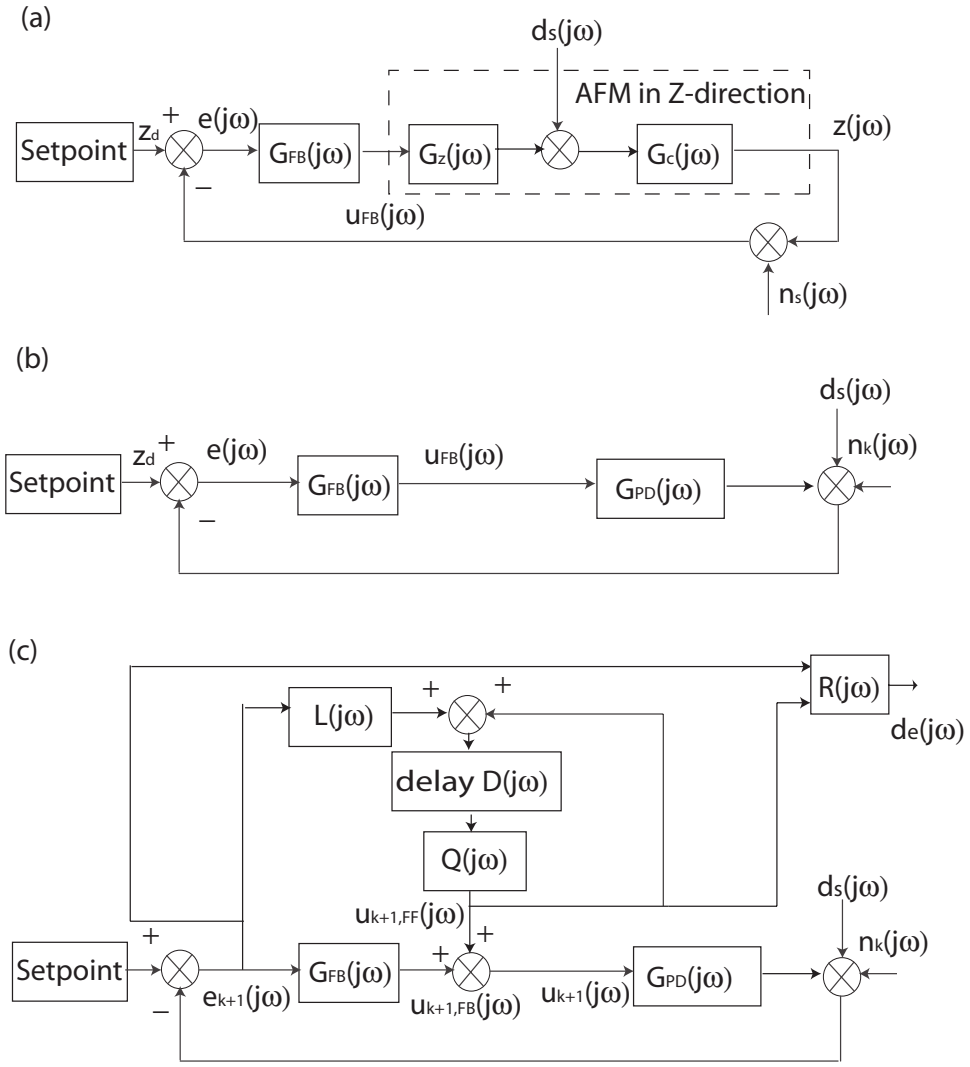

Figure 4.1 The block diagram of (a) a standard feedback loop, (b) the modified feedback loop, and (c) the proposed CCF-ILC approach for the z-axis positioning in AFM imaging.

$u_{k,FF}(j\omega)$ remains bounded for iterations $\forall k > 1$, and the the residual error $e_k(j\omega)$ converges to zero when the noise $n(j\omega)$ vanishes;

2. Improve the feedback tracking with the augmented feedforward control, i.e., for the same feedback controller, the tracking error $e(j\omega)$ (e.g., the deflection signal) is smaller when using the CCF-ILC approach than that when using the feedback control alone;

3. Improve the imaging accuracy, i.e., the estimation of the sample profile $d_s(j\omega)$ (denoted as $d_e(j\omega)$ in Fig. 4.1 (c)), is more accurate than the estimation obtained by current commercial AFMs.

We note that the proposed CCF-ILC approach aims at achieving high-speed imaging of samples with relatively smooth topography (i.e., the sample topography change from one scanline to the next is relatively small). In those samples, the sample profiles across two adjacent scanlines are similar, thus once a precision imaging on one scanline is obtained, then the line-to-line similarity can be explored to minimize the iterations needed for the next scanline imaging. Thus, the CCF-ILC approach will be able to significantly reduce the total imaging time. Samples of relatively smooth topography appear in a wide variety of areas, such as polished surfaces in semiconductor and optical industry [77], nano-/bio-materials [78], and various biological samples [79]. As the first step, this chapter is focused on the precision tracking of the sample profile on one scanline.

In the proposed CCF-ILC technique, a stabilizing feedback controller $G_{FB}(s)$ is designed first—the feedback controller $G_{FB}(s)$ guarantees that the feedback loop is internally stable [45]. Therefore, the first objective of the proposed controller design implies that all the signals in the control system (Fig. 4.1 (c)) should be bounded throughout the iterations. It is noted that the z-axis positioning of the AFM probe can be sensitive to effects such as the probe shape, the setpoint value of the loading force (i.e., the cantilever deflection), and the sensor/signal noise [80]. Therefore, the feedback controller is designed to enhance the robustness of the entire control system against these adverse effects.

4.2.1 Robust Feedback Controller Design

The feedback controller $G_{FB}(j\omega)$ is designed by using the model-based H_∞ robust feedback control technique [17, 43]. The goal of the H_∞ robust control design is to render the sensitivity of the feedback control system, $S(j\omega)$,

$$S(j\omega) = \frac{1}{1 + G_{PD}(j\omega)G_{FB}(j\omega)}, \tag{4.1}$$

and the complementary sensitivity of the feedback control system, $T(j\omega)$,

$$T(j\omega) = \frac{G_{PD}(j\omega)G_{FB}(j\omega)}{1 + G_{PD}(j\omega)G_{FB}(j\omega)}, \tag{4.2}$$

to satisfy given stability and robustness requirements [45]. This goal can be achieved by seeking the feedback controller $G_{FB}(jw)$ to satisfy the following criteria

$$\left\| \begin{array}{c} W_P(j\omega)S(j\omega) \\ W_T(j\omega)T(j\omega) \\ W_u(j\omega)G_{FB}(j\omega)S(j\omega) \end{array} \right\|_\infty \leq 1 \tag{4.3}$$

where $\|G(j\omega)\|_\infty$ denotes the H_∞ norm of the transfer function $G(j\omega)$ [45], $G_{FB}(j\omega)$ denotes the feedback controller, and $W_P(j\omega)$, $W_T(j\omega)$, $W_u(j\omega)$ are user-defined weighting functions to impose the requirements for the bandwidth and tracking performance ($W_P(j\omega)$), the robustness against model uncertainties ($W_T(j\omega)$), and the input magnitude ($W_u(j\omega)$), respectively [81].

4.2.2 CCF-ILC Design: Convergence Analysis

In the proposed CCF-ILC approach, the following general form of linear iterative learning control law is employed [10]:

$$\begin{aligned} u_{0,FF}(j\omega) &= 0 \\ u_{k+1,FF}(j\omega) &= Q(j\omega)(u_{k,FF}(j\omega) + L(j\omega)e_k(j\omega)), \qquad \text{for } k \geq 1 \end{aligned} \tag{4.4}$$

where $Q(j\omega)$ and $L(j\omega)$ are the ILC filters as shown in Fig. 4.1 (c). Note that in Eq. (4.4), the filter $Q(j\omega)$ is factored out without loss of generality. The conditions to guarantee the convergence of the CCF-ILC algorithm (the first objective) is given by the following lemma.

Lemma 5 *Let $G_{PD}(j\omega)$ be the frequency response of a linear time invariant plant, and let $G_{FB}(j\omega)$ be a stabilizing feedback controller. Then for bounded measurement noise $n_k(j\omega)$, i.e., $|n_k(j\omega)| \leq \delta(\omega)$, both the iterative control input $u_k(j\omega)$ and the residual error $e_k(j\omega)$ are bounded throughout the iterations; And the limit of the residue error $e_k(j\omega)$ (as the iteration $k \to \infty$) is bounded by an affine function of the sample profile $d_s(j\omega)$ and the noise effect $\delta(\omega)$*

$$|e_\infty(j\omega)| \triangleq \lim_{k\to\infty} |e_k(j\omega)| \leq \Big|\frac{\mathbf{E}_d(\omega)}{1-\rho(\omega)}\Big|\,|d_s(j\omega)| + \mathbf{E}_\delta(\omega)\delta(\omega), \tag{4.5}$$

provided that the ILC filters $L(j\omega)$ and $Q(j\omega)$ are chosen such that the following iteration coefficient $\rho(j\omega)$ is less than one,

$$\rho(\omega) = |Q(j\omega)\{1 - G_{PD}(j\omega)S(j\omega)L(j\omega)\}| < 1. \tag{4.6}$$

In Eq. (4.5), the limit of the residual error $e_\infty(j\omega)$ is called the ultimate ILC error*, and the frequency dependent coefficient $\mathbf{E}_d(\omega)$ and $\mathbf{E}_\delta(j\omega)$ are defined as*

$$\mathbf{E}_d(\omega) \triangleq |(Q(j\omega)-1)S(j\omega)| \tag{4.7}$$

$$\mathbf{E}_\delta(\omega) \triangleq \frac{|Q(j\omega)G_{PD}(j\omega)S(j\omega)L(j\omega)S(j\omega)| + |S(j\omega)|}{|1-\rho(\omega)|} \tag{4.8}$$

Proof We proceed by quantifying the residual error $e_k(j\omega)$ for given noise/disturbance $n_k(j\omega)$ at the k^{th} iteration. First note that by Fig. 4.1 (c), the feedforward control input $u_{k,FF}(j\omega)$ can be written as

$$u_{k,FF}(j\omega) = S^{-1}(j\omega)G_{PD}^{-1}(j\omega)\left[-e_k(j\omega) - S(j\omega)d(j\omega) - S(j\omega)n_k(j\omega)\right] \tag{4.9}$$

In the following derivation, the dependence on $j\omega$ is omitted for simplicity. Substituting Eq. (4.9) into Eq. (4.4) leads to

$$G_{PD}^{-1}\left[-e_{k+1} - Sd - Sn_{k+1}\right] = QG_{PD}^{-1}\left[-e_k - Sd_s - Sn_k\right] \quad + SQLe_k \tag{4.10}$$

Rewriting Eq. (4.10) yields

$$\begin{aligned}
e_{k+1} &= Q\left(1-G_{PD}SL\right)e_k + (Q-1)Sd_s + QSn_k - Sn_{k+1} \\
&= Q\left(1-G_{PD}SL\right)\left\{Q\left(1-G_{PD}SL\right)e_{k-1} + (Q-1)Sd_s\right\} \\
&\quad +QSn_{k-1} - Sn_k + (Q-1)Sd_s + QSn_k - Sn_{k+1} \\
&= \cdots \\
&= \left\{Q\left(1-G_{PD}SL\right)\right\}^{k+1} e_0 \quad + \sum_{j=0}^{k}\left\{Q\left(1-G_{PD}SL\right)\right\}^{j}(Q-1)Sd_s \\
&\quad + \sum_{j=0}^{k}\left\{Q\left(1-G_{PD}SL\right)\right\}^{j} QSn_{k-j} \quad - \sum_{j=0}^{k}\left\{Q\left(1-G_{PD}SL\right)\right\}^{j} Sn_{k+1-j} \qquad (4.11)
\end{aligned}$$

By changing the index used in the last term in Eq. (4.11), the last two terms in Eq. (4.11) can be simplified as:

$$\begin{aligned}
&\sum_{j=0}^{k}\left\{Q\left(1-G_{PD}SL\right)\right\}^{j} QSn_{k-j} - \sum_{j=0}^{k}\left\{Q\left(1-G_{PD}SL\right)\right\}^{j} Sn_{k+1-j} \\
= &\sum_{j=0}^{k}\left\{Q\left(1-G_{PD}SL\right)\right\}^{j} QSn_{k-j} - \sum_{j=0}^{k}\left\{Q\left(1-G_{PD}SL\right)\right\}^{j+1} Sn_{k-j} \\
&-sn_{k+1} + \left\{Q\left(1-G_{PD}SL\right)\right\}^{k+1} sn_0 \\
= &\sum_{j=0}^{k}\left\{Q\left(1-G_{PD}SL\right)\right\}^{j}\left\{Q - Q(1-GSL)\right\} Sn_{k-j} - sn_{k+1} + \left\{Q\left(1-G_{PD}SL\right)\right\}^{k+1} sn_0 \\
= &\left\{\sum_{j=0}^{k}\left\{Q\left(1-G_{PD}SL\right)\right\}^{j} QG_{PD}SLSn_{k-j}\right\} - sn_{k+1} + \left\{Q\left(1-G_{PD}SL\right)\right\}^{k+1} sn_0 \qquad (4.12)
\end{aligned}$$

Substituting Eq. (4.12) into Eq. (4.11) and using triangle inequality, the iterative residual error e_{k+1} can be bounded as

$$\begin{aligned}
|e_{k+1}| &\leq \rho^{k+1}|e_0| + \mathbf{E}_d|d_s|\sum_{j=0}^{k}\rho^j + (1+\rho^{k+1})|S\delta| + |QG_{PD}SLS|\,|\delta|\sum_{j=0}^{k}\rho^j \\
&\quad \text{(By definitions of } \mathbf{E}_d \text{ and } \rho \text{ in Eqs. (4.6, 4.7))} \\
&\leq \rho^k|e_0| + \frac{\mathbf{E}_d|d_s|\left(1-\rho^k\right)}{1-\rho} + \frac{|QG_{PD}SLS|\,|\delta|\left(1-\rho^k\right)}{1-\rho} + (1+\rho^{k+1})|S|\,|\delta|\,. \qquad (4.13)
\end{aligned}$$

Thus, from the above Eq. (4.13) the tracking error e_k is bounded for all iterations $k \geq 1$, and is eventually bounded by the ultimate error, $|e_\infty|$, as defined in Eq. (4.5), when the iteration coefficient $\rho(\omega) < 1$ and the iteration $k \to \infty$. Similarly, it can be shown that under the same condition (i.e., $|\rho(\omega)| < 1$), the iterative control input in the k^{th} iteration, $u_k(j\omega)$, is also bounded. This completes the proof. ■

Remark 13 *The above Lemma 5 shows that implementation of the CCF-ILC approach is not restricted to AFM imaging — it can be used for tracking/rejecting unknown periodic trajectory or disturbance in other applications.*

Equation (4.5) of the ultimate error $e_\infty(j\omega)$ shows that when the measurement noise is negligible (i.e., $\delta(\omega) = 0$), the ultimate error approaches to zero (the objective one), i.e., $e_\infty = 0$, when 1) the ultimate error coefficient equals to zero (i.e., $\mathbf{E}_d(\omega) = 0$), and 2) the iteration coefficient is less than one (i.e., $\rho(\omega) < 1$). It will be shown next that these two conditions can be satisfied in the proposed inversion-based CCF-ILC approach through the design of the ILC filters $Q(j\omega)$ and $L(j\omega)$.

4.3 Design of the CCF-ILC Filters

Lemma 5 implies that to achieve good tracking, the filter $Q(j\omega)$ should be chosen to be one (to make $\mathbf{E}_d(\omega) = 0$), and the filter $L(j\omega)$ should approximate the inverse of the closed-loop transfer function $G_{PD}(j\omega)S(j\omega)$ (to render a small iteration coefficient $\rho(\omega)$). This observation agrees with, in general, the design strategy of CCF-ILC controller as described in Ref. [10]. However, exact inverse of the closed-loop transfer function $G_{PD}(j\omega)S(j\omega)$ is limited by model uncertainties [8] and noise effect, particularly in the high frequency range. As shown in Eq. (4.6), these adverse effects can result in a large iteration coefficient $\rho(\omega)$ (i.e., the second term in Eq. (4.6) becomes large), and the filter $Q(j\omega)$ should be designed, in general, to possess low-pass characteristics. Thus in the following, $Q(j\omega)$ is named as the "roll-off ILC filter" and $L(j\omega)$ as the "inversion-based ILC filter".

We propose a two-step approach to design the ILC filters $Q(j\omega)$ and $L(j\omega)$. Since the ultimate error coefficient $\mathbf{E}_d(\omega)$ (as defined in (4.7)) is independent to the design of the inversion-based ILC filter $L(j\omega)$, we first, design the inversion-based ILC filter $L(j\omega)$ to minimize the term $|1 - G_{PD}(j\omega)S(j\omega)L(j\omega)|$ in the iteration coefficient $\rho(\omega)$. Then secondly, the roll-off ILC filter $Q(j\omega)$ is designed to ensure the convergence of the CCF-ILC algorithm, and to minimize the ultimate error $e_\infty(j\omega)$ (see Eq. (4.5)).

4.3.1 Design of the inversion-based ILC filter $L(j\omega)$

The filter $L(j\omega)$ is designed by using the recently-developed robust-inversion technique [75] to minimize the term $|1 - G_{PD}(j\omega)S(j\omega)L(j\omega)|$ upon system dynamics uncertainties, i.e.,

$$\min_{L(j\omega)} \sup_{\Delta G} \left|1 - G_{PD}(j\omega)S(j\omega)L(j\omega)\right|, \tag{4.14}$$

where $\Delta G(j\omega)$ denotes the model uncertainties as defined below [75, 1],

$$\Delta G(j\omega) = \frac{G_L(j\omega)}{G_{L,m}(j\omega)} = \Delta r(\omega) \cdot e^{j\Delta\theta(\omega)}. \tag{4.15}$$

In Eq. (4.15), $G_L(j\omega)$ denotes the true linear dynamics response of the system, e.g., for the z-axis AFM dynamics,

$$G_L(j\omega) = G_{PD}(j\omega)S(j\omega), \tag{4.16}$$

and $G_{L,m}(j\omega)$ denotes the model of the linear dynamics $G_L(j\omega)$. In the robust-inversion technique, a frequency-dependent gain-modulation $\alpha(\omega)$ is introduced in the inversion-based ILC filter,

$$L(j\omega) = \alpha(\omega) \cdot G_{L,m}^{-1}(j\omega), \tag{4.17}$$

and then the design objective is transformed to finding the optimal gain modulation $\alpha(\omega)$ against the model uncertainty, i.e. ,

$$\min_{\alpha(\omega)} \sup_{\Delta G} \left|1 - \alpha(\omega)\Delta G(j\omega)\right| \tag{4.18}$$

The solution to the above minmax problem (4.18) is given in the following Theorem [75].

Theorem 2 *At any given frequency ω, let the magnitude variation of the system dynamics $\Delta r(\omega)$ (defined in (4.15)) be bounded as $\Delta r(\omega) \in [\Delta r_{\min}(\omega),\ \Delta r_{\max}(\omega)]$, with $\Delta r_{\min} \in (0,\ 1]$ and $\Delta r_{\max}(\omega) \geq 1$, then if the size of the phase variation of the system dynamics, $\Delta\theta_m(\omega)$, is less than $\pi/2$, i.e., $\left|\Delta\theta_m(\omega)\right| < \pi/2$:*

1. *The feedforward control error term $|1 - \alpha\Delta G(j\omega)|$ is less than 1 if and only if the gain coefficient $\alpha(\omega)$ is chosen as*

$$0 < \alpha(\omega) < \frac{2\cos(\Delta\theta_m(\omega))}{\Delta r_{\max}(\omega)};$$

2. The optimal gain $\alpha(\omega)$ to solve the minmax problem (4.18) is given by

$$\alpha_{opt}(\omega) = \frac{2\cos\left(\Delta\theta_m(\omega)\right)}{\Delta r_{\min}(\omega) + \Delta r_{\max}(\omega)}. \tag{4.19}$$

3. The solution to the minmax problem (4.18) (with the optimal gain (4.19)) is,

$$\min_{\alpha(\omega)} \sup_{\Delta G} \left|1 - \alpha(\omega)\Delta G(j\omega)\right| = \sqrt{1 - \frac{4\cos^2\left(\Delta\theta_m(\omega)\right)\Delta r_{\min}(\omega)\Delta r_{\max}(\omega)}{\left(\Delta r_{\min}(\omega) + \Delta r_{\max}(\omega)\right)^2}}. \tag{4.20}$$

Corollary 2 *The inversion-based ILC filter $L(j\omega)$ has no poles on the $j\omega$ axis, provided that the original system $G_{L,m}(j\omega)$ is hyperbolic (i.e., has no poles/zeros on the $j\omega$ axis).*

Proof We show by contradiction. Assume that the ILC filter $L(j\omega)$ has a pair of poles on the $j\omega$ axis, $\pm ja$ (with $a \in \Re$), then the frequency response of the ILC filter $L(j\omega)$ approaches to infinity as the frequency ω appoaches to a, i.e., $L(j\omega) \to \infty$ as $w \to a$. However, the hyperbolicity of the original system implies that its inverse $G_{L,m}^{-1}(j\omega)$ is also hyperbolic, and the gain modulation term $\alpha(\omega)$ is less than 1 (by (4.19)) and thereby bounded for all frequency ω. Therefore, the ILC filter $L(j\omega)$ is also bounded at all frequencies ω—a contradiction! This completes the proof. ■

Remark 14 *Theorem 2 implies that when the phase variation of the system dynamics is larger than or equal to $\pi/2$ at frequency ω, the optimal gain $\alpha(\omega)$ should be set to zero, i.e., $L(j\omega) = 0$, and the solution to the minmax problem (Eq. (4.14)) equals to one at that frequency ω. It is noted that the dynamics uncertainty $\Delta G(j\omega)$ can be experimentally estimated in applications, for example, by 1) measuring the system frequency response under various operation conditions, and 2) obtaining the maximum dynamics differences (in both magnitude and phase) among the measured frequency responses [75]. This procedure is illustrated in Sec.4.4.3.*

Remark 15 *The above robust-inversion-based ILC filter design is fundamentally different from the existing CCF-ILC approaches, where the ILC filter $L(j\omega)$ is designed using the H_∞ robust-control approach [10] and a causal stable filter $L(j\omega)$ is obtained. On the contrary, the*

above robust-inversion-based ILC filter $L(j\omega)$ is not restricted to a causal filter. Therefore, for nonminimum-phase systems, the tracking performance of the robust-inversion based filter will not be limited by the nonminimum-phase characteristics of the system [44], and the system dynamics is better compensated for by using the proposed CCF-ILC method (than the existing CCF-ILC approaches). Moreover, the proposed ILC filter design explicitly accounts for and minimizes the effect of model uncertainties.

4.3.2 Realization of the inversion-based ILC filter $L(j\omega)$

It is noted that the inversion-based filter $L(j\omega)$ might have right-half-plane poles, thereby become unstable. Thus its online implementation, as needed in the proposed CCF-ILC algorithm, can be challenging. We propose two implementation schemes: 1). the preview-based stable inversion technique [20, 48]; and 2) the frequency-domain method using the Fourier-transform method (e.g., FFT).

The preview-based stable-inversion approach obtains the bounded solution to the robust-inversion-based filter $L(j\omega)$ by using the notion of noncausality, provided that 1). the filter $L(j\omega)$ has no pure imaginary poles, and 2) the input signal to the filter $L(j\omega)$ can be previewed for some finite amount of time, (i.e., preview time). These two conditions are satisfied in the proposed CCF-ILC approach—by Corollary 2 and that the input signal to the filter $L(j\omega)$, the error $e(j\omega)$ from previous scanline (see (4.4)), is known a priori for one entire scanline, i.e., the error $e(j\omega)$ can be previewed with preview time of one scan period. It has been shown that the precise output of the filter $L(j\omega)$ can be obtained with a large enough preview time (the required preview time depends on the unstable dynamics part of the filter $L(j\omega)$, and thus can be quantified [20, 48]). Readers are referred to [20, 48] for the details. Alternatively, the filter $L(j\omega)$ can be directly implemented in frequency-domain using fast Fourier transform (FFT). This method is illustrated in Sec. 4.4.3.

4.3.3 Design of the roll-off ILC filter $Q(j\omega)$

Next, the roll-off ILC filter $Q(j\omega)$ is designed to compensate for the dynamics uncertainties and noise effect. By (4.6), to garantee the convergence of the CCF-ILC approach, the roll-off filter $Q(j\omega)$ must be chosen to render the iteration coefficient $\rho(j\omega)$ less than one. Such a requirement leads to the following upper bound of the roll-off filter $Q(j\omega)$:

$$|Q(j\omega)| < \frac{1}{|(1 - L(j\omega)G_{PD}(j\omega)S(j\omega))|}. \tag{4.21}$$

To reduce the ultimate error $|e_\infty|$ (see (4.5)), the roll-off filter $Q(j\omega)$ should be close to one whenever it is possible. Since in practices, precision tracking in low frequency range is usually needed, the roll-off filter $Q(j\omega) = 1$ should be chosen in the low frequency range. Generally, such a choice of filter $Q(j\omega)$ can be realized in the proposed CCF-ILC framework, because the model uncertainty tends to be small in the low frequency range (specifically, the phase variation tends to be $< \pi/2$), and thus the upper bound of the roll-off filter $Q(j\omega)$ (4.21) is larger than 1 (see (4.13)). In the high frequency range, however, model uncertainty tends to be significant and the phase variation can be larger than $\pi/2$, for example, around the resonant frequencies and/or lightly-damped zeros. Thus by Theorem 2, the inversion-based filter $L(j\omega) = 0$ should be chosen (see Remark 14), and the gain of the roll-off filter $Q(j\omega)$ becomes less than 1 (by (4.21)). Moreover, the noise and the disturbance effects also tend to be large—compared to the system gain in the high frequency range. Therefore, the filter $Q(j\omega)$ should be rolled-off as frequency increased. Thus, the roll-off filter $Q(j\omega)$ should have "low-pass" characteristics, and Eq. (4.21) provides a guide to the design of such a low-pass filter.

The phase delay, associated with conventional low-pass filters, however, must be accounted for when implementing the roll-off filter $Q(j\omega)$. Such a phase delay can result in the residual error $e_k(j\omega)$ to be amplified rather than reduced when the iterative feedforward control input is applied. To remove this detrimental phase delay, a zero-phase low-pass filter is used to implement the roll-off filter $Q(j\omega)$. Particularly, we present a discrete-time domain representation of the zero-phase low-pass filter to facilitate its implementation [82]: A 2N order zero-phase

FIR (finite impulse response) real filter is given by

$$Q(z) = b_0 + \sum_{k=1}^{N}(b_k z^k) + \sum_{k=1}^{N}(b_k z^{-k}) \tag{4.22}$$

where the coefficients $b_k \in \Re$. It can be shown that the frequency response of $Q(e^{j\omega T})$ is real—thus the phase of $Q(z)$ is zero, i.e.,

$$Q(e^{j\omega T}) = b_0 + \sum_{k=1}^{N}(2b_k \cos \omega NT) \in \Re. \tag{4.23}$$

It is evident from (4.22) that the zero-phase FIR filter is noncausual. Such a noncausal filter, however, is implementable in the proposed CCF-ILC framework because the signal to be filtered is the sample profile from the previous scanline, thereby completely known ahead—as long as the filter order N is not larger than the total sampling points on one scanline. For example, even under a low-resolution imaging with 64 pixel per scanline, a 128 order zero-phase low-pass filter can still be implemented.

4.3.4 Positioning Enhancement with CCF-ILC Approach

The inversion-based CCF-ILC will enhance the total tracking performance (the second design objective) provided that the measurement noise/disturbance ($n_k(j\omega)$ in Fig. 4.1) is small. Next, we discuss that the ultimate error of the CCF-ILC approach, $|e_\infty(j\omega)|$, is less than or equal to the feedback residual error, $|e_{FB}(j\omega)| = |S(j\omega)d_s(j\omega)|$, when the noise is negligible. By (4.5), when the noise is ignored ($\delta(\omega) = 0$), the ratio $q(\omega)$ of the CCF-ILC tracking error, $e_\infty(j\omega)$, with respect to the tracking error of feedback only, $e_{FB}(j\omega)$, becomes

$$q(\omega) \;=\; \frac{|e_\infty(j\omega)|}{|e_{FB}(j\omega)|} = \frac{|1 - Q(j\omega)|}{\Big|1 - |Q(j\omega)|\,|1 - G_L(j\omega)L(j\omega)|\Big|}. \tag{4.24}$$

Then we proceed our discussion by considering the tracking with or without applying the CCF-ILC feedforward input,

1. In the frequency range where the dynamics variation is small, the CCF-ILC controller $L(j\omega)$ is applied (see Remark 14), and the term $|1 - G_L L|$ in the error ratio (4.24) is less than 1 (by (4.13)). Thus, the error ratio is less than one, $q(\omega) < 1$, because the ILC filter $Q(j\omega)$ is a zero phase low-pass filter and $Q(j\omega) \leq 1$ in that frequency range;

2. In the frequency range where the dynamics variation is large, the CCF-ILC controller $L(j\omega)$ is set to zero (see Remark 14), the term $|1 - G_L L| = 1$, and thereby the error ratio equals to one, $q(\omega) = 1$.

Thus by the continuity of the system dynamics, the above discussion implies that when the noise/disturbance is small, the use of the proposed CCF-ILC approach will enhance the total tracking performance.

4.3.5 Design of the sample topography observer $R(j\omega)$

Finally, we present a model-based observer of sample topography $R(j\omega)$. In commercial AFMs, sample profile is estimated simply by scaling the input to the z-axis piezo actuator by its DC-Gain. Using such a method, good estimation can be obtained only when the scanning rate is low, i.e., when the piezo actuator dynamics can be adequately approximated by its DC-gain. As the scanning rate increases, the effects of the AFM z-axis dynamics (including the piezoactuator, the cantilever, and the mechanical fixture connecting these two parts) also become significant, i.e., the piezo input-output relation should be accounted for not by the DC-gain, but by the full dynamics model instead. The effect of the z-axis AFM dynamics also implies that during high speed imaging, even if the cantilever deflection is maintained around the setpoint value, the motion of the piezo actuator may not resemble the sample profile at all. Furthermore, during high-speed imaging, the dynamics coupling from the lateral scanning of the piezotube scanner to its vertical motion also becomes significant, resulting in large coupling-caused vertical motion [1, 83]. Such coupling-caused vertical displacement must be accounted in the sample estimation. Therefore, new sample estimation method must be developed for high-speed AFM imaging.

We estimate the sample profile by using the z-axis dynamics model. Note that the x-to-z dynamics-coupling effect can be regarded as an additional disturbance to the cantilever deflection, thus it can be accounted-for by replacing the sample topography $d_s(j\omega)$ in Fig. 4.1

(c) with

$$\hat{d}(j\omega) = d_s(j\omega) + d_c(j\omega) \tag{4.25}$$

where $d_c(j\omega)$ denotes the coupling caused disturbance. Therefore, from the block diagram in Fig. 4.1 (c), the topography-coupling combined singal $\hat{d}(\omega)$ can be represented as

$$\begin{aligned}
\hat{d}(j\omega) &= -S^{-1}(j\omega)e_k(j\omega) - G_{PD}^{-1}(j\omega)u_{k,FF}(j\omega) \\
&= \begin{bmatrix} -S^{-1}(j\omega) & -G_{PD}^{-1}(j\omega) \end{bmatrix} \begin{bmatrix} e_k(j\omega) \\ u_{k,FF}(j\omega) \end{bmatrix} \\
&= R(j\omega) \begin{bmatrix} e_k(j\omega) \\ u_{k,FF}(j\omega) \end{bmatrix}
\end{aligned} \tag{4.26}$$

The above two Eqs. (4.25, 4.26) implies that the sample topography $d_s(j\omega)$ can be estimated as

$$d_s(j\omega) = R(j\omega) \begin{bmatrix} e_k(j\omega) \\ u_{k,FF}(j\omega) \end{bmatrix} - d_c(j\omega). \tag{4.27}$$

Note that the dynamics-coupling caused vertical displacement is *repetitive* at a period of the lateral scanning rate, therefore, such coupling-caused vertical motion can be compensated for by using iterative control approach. This idea has been explored in [1]. However, unlike the approach in [1], where additional feedforward control input needs to be applied to the z-axis control, the proposed CCF-ILC approach can accounts for the coupling-caused disturbance with no extra input. Also note that the cantilever deflection error, $e_k(j\omega)$, is utilized in the above sample topography estimation method, which implies that a good sample estimation can be obtained even when the z-axis positioning error is relatively large. Precision positioning in the z-axis, however, is still needed in many AFM imaging applications, because large variations of the cantilever deflection result in large variations in the tip-sample interaction force, which can damage the sample (when the sample is soft), or the tip (when the sample is stiff). Moreover, the proposed sample topography observer $R(j\omega)$ is implemented offline in frequency-domain in this chapter, thereby issues related to possibly nonminimum-phase and non-proper dynamics of the observer $R(j\omega)$ are avoided. However, the online implementation

can also be realized by using the preview-based stable-inversion technique [20].

Remark 16 *Recently, a sample estimation based on robust control approach has been proposed with online implementation [76]. However, the dynamics-coupling effect was not considered in [76], thereby significant imaging distortion can still occur when the dynamics-coupling caused disturbance motion becomes pronounced.*

4.4 Experiment Example: AFM Imaging

We illustrate the proposed CCF-ILC approach by implementing it on an AFM system ($Dimension^{TM}$ 3100, Veeco Inc). We start with describing the modeling of the z-axis AFM dynamics.

4.4.1 Model identification

First, the frequency response of the z-axis AFM dynamics, $G_{PD}(j\omega)$, was measured by using a data acquisition system along with MATLAB toolboxes. The AFM probe with a nominal spring constant of $0.12N/m$ was positioned to contact a silicon calibration sample with a normal load of $\sim$9 nN. Then a band-limited white noise signal $u(t)$ generated in MATLAB was applied to drive the piezo actuator, and the cantilever deflection signal $z(t)$ was measured and utilized to obtain the frequency response using the System Identification Toolbox. To estimate the model uncertainty, the frequency responses $G_{PD}(j\omega)$ were measured with five different input voltage levels (0.6 V, 0.7 V, 0.8 V, 0.9 V, 1 V) at three different normal loads (all around 9 nN). The total of 15 frequency responses measured were averaged to obtain the nominal frequency response $G_{PD,m}(j\omega)$, as shown in Fig. 4.2, which was used in the CCF-ILC design.

4.4.2 Robust feedback controller design

The transfer function model of the z-axis AFM dynamics can be obtained by curve-fitting the nominal frequency response (MATLAB command "invfreqs"). The frequency response of the obtained model was compared with the nominal experimental responses in Fig. 4.2. As shown

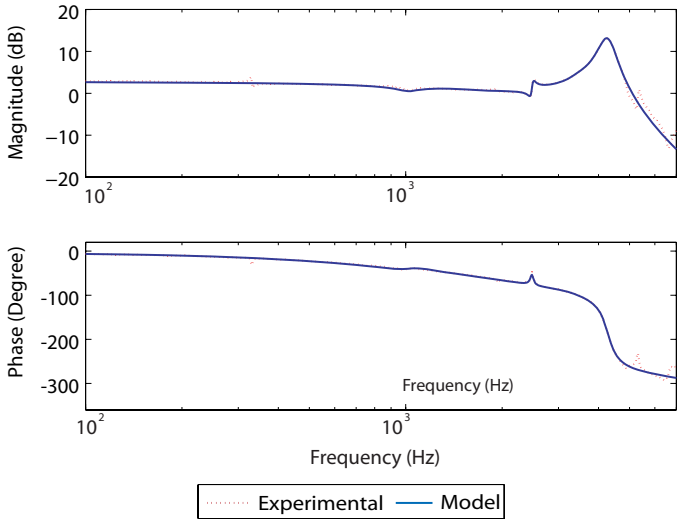

Figure 4.2 Comparison of the experimentally-measured nominal frequency response with the frequency response of the transfer function model for the AFM $z-$axis direction.

in Fig. 4.2, the transfer function model captured the z-axis AFM dynamics quite well until $\sim$ 4000 Hz. Then the feedback controller was designed mainly to enhance the robustness of the position system (rather than obtain a large bandwidth) as in [84]. For comparison, we also designed a proportional-integral (PI) feedback controller whose parameters were tuned during the experiments to experimentally optimize the tracking performance of the PI controller.

4.4.3 Design of the CCF-ILC filters $L(j\omega)$ and $Q(j\omega)$

Design of the robust-inversion-based ILC filter $L(j\omega)$ As shown in Sec. 4.3 (see Eqs. (4.15, 4.16, 4.17)), the closed-loop frequency response $G_{L,m}(j\omega)$ and its dynamics uncertainty $\Delta G(j\omega)$ need to be obtained in order to design the filter $L(j\omega)$. By applying the feedback controller $G_{FB}(s)$ to the nominal z-axis AFM dynamics (Subsec. 4.4.1), the closed-loop frequency response (needed in the design of filter $L(j\omega)$), $G_{L,m}(j\omega)$, was obtained. Then to estimate the related dynamics uncertainty, the measured open-loop frequency responses (total of 15) of the z-axis AFM dynamics (see Sec. 4.4.1) were used. The upper bound of the amplitude uncertainty and the phase uncertainty were estimated by finding the maximum difference among the

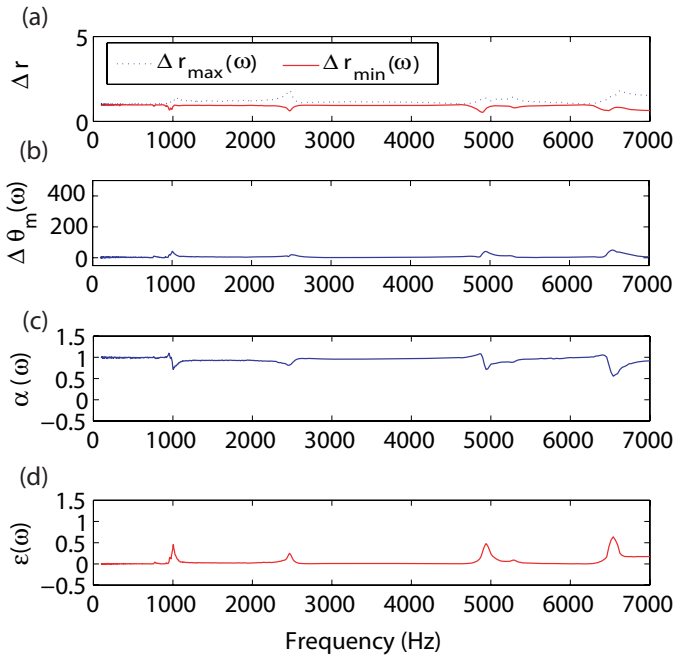

Figure 4.3 (a) the experimentally measured magnitude variation $\Delta r_{max}(\omega)$ and $\Delta r_{min}(\omega)$ (a), (b) the phase variation $\Delta\theta_m(\omega)$, (c) the calculated optimal gain $\alpha_{opt}(\omega)$, and (d) the minimized solution $\epsilon_L(\omega)$.

experimental frequency responses at each frequency $\omega \in [0,\ 7]\ kHz$, as shown in Fig. 4.3(a), (b), respectively. Then the optimal gain coefficient, $\alpha_{opt}(\omega)$, and the ILC filter $L(j\omega)$, were obtained according to Theorem 2(Eq. (4.20)). The results are plotted in Fig. 4.3 (c) ($\alpha_{opt}(\omega)$) and (d) ($\epsilon_L(\omega)$). Moreover, it was experimentally measured that the system noise has components mainly in the frequency range $\omega \geq 2000\ Hz$. Hence, to account for the noise effect, the optimal gain coefficient, $\alpha_{opt}(\omega)$ was truncated at frequency $\omega = 2\ KHz$, i.e.,

$$\alpha_{opt,m}(\omega) = \begin{cases} \alpha_{opt}(\omega) & \omega \leq 2000 \text{ Hz}, \\ 0 & \text{otherwise.} \end{cases} \tag{4.28}$$

Finally, the ILC inversion-based filter $L(j\omega)$ was obtained as $L(j\omega) = \alpha_{opt}(\omega)G^{-1}_{L,m}(j\omega)$. In the experiments, the filter $L(j\omega)$ was implemented in frequency-domain using MATLAB and SIMULINK toolbox (the blocks"fft" and "ifft" in SIMULINK). Particularly, MATLAB/SIMULINK requires one cycle (one scanline for AFM imaging) time to do the FFT/IFFT calculation, therefore one flat scanline was inserted between each scanlines to allow the batch calculation.

Design of the roll-off ILC filter $Q(j\omega)$ The design of the ILC roll-off filter $Q(j\omega)$ as a zero-phase, low-pass filter was realized by combining a linear phase FIR low-pass filter with a linear phase lead,

$$Q(z) = Q_l(z) \times z^P \tag{4.29}$$

where $Q_l(z)$ is the linear-phase FIR low-pass filter (Matlab command "firpm"). Note that the phase lead term z^P in Eq. (4.29) is simply a P-step forward shift in discrete-time implementation. Also the signal $L(j\omega)e_k(jw)$ and the feedforward control signal $u_{k,FF}(j\omega)$ from the previous scanline were delayed by one scanning period and applied in the CCF-ILC algorithm, i.e., the residual error signal was delayed by N-step (N: number of sampling points per scanline) in implementations. Therefore, the P-step phase lead can be combined with the N-step delay in implementations (denoted as the delay term"$D(j\omega)$" in Fig. 4.1(c)).

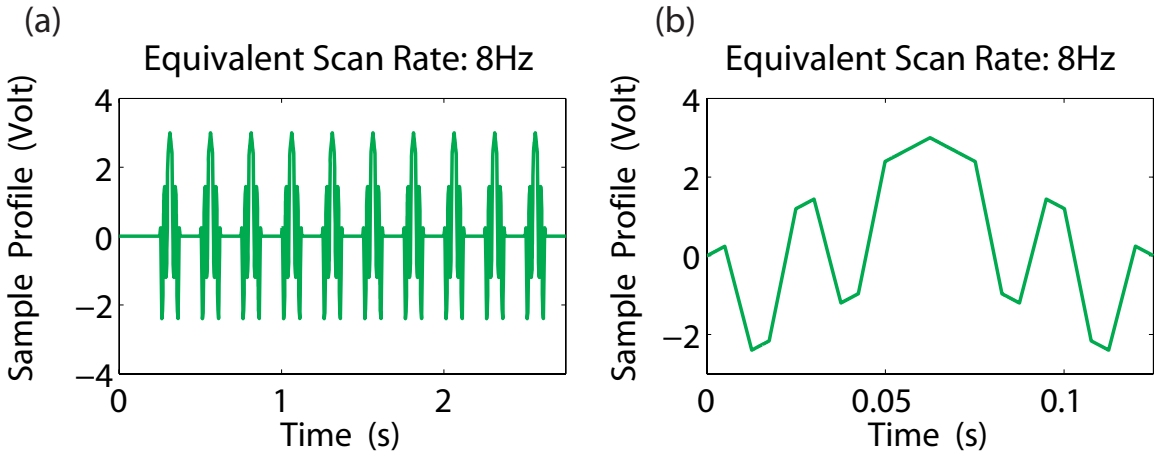

Figure 4.4 (a) the applied disturbance signal (for ten repetitive scans) with equivalent scan rate of 8 Hz; and (b) the zoomed-in view of the disturbance signal in one scan period (the disturbance trajectory for scan rate of 64 Hz is the same except it is 8 times faster).

4.4.4 Experimental results and discussion

The experimental implementation was conducted in two stages. First, Note that the unknown sample topography enters the z-axis positioning control system as a disturbance (see Fig. 4.1), thus as similarly done before [76], the performance of the z-axis control system can be separately evaluated by injecting a disturbance signal to the z-axis piezo actuator with no lateral x-y axes scanning. The disturbance signal would mimic a given sample topography. Therefore, this experiment is called the "one-point imaging", which excludes, in the vertical z-axis positioning control, the effects due to the lateral-to-vertical coupling [1, 83] and tracking errors from lateral scanning [54, 17]. Then secondly, the proposed method was used to repeatedly image a calibration sample on one scanline.

One point imaging

The disturbance trajectory was generated by mapping a simulation-generated sample profile (with sample slope as usually existing in real samples) to the lateral scanning period. Two

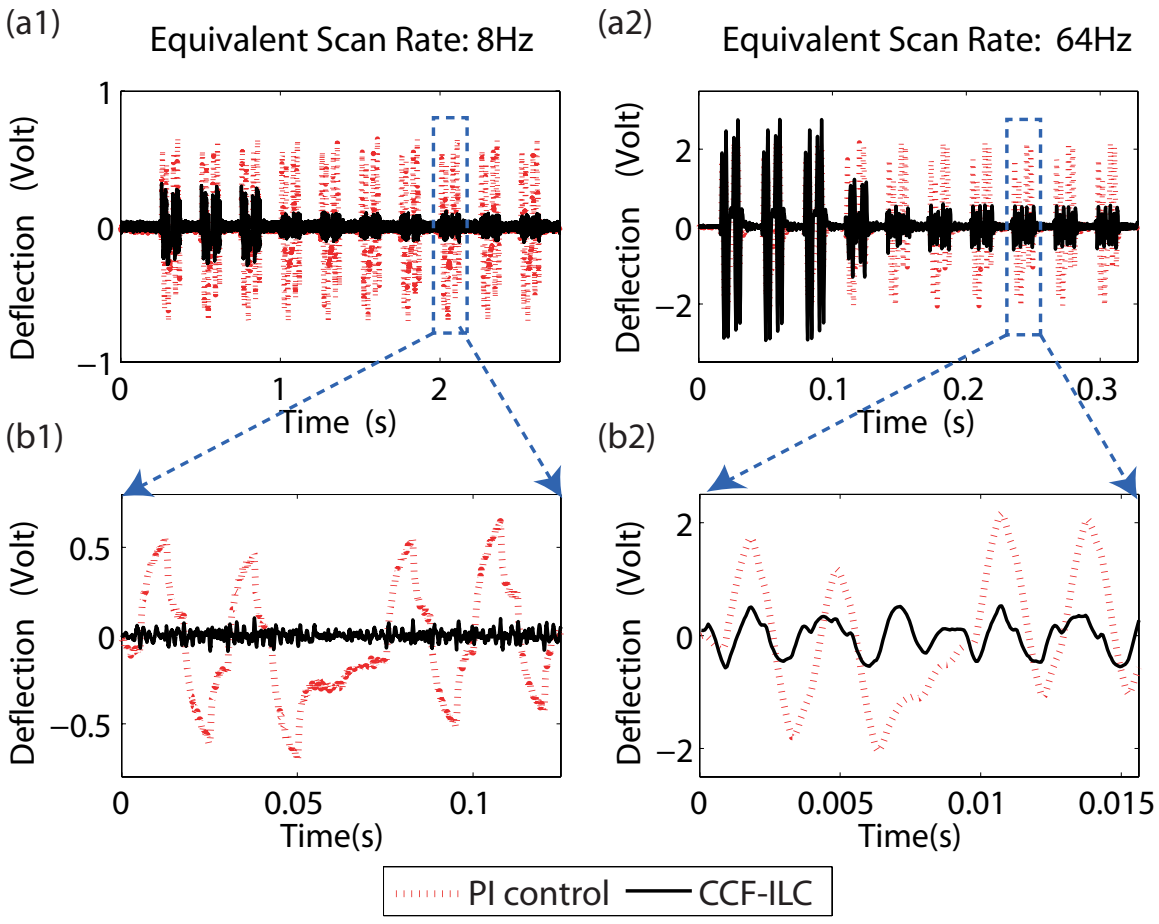

Figure 4.5 Comparison of the deflection signal (i.e., the residual error) obtained by using the PI controller and that by using the proposed CCF-ILC approach for the equivalent scan rates of (a1) 8Hz and (a2) 64Hz in "one point imaging", for 10 repetitive scans (Note the CCF-ILC control input was applied from the fourth scan), and the zoomed-in view of one scanline for the equivalent scan rates of (b1) 8 Hz and (b2) 64 Hz.

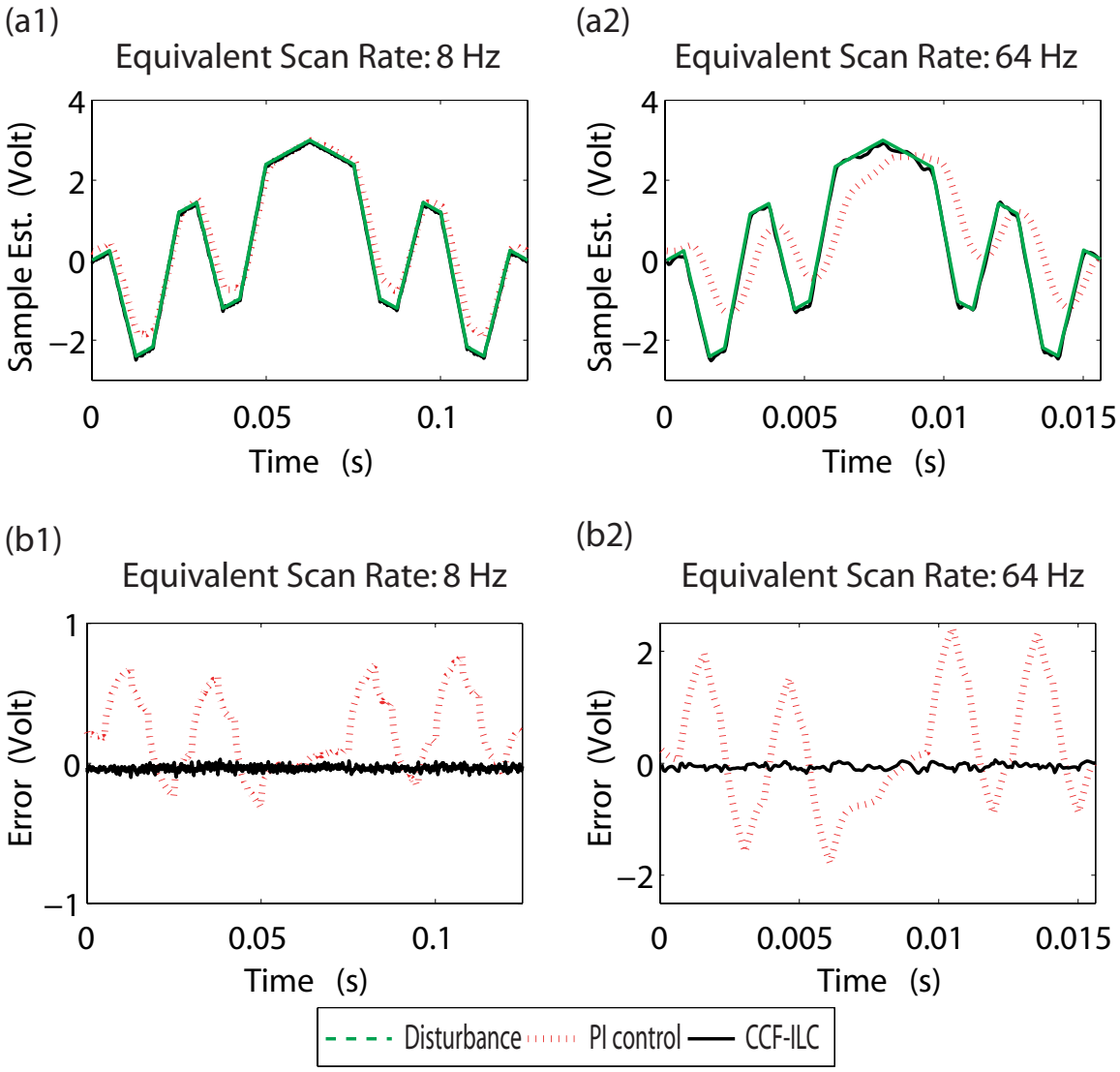

Figure 4.6 Comparison of the estimated "sample profile" by using PI control and the CCF-ILC approach for the equivalent scan rates of (a1) 8Hz (a2) 64Hz in "one point imaging", and (b1, b2) the corresponding estimation errors.

different scanning rates (8 Hz and 64 Hz) were used in the experiments, and the obtained disturbance trajectory for scan rate of 8 Hz is shown in Fig. 4.4. Then the CCF-ILC approach was used to account for such a disturbance trajectory of multiple periods (see Fig. 4.4 (a))– tracking multiple periods of the disturbance trajectory is equivalent to iteratively imaging on the same scanline. To compare the experimental results of the CCF-ILC approach with that of feedback alone, the feedforward control signal was not applied until the 4th period (see Fig. 4.5 (a)). The residual deflection errors are compared with the errors obtained by using the PI controller in Fig. 4.5. Then, the "sample profile" can be estimated by using the observer $R(j\omega)$, as described in Sec. 4.3.5. The obtained sample estimation is compared with that by using the commercial method (along with the PI controller) in Fig. 4.6.

The experimental results show that the proposed CCF-ILC approach significantly improved the AFM z-axis precision positioning in high-speed scanning. For both scan rates (8 Hz and 64 Hz), much smaller residual error (i.e., deflection signal change) was obtained by using the CCF-ILC approach than that by only using the robust feedback control or the PI feedback control. As shown in Fig. 4.5 (a1), (b1), for disturbance trajectory at equivalent scan rate of 8 Hz, the maximum residual error with the CCF-ILC approach was less than one third of that with the robust feedback control only (the first three periods tracking of the CCF-ILC approach in Fig. 4.5 (a1)), and is less than one seventh of that under the PI control only. When the "scan rate" was increased to 64 Hz, significant frequency components of the disturbance signal were beyond the feedback bandwidth, thereby larger residual error was generated under both the PI control and the robust feedback control. On the contrary, the residue error was maintained small by using the proposed CCF-ILC approach, and the tracking error was even similar than that by using (either robust or PI) feedback control only at "scan rate" of 8 Hz. We note that at 64 Hz tracking, the residual error under the robust feedback control only was slightly larger than that under the PI control. This is because the robust feedback controller was designed with emphasis on the robustness of the feedback control and the tracking precision at low frequency. We also note that, in both scan rates tracking, only one or

two iterations were needed, and the deflection error signal remained bounded throughout the iterations. Therefore, by using the CCF-ILC approach, the vertical z-axis positioning precision during high-speed scanning can be significantly improved over using feedback control only.

The experimental results also show that the CCF-ILC approach can significantly improve the sample profile estimation over the commercial PI-control approach. When the "scan rate" was relatively low (8 Hz), although the estimated disturbance trajectory (i.e., the estimated sample profile) obtained by using the PI control or the CCF-ILC approach were both close to the "true" sample profile (see Fig. 4.6 (a1), the estimation error with the use of the CCF-ILC approach was still over 10 times smaller than that with the PI control (see Fig.4.6 (a1), (b1)). When the "scan rate" increased much higher to 64 Hz, the imaging distortion/error was much more prononced (18 times larger) under the PI control than that under the CCF-ILC approach, as shown in Fig. 4.6 (a2) (b2), and the imaging error under the CCF-ILC approach is only 4.4% of the sample profile size. Therefore, the experiment results demonstrate that precise sample estimation can be obtained by using the proposed CCF-ILC appraoch for high-speed AFM imaging.

One line imaging

Next, the proposed CCF-ILC technique was implemented to repetitively scan a calibration sample (TGZ02, MikroMasch, with a nominal pitch size of 3 μm and nominal step height of 84 nm) on the same scanline. The precision positioning in the lateral scanning was achieved by using the inversion-based iterative control (IIC) approach [54]. It has been shown [54] that this IIC technique can effectively compensate for both the vibrational dynamics and the hysteresis effects simultaneously in high-speed, large-range lateral scanning. In this experiments, the maximum relative tracking error of the lateral scanning was maintained to be less than 1% (of the scan range of 20 μm) throughtout all four different scanning rates (8 Hz, 16 Hz, 32 Hz, and 64 Hz). The obtained deflection error signals are compared with those obtained by using the PI control in Fig. 4.7 (the first row for the total of ten repetitive scannings, and the second

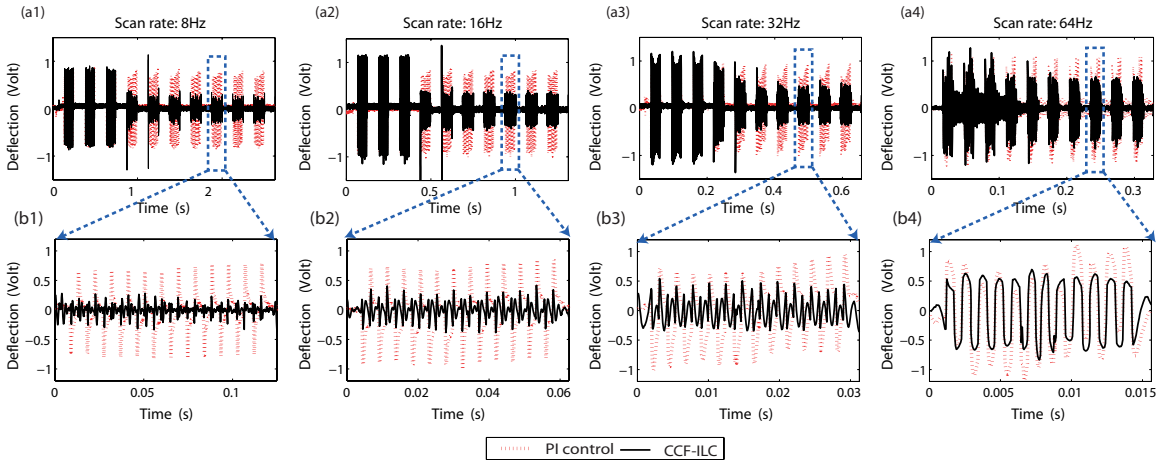

Figure 4.7 Comparison of the deflection error (the residual error) by using by using the proposed CCF-ILC approach with that by using the PI control for four different scan rates of (a1, b1) 8Hz, (a2, b2) 16Hz, (a3, b3) 32Hz, and (a4, b4) 64Hz in one scanline imaging, where the first row shows the total of 10 repeated scan result with the feedforward control input applied from the fourth scan; and the scecond row is the zoomed-in view of one scanline results. The lateral scan range is 20 μ m.

row for the zoomed-in view of one period scan).

The experimental results show that by using the proposed CCF-ILC approach, much smaller residual error was obtained than that by using the feedback control only. At the scan rate of 8 Hz, the maximum residual error under the CCF-ILC approach was 3 times smaller than that under the robust feedback control or under the PI control (The deflection error for the first three periods scanning under the CCF-ILC was obtained by using the robust feedback control only), as shown in Fig. 4.7 (a1) (b1). Such small residual error was maintained as the scan rate was doubled and quadrupled (see Fig. 4.7 (a2) (a3) (b2) (b3)). Even at the scan rate of 64 Hz, the residual error by using the CCF-ILC approach was still as small as that by using the feedback control only at 8 times lower scan rate (compare Fig. 4.7 (b1) with (b4)).

Compensation for the dynamics coupling To remove the dynamics-coupling effect in the obtained sample profile, we first used the proposed sample topography observer $R(j\omega)$ (see

Subsec. 4.3.5) to estimate the dynamics-coupling disturbance ($d_c(\cdot)$ in (4.25)), by scanning a flat sample with the proposed CCF-ILC technique: As (4.27) implies that when the sample was flat (i.e., compared to the dynamics-coupling effect, the sample topography variation was negligible, thereby $d_s(j\omega) \approx 0$ in (4.27)), the dynamics-coupling disturbance can be obtained by using the observer $R(j\omega)$ along with the feedforward control input $u_{k,FF}(j\omega)$ and the residual error $e_k(j\omega)$. The obtained dynamics coupling caused disturbance $d_c(\cdot)$ is shown in Fig. 4.8 for the four different scan rates (where the surface slope has been removed). The experimental results show that the dynamics coupling caused error increased as the scan rate increased. As shown in Fig. 4.8, at scan rate of 8 Hz, the dynamics coupling caused error was small ($\sim$5 nm). As the scan rate was further increased to 64 Hz, much larger (over four times larger than that at 8 Hz) coupling-caused oscillations occurred. Such large dynamics-coupling caused error must be accounted in AFM-imaging.

The sample estimation results obtained by using the CCF-ILC approach and those by using the PI control approach are compared in Fig. 4.9 for the four different scan rates, where the sample slope was removed from the sample estimation for the CCF-ILC approach. The sample slope was obtained by linearly line fitting the sample estimation obtained at low scan rate (8 Hz). The experimental results showed that, the proposed CCF-ILC approach can obtain a good sample profile estimation, even under the dynamics-coupling effect. At the scan rate of 8 Hz, the estimated sample profile obtained by using the CCF-ILC approach was close to the true sample profile (the rectangle pitches can be clearly identified), whereas the estimated sample profile by using the PI control showed pronounced sample distortions (the top of the pitches were cornered around instead of being flat, see Fig. 4.9 (a)). As the scan rate was increased (to 16 Hz and 32 Hz), the estimation error became larger by using the PI control (where not only the top but also the bottom of the pitches were cornered around), while the sample profile can still be relatively well estimated by using the proposed approach. When the scan rate was further increased to 64 Hz, the imaging distortion was even more pronounced under the PI control—the basic shape of the sample surface cannot be recognized, and large variations

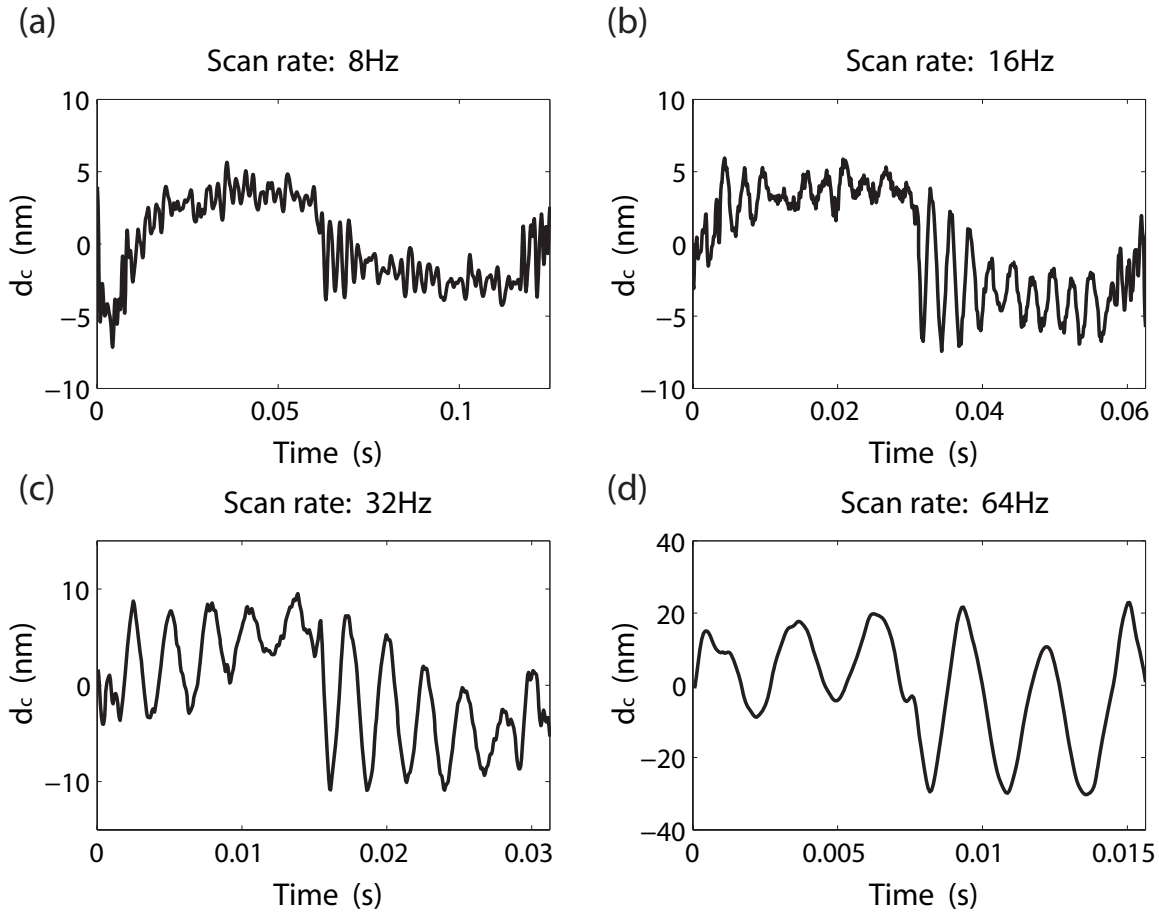

Figure 4.8 Dynamics-coupling caused disturbance $d_c(t)$ at four scan frequencies (a) 8 Hz, (b) 16 Hz, (c) 32 Hz, and (d) 64Hz.

occurred among the estimated pitches. On the contrary, by using the CCF-ILC approach, the sample estimation signal was still relatively close to the sample profile. Therefore, the experiment results showed that the proposed CCF-ILC appraoch can achieve a smaller tracking error as well as a better sample estimation than those obtained by using the feedback control alone.

4.5 Conclusion

A current cycle feedback iterative learning control approach was proposed in this chapter to achieve z-axis precision positioning during high-speed AFM-imaging. The CCF-ILC controller took the general ILC form consisting of two filters. First, The convergence of this CCF-ILC approach was investigated. Then secondly, with a robust-control based feedback controller already being designed, a two-step CCF-ILC controller design was proposed. The recently developed robust-inversion approach was used to design the inversion-based ILC filter, and a zero-phase low-pass filter was used to design the roll-off ILC filter. Moreover, a new sample profile observer was proposed which accounted for the dynamics-coupling effect. The proposed method was illustrated by implementing it to an AFM system. The experimental results showed that the imaging speed can be improved nearly 8 times by using the proposed technique than the conventional PI control method, and the sample estimation precision was also significantly improved.

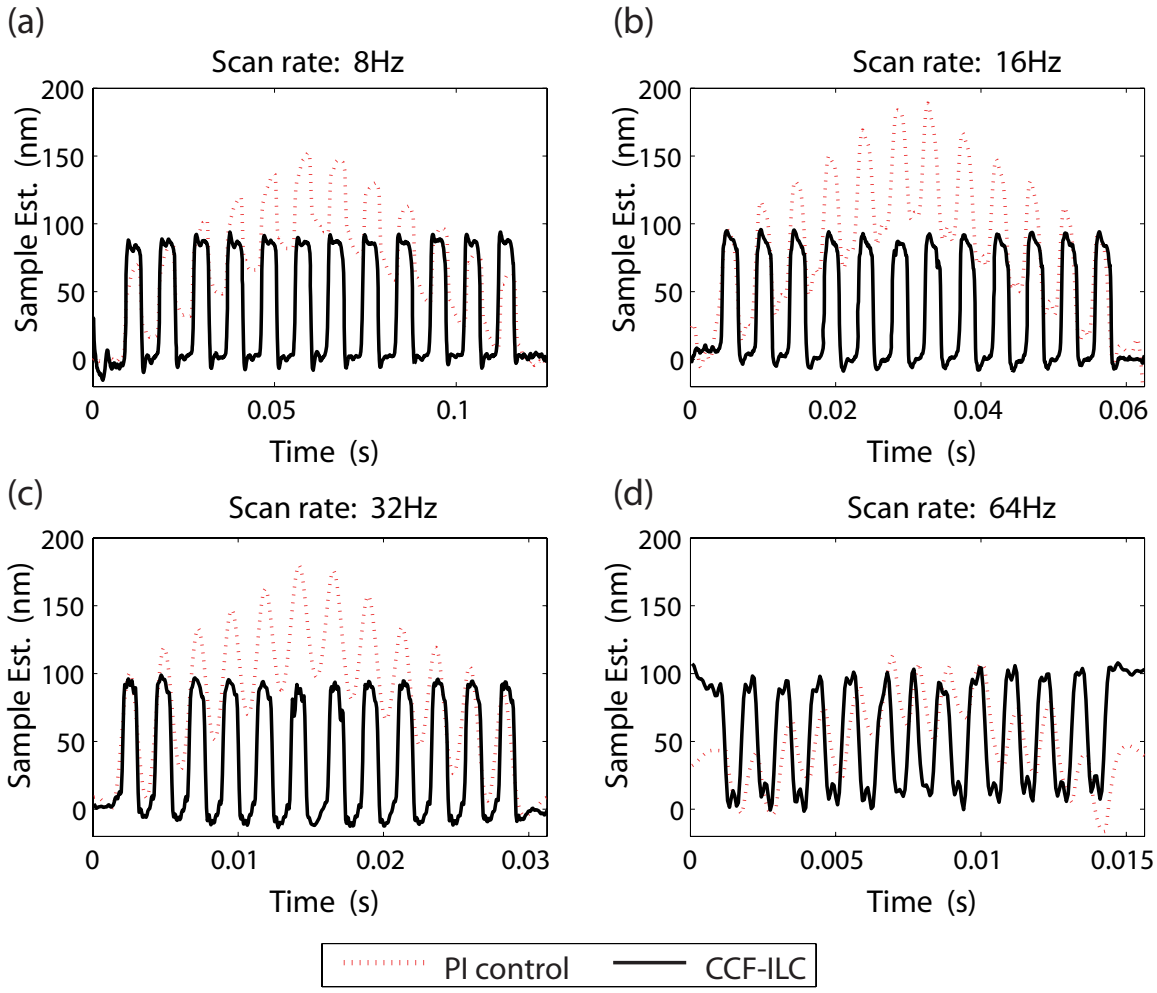

Figure 4.9 Comparison of the estimated sample profile of PI controller and CCF-ILC approach for the two scan frequencies (a) 8Hz, (b) 16 Hz, (c) 32 Hz, and (d) 64Hz (for single line scanning with scan range 20 μm).

CHAPTER 5. An iterative based feedforward-feedback control approach to high-speed AFM imaging

A paper to be published in the ASME Journal of Dynamic Systems, Measurement and Control

Ying Wu [1] and Qingze Zou [2]

Abstract

In this chapter, we propose an iterative-based feedforward-feedback control approach to achieve high speed AFM imaging. AFM imaging requires precision positioning of the AFM probe relative to the sample in all x-y-z axes. It has been demonstrated that, with advanced control techniques such as the inversion-based iterative-control (IIC) techniques, precision positioning of the probe in the lateral (x-y) scanning can be successfully achieved. Precision positioning of the probe in the vertical z-axis direction, however, is challenging because of issues such as the sample topography is unknown in general, the probe-sample interaction is complicated, and the probe-sample position is sensitive to the probe-sample interaction. Recently, the current-cycle-feedback iterative-learning-control (CCF-ILC) approach is proposed for high-speed AFM imaging. The CCF-ILC feedforward-feedback 2 degree-of-freedom (DOF) controller design has been successfully implemented for iteratively imaging on one scanline. In this chapter, we extend this CCF-ILC approach to the entire imaging of samples. The main contribution of this chapter is the analysis and the use of the CCF-ILC approach for tracking sample profiles with variations between scanlines (called line-to-line sample variations). The

[1]Primary researcher and author
[2]Author for correspondence

convergence of the CCF-ILC system is analyzed for the general case where the line-to-line sample variation occurs at each iteration. The allowable line-to-line sample profile variation is quantified. The performance improvement of the CCF-ILC is discussed by comparing the tracking error of the CCF-ILC technique to that of using feedback control alone. The proposed CCF-ILC control approach is illustrated by implementing it to the z-axis direction control in AFM imaging. Experimental results show that the imaging speed can be significantly increased by using the proposed approach.

5.1 Introduction

In this chapter, we propose an iterative-based feedforward-feedback control approach to achieve high speed AFM imaging. Since its invention [85], AFM has been established as an enabling tool to image as well as to manipulate matter at nanoscale [86]. Current AFM system, however, is slow and AFM imaging, therefore, is time consuming. Moreover, such slow speed of AFM has hindered the interrogation of nanoscale dynamic phenomena [57, 58]. For example, AFM enables the imaging of live biological samples in a biology-friendly environment. However, the AFM imaging time of at least several minutes is too slow to capture rapid biological phenomena occurring in seconds, such as the locomotion of living cells [16] and the dehydration process of collagen [61, 62]. As a result, large imaging distortion (i.e., temporal error) can be generated because the first pixel and the last pixel in the obtained image are acquired at very different time instants. AFM imaging requires precision positioning of the AFM probe relative to the sample in all x-y-z-axes, because large positioning error of the AFM-probe to the sample can lead to not only large imaging distortion [3], but also damage of the sample (when the sample is soft) [29], and/or the probe (when the sample is hard) [28]. Although precision positioning of the AFM-probe in high-speed lateral x-y axes scanning can be achieved by using recently-developed control techniques [54, 17] such as the inversion-based iterative learning control [54], challenges exist in the precision positioning of the AFM-probe in the vertical z-axis. These challenges arise because 1) the sample topography is unknown in general, 2) the probe-sample interaction is complicated due to the nonlinear dependence of the interaction force on the

probe-sample position as well as the deformation/reaction of the sample [59, 60], and 3) the relative probe-sample position is sensitive to the probe-sample interaction [60]. Therefore, precision positioning of the AFM probe in the vertical z-axis direction must be maintained to achieve high-speed AFM imaging.

Efforts have been made to improve the z-axis precision positioning of the probe during AFM imaging. For example, PID-type of controllers have been widely used in commercial AFM systems. The performance of such *ad-hoc* PID controllers, however, is limited by its low bandwidth and robustness [17], because of the low gain margin of the piezo actuators. Modern model-based feedback control approach increases the system bandwidth and achieves better robustness [17, 18]. However, the bandwidth and the robustness of feedback-based approaches are limited by the fundamental constrains of closed-loop feedback control: the overall performance and robustness of all feedback control systems is governed by the well-known Bode's integral [45], which implies that, in these advanced feedback control approaches, the closed-loop bandwidth has to be traded-off with the system robustness. Furthermore, piezo actuators tend to have nonminimum-phase dynamics characteristics [17, 20], while fundamental limit exists in the output tracking of such nonminimum-phase systems when using feedback control alone [44]. Therefore, z-axis positioning control of the AFM probe needs to be improved to achieve high-speed AFM imaging.

The constraints of feedback approaches to the z-axis positioning control of AFM probe can be alleviated with the two-degree-of-freedom (2-DOF) control scheme, by combining feedback with feedforward control. For example, it has been demonstrated in [43] that by using the H_∞ control theory to design the feedback and feedforward controllers in the 2DOF control system, the AFM imaging speed can be improved. However, limits still exist in such a 2DOF controller design. First, the H_∞-based design of feedforward control results in causal (i.e., stable) controllers, therefore, as piezo actuators tend to be nonminimum-phase, the performance of such feedforward controllers is limited. Moreover, the "bandwidth" of the feedforward control

is constrained by the bandwidth of the feedback control [43], because the current feedforward control signal was generated by using the total control signal from the last scanline in [43]. Thus, new approach needs to be developed to further exploit the benefits of 2DOF control approach for AFM-imaging,

Recently, the current-cycle-feedback iterative-learning-control (CCF-ILC) approach is proposed in [84] for high-speed AFM imaging. The CCF-ILC approach integrated the H_∞ robust control technique [45] with the inversion-based feedforward control technique [5, 20]. Particularly, the feedback controller is designed based on the H_∞ robust control theory, and the feedforward controller is designed based on the recently-developed robust-inversion technique [75]. The robust-inversion technique overcomes the causality limits and explicitly account for the uncertainties of system dynamics when finding the inverse feedforward controller [75]. Moreover, iteration is introduced to further exploit the priori knowledge of the sample profile in the AFM imaging, as well as to compensate for the disturbances and uncertainties effects. It has been shown [84] that the convergence of the CCF-ILC law can be guaranteed by a proper choice of the feedforward controller, and for any given feedback controller, the positioning precision can be significantly improved when using the CCF-ILC approach. As the first step, the CCF-ILC 2DOF controller design has been successfully implemented in [84] to iteratively image on the same scanline. In this chapter, we extend this CCF-ILC approach to the entire sample imaging.

The main contribution of this chapter is the analysis and the use of the CCF-ILC approach for AFM z-axis positioning with line-to-line sample variations. The convergence of the CCF-ILC law is discussed for the general case where the sample profile variation occurs at each iteration. Then, the CCF-ILC law is designed as in [84] and the performance of the CCF-ILC is discussed by comparing the tracking error of the CCF-ILC technique to that of using feedback control alone. It is shown that the CCF-ILC approach can improve the tracking even when the sample profile changes from one scanline to the next. Furthermore, the allowable sample pro-

file variation (to guarantee the convergence of the CCF-ILC law) is quantified. The proposed CCF-ILC control approach is illustrated by implementing it to the z-axis direction control in AFM imaging. Experimental results show that the speed of obtaining an entire image can be significantly increased by using the proposed approach.

The rest of the chapter is organized as follows. The general CCF-ILC framework is formulated in section 5.2 and the convergence of the CCF-ILC approached is analyzed. In Section 5.3, the design of the CCF-ILC is presented, and the tracking performance of the CCF-ILC approach is discussed by quantifying allowable line-to-line sample variations in Section 5.4, followed by the implementation of the proposed approach to the z-axis direction control in AFM imaging in Section 5.5, where the experimental results are also presented and discussed. Our conclusions are given in Section 5.6.

5.2 Problem formulation and Convergence Analysis

In this section, we formulate and discuss the CCF-ILC approach to the vertical positioning of the AFM probe, when there exists line-to-line sample variation. We start with briefly describing the feedback control system of z-axis for the AFM imaging.

In general, the feedback control system for z-axis AFM probe positioning can be schematically presented by Fig. 5.1(a), where $G_z(s)$ denotes the dynamics model of the piezo actuator for the z-axis positioning, $G_c(s)$ denotes the cantilever-photodiode dynamics (from the output of the z-axis piezo to the cantilever deflection), $K_s(s)$ denotes the photodiode sensitivity, $d_s(\cdot)$ denotes the sample profile, and $n_s(\cdot)$ denotes the system noise. The goal of the z-axis AFM probe positioning is to maintain a constant setpoint value (i.e., constant normal force between the tip and the sample) during the scanning process. Then the image of the sample topography can be estimated using the control signal or the deflection error [76].

Unlike the above feedback-based approach to z-axis positioning, the proposed CCF-ILC ap-

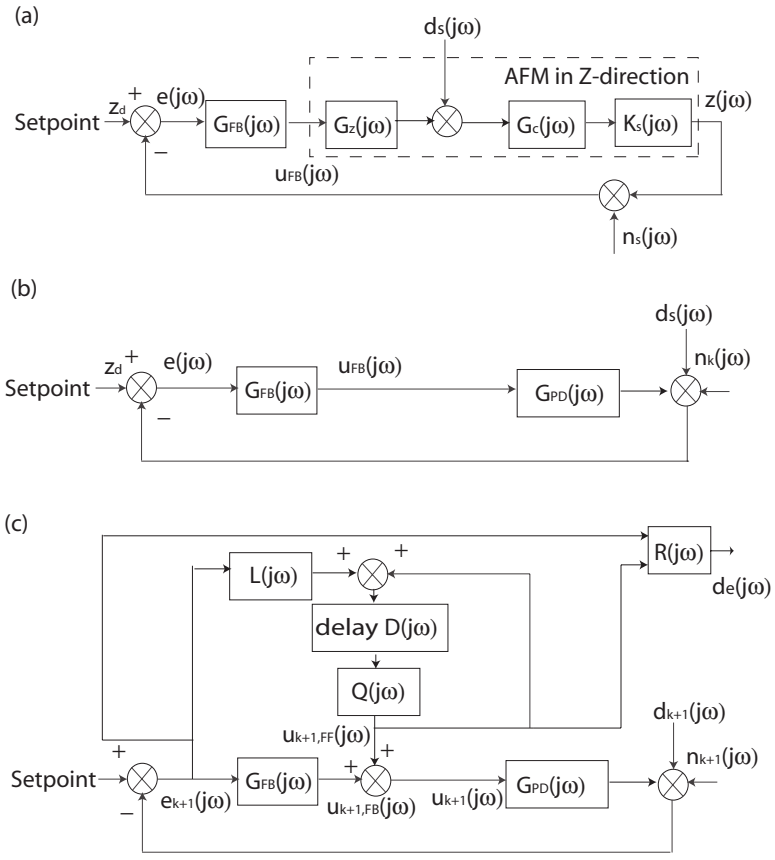

Figure 5.1 The block diagram of (a) a standard feedback loop, (b) the modified feedback loop, and (c) the proposed CCF-ILC approach for the vertical z-axis positioning in AFM imaging.

proach integrates an online iterative-learning control (ILC) as feedforward to the z-axis feedback control. First, to simplify the presentation of the controller design, the unknown sample profile is scaled with the DC-gain of the cantilever-photodiode dynamics $G_c(0)$, and then right-shifted to the joint point at the cantilever deflection output in the control block diagram, as shown in Fig. 5.1 (b) (The same notation $d_s(\cdot)$ is used for simplification). Such a signal-shift is feasible because the bandwidth of the cantilever-photodiode dynamics tends to be much higher (over 10 times) than that of the z-axis piezo dynamics. Thus, the proposed CCF-ILC controller can be schematically shown in Fig. 5.1 (c), where $Q(j\omega)$ and $L(j\omega)$ are the ILC filters to be designed, '`delay` $D(j\omega)$' denotes the one-scanline-period delay, and $R(j\omega)$ denotes the observer to be designed for obtaining the measured sample profile $d_e(j\omega)$. Specifically, the objectives of the proposed CCF-ILC design are that, during the entire imaging process, the CCF-ILC system should

1. guarantee the convergence of the CCF-ILC approach, i.e., the feedforward control input $u_{k,FF}(j\omega)$ remains bounded for all iterations ($\forall k > 1$) when there exists line-to-line sample variations between each iteration, and the residual error $e_k(j\omega)$ converges to zero when the noise $n(j\omega)$ and the line-to-line sample variation vanishes;

2. improve the output tracking with the augmented feedforward control, i.e., for the same feedback controller, the tracking error $e(j\omega)$ (e.g., the deflection signal) when using the CCF-ILC approach is smaller than that when using the feedback control alone; and

3. improve the imaging accuracy (denoted as $d_e(j\omega)$ in Fig. 5.1 (c)) , i.e., the estimation of the sample profile $d_s(j\omega)$, is more accurate than the estimation obtained by using current commercial AFMs.

In the proposed CCF-ILC technique, a stabilizing feedback controller $G_{FB}(s)$ is designed first—the feedback controller $G_{FB}(s)$ guarantees that the feedback loop is internally stable [45]. This implies that the first objective of the proposed controller design requires all the signals in the control system (Fig. 5.1 (c)) to be bounded throughout the iterations. It is noted that the z-axis positioning of the AFM probe can be sensitive to effects such as the variation of the

cantilever type and/or mounting, the setpoint value of the loading force (i.e., the cantilever deflection), and the measurement noise [80]. Therefore, the feedback controller is designed to enhance the robustness of the entire control system against these adverse effects. We design the feedback controller by using the robust control technique [84, 75] (The readers are referred to [75] for details). In the following, we assume that such a feedback controller has already been in place.

5.2.1 CCF-ILC Design: Convergence Analysis

In the proposed CCF-ILC approach, the following general form of the linear iterative learning control law is employed [10]:

$$\begin{aligned} u_{0,FF}(j\omega) &= 0 \\ u_{k+1,FF}(j\omega) &= Q(j\omega)(u_{k,FF}(j\omega) + L(j\omega)e_k(j\omega)), \qquad \text{for } k \geq 1 \end{aligned} \tag{5.1}$$

where $Q(j\omega)$ and $L(j\omega)$ are the ILC filters to be designed, and the filter $Q(j\omega)$ is factored out without loss of generality. We note that the CCF-ILC approach can be implemented in several different schemes. For example, the CCF-ILC algorithm can be applied to repeatedly image on the first scanline until the required imaging precision (i.e., tracking precision) is achieved before moving to image at the next scanline. Or alternatively, the CCF-ILC approach can be applied to image at each scanline with a pre-chosen number of iterations. These schemes are all special cases of the more general one where the line-to-line sample profile variation occurs at each iteration. Thus, we discuss next the conditions to guarantee the convergence of the CCF-ILC law (the first design objective) for this general scenario.

Lemma 6 *Let $G_{PD}(j\omega)$ be the frequency response of a linear time invariant plant, and let $G_{FB}(j\omega)$ be a stabilizing feedback controller. Then for bounded measurement noise $n_k(jw)$ during the k^{th} iteration, i.e., $|n_k(j\omega)| \leq \delta(\omega)$, and bounded modified line-to-line sample variation as defined below,*

$$\widehat{\Delta d}_k(\omega) \triangleq |Q(j\omega)d_k(j\omega) - d_{k+1}(j\omega)| \leq \max_k \widehat{\Delta d}_k(\omega) \triangleq \widehat{\Delta d}_{\max}(\omega), \tag{5.2}$$

both the iterative control input $u_k(j\omega)$ and the residual error $e_k(j\omega)$ are bounded throughout the iterations, provided that the following iteration coefficient $\rho(j\omega)$ is less than one, i.e.,

$$\rho(\omega) = |Q(j\omega)\{1 - G_{PD}(j\omega)S(j\omega)L(j\omega)\}| < 1. \tag{5.3}$$

Moreover, the residual error $e_k(j\omega)$ is bounded by an affine function of the maximum modified line-to-line sample variation $\widehat{\Delta d}_{\max}(j\omega)$ and the noise level $\delta(\omega)$

$$|e_\infty(j\omega)| \triangleq \lim_{k\to\infty} |e_k(j\omega)| \le \left|\frac{S(j\omega)}{1-\rho(\omega)}\right| \left|\widehat{\Delta d}_{\max}(j\omega)\right| + \mathbf{E}_\delta(j\omega)\delta(\omega), \tag{5.4}$$

where the limit of the residual error $e_\infty(j\omega)$ is called the ultimate ILC error*, and the frequency dependent coefficient $\mathbf{E}_\delta(j\omega)$ is defined as*

$$\mathbf{E}_\delta(\omega) \triangleq \frac{|Q(j\omega)G_{PD}(j\omega)S(j\omega)L(j\omega)S(j\omega)| + |S(j\omega)|}{|1-\rho(\omega)|} \tag{5.5}$$

Proof We proceed by quantifying the residual error $e_k(j\omega)$ for given noise/disturbance $n_k(j\omega)$. Note that from the block diagram in Fig. 5.1 (c), for any given stabilizing feedback controller, the feedforward control input $u_{k,FF}(j\omega)$ in the k^{th} iteration can be written as

$$u_{k,FF}(j\omega) = S^{-1}(j\omega)G_{PD}^{-1}(j\omega)\left[-e_k(j\omega) - S(j\omega)d_k(j\omega) - S(j\omega)n_k(j\omega)\right] \tag{5.6}$$

In the following derivation, the dependence on $j\omega$ is omitted for economy. Substituting Eq. (5.6) into Eq. (5.1) leads to

$$G_{PD}^{-1}\left[-e_{k+1} - Sd_{k+1} - Sn_{k+1}\right] = QG_{PD}^{-1}\left[-e_k - Sd_k - Sn_k\right] + SQLe_k \tag{5.7}$$

Then the residual error at the next iteration $k+1$ can be obtained from Eq. (5.7) as

$$
\begin{aligned}
e_{k+1} &= Q\left(1-G_{PD}SL\right)e_k + (Qd_k - d_{k+1})S + QSn_k - Sn_{k+1} \\
&= Q\left(1-G_{PD}SL\right)\left\{Q\left(1-G_{PD}SL\right)e_{k-1} + (Qd_k - d_{k+1})S\right\} \\
&\quad + QSn_{k-1} - Sn_k + (Qd_k - d_{k+1})S + QSn_k - Sn_{k+1} \\
&= \cdots \\
&= \left\{Q\left(1-G_{PD}SL\right)\right\}^{k+1} e_0 + \sum_{j=0}^{k}\left\{Q\left(1-G_{PD}SL\right)\right\}^{j}(Qd_k - d_{k+1})S \\
&\quad + \sum_{j=0}^{k}\left\{Q\left(1-G_{PD}SL\right)\right\}^{j} QSn_{k-j} - \sum_{j=0}^{k}\left\{Q\left(1-G_{PD}SL\right)\right\}^{j} Sn_{k+1-j} \qquad (5.8)
\end{aligned}
$$

By changing the index used in the last term in Eq. (5.8), the last two terms in Eq. (5.8) can be simplified as:

$$
\begin{aligned}
&\sum_{j=0}^{k}\left\{Q\left(1-G_{PD}SL\right)\right\}^{j} QSn_{k-j} - \sum_{j=0}^{k}\left\{Q\left(1-G_{PD}SL\right)\right\}^{j} Sn_{k+1-j} \\
= &\sum_{j=0}^{k}\left\{Q\left(1-G_{PD}SL\right)\right\}^{j} QSn_{k-j} - \sum_{j=0}^{k}\left\{Q\left(1-G_{PD}SL\right)\right\}^{j+1} Sn_{k-j} \\
&- sn_{k+1} + \left\{Q\left(1-G_{PD}SL\right)\right\}^{k+1} sn_0 \\
= &\sum_{j=0}^{k}\left\{Q\left(1-G_{PD}SL\right)\right\}^{j}\left\{Q - Q(1-GSL)\right\} Sn_{k-j} - sn_{k+1} + \left\{Q\left(1-G_{PD}SL\right)\right\}^{k+1} sn_0 \\
= &\left\{\sum_{j=0}^{k}\left\{Q\left(1-G_{PD}SL\right)\right\}^{j} QG_{PD}SLSn_{k-j}\right\} - sn_{k+1} + \left\{Q\left(1-G_{PD}SL\right)\right\}^{k+1} sn_0 \qquad (5.9)
\end{aligned}
$$

Substituting Eq. (5.9) into Eq. (5.8) and using triangle inequality, the iterative residual error e_{k+1} can be bounded as

$$\begin{aligned}
|e_{k+1}| &\leq |\{Q(1-G_{PD}SL)\}|^{k+1}|e_0| + \sum_{j=0}^{k}|\{Q(1-G_{PD}SL)\}|^{j}|(Qd_k - d_{k+1})S| \\
&\quad + \sum_{j=0}^{k}|Q(1-G_{PD}SL)|^{j}|QG_{PD}SLS||n_{k-j}| + \left|\{Q(1-G_{PD}SL)\}^{k+1}Sn_0 - Sn_{k+1}\right| \\
&\leq \rho^{k+1}|e_0| + \left|\widehat{\Delta d}_{\max}S\right|\sum_{j=0}^{k}\rho^{j} + (1+\rho^{k+1})|S\delta| + |QG_{PD}SLS||\delta|\sum_{j=0}^{k}\rho^{j} \\
&\quad \text{(By definitions of } \widehat{\Delta d} \text{ and } \rho \text{ in Eqs. (5.3, 5.5))} \\
&\leq \rho^{k}|e_0| + \frac{\widehat{\Delta d}_{\max}S(1-\rho^{k})}{1-\rho} + \frac{|QG_{PD}SLS||\delta|(1-\rho^{k})}{1-\rho} + (1+\rho^{k+1})|S||\delta|. \qquad (5.10)
\end{aligned}$$

Thus, it is evident from the above Eq. (5.10) that when the iteration coefficient $\rho(\omega) < 1$, the tracking error e_k is bounded for all iterations $k \geq 1$, and the ultimate error, $|e_\infty|$ is eventually bounded as in Eq. (5.4) when $k \to \infty$. Similarly, it can be shown that under the same condition (i.e., $|\rho(\omega)| < 1$), the iterative control input, $u_k(j\omega)$, is also bounded for all iteration $k \geq 1$. This completes the proof. ■

Lemma 6 implies that, for the special case where the line-to-line sample variation vanishes, for example, when repetitively imaging on the same scanline as in [84], the CCF-ILC law (5.1) should also converge. Particularly, it can be easily verified that in this case the ultimate error bound in Eq. (5.4) reduces to the ultimate error bound given in [84].

Corollary 3 *Let the conditions in Lemma 6 hold, then when the line-to-line sample variation vanishes, i.e., $d_k(j\omega) = d_{k+1}(j\omega) = d(j\omega)$ for $\forall k > 1$, the ultimate error bound $|e_\infty(j\omega)|$ becomes*

$$|e_\infty(j\omega)| \triangleq \lim_{k\to\infty}|e_k(j\omega)| \leq \left|\frac{\mathbf{E}_d(\omega)}{1-\rho(\omega)}\right||d_s(j\omega)| + \mathbf{E}_\delta(\omega)\delta(\omega), \qquad (5.11)$$

where $\rho(\omega)$ and $E_\delta(\omega)$ are as defined before in Eqs. (5.3,5.5), respectively, and the coefficient

E_d is given by

$$\mathbf{E}_d(\omega) \triangleq |(Q(j\omega) - 1)S(j\omega)| \tag{5.12}$$

Lemma 6 implies that when the noise effect is small ($\delta(j\omega) \to 0$), the bound of the residual error is monotonically decreasing with iterations (see Eq. (5.10)). Thus, to guarantee the overall imaging quality in implementations, it is preferred to iteratively image on one scanline until the residual error is smaller than a user-chosen thresh-hold value, then proceed the imaging on the rest of scanlines with a pre-chosen, given number of iterations. Therefore, we propose to design the CCF-ILC filters $Q(j\omega)$ and $L(j\omega)$ for repetitively imaging on one scanline as in [84], and then quantify the size of the allowable line-to-line sample variation such that the imaging on the rest of scanlines can be proceeded with no iterations (i.e., scan once at each scanline).

Remark 17 *We note that the modified line-to-line variation defined in Eq. (5.2) is different from the line-to-line sample variation — the sample profile on the current scanline is multiplied by the ILC filter $Q(j\omega)$. This is because in the CCF-ILC control law (5.1), the sample topography information of current scanline passes through the ILC filter $Q(j\omega)$ before it is used to update the tracking for the next scanline.*

Remark 18 *The proposed CCF-ILC approach aims at achieving high-speed imaging of samples with relatively smooth topography (i.e., the line-to-line sample variation is relatively small). Such smooth samples exist in a wide variety of areas, including semiconductor and optical industry [77], nano-/bio-materials [78], and biology [79].*

5.3 Controllers Design

As in [84], a two-step approach to design the CCF-ILC filters is proposed. Note that by Lemma 6, the filter $L(j\omega)$, in general, should approximate the inverse of the closed-loop transfer function $G_{PD}(j\omega)S(j\omega)$ (to render the iterative coefficient $\rho(j\omega)$ and thereby the ultimate error $e_\infty(j\omega)$ small, see Eqs. (5.3, 5.4)), and the filter $Q(j\omega)$ should be as close as possible to one in the low frequency range (to drive the ultimate error to 0) while compensating for

the model uncertainties and noise effect in the high frequency range, i.e., $Q(j\omega)$ possess the characteristics of a low-pass filter. Thus in the following, we call $L(j\omega)$ the 'inversion-based ILC filter' and $Q(j\omega)$ the 'roll-off ILC filter'.

Design of the inversion-based ILC filter $L(j\omega)$

The inversion-based ILC filter $L(j\omega)$ is designed to minimize the term $|1 - G_{PD}(j\omega)S(j\omega)L(j\omega)|$ in the iteration coefficient $\rho(\omega)$, by using the recently developed robust inversion technique [75]. We start with defining the model uncertainties as

$$\Delta G(j\omega) = \frac{G_L(j\omega)}{G_{L,m}(j\omega)} = \Delta r(\omega) \cdot e^{j\Delta\theta(\omega)}, \tag{5.13}$$

where $G_L(j\omega)$ denotes the true linear dynamics response of the system, e.g., for the z-axis AFM dynamics,

$$G_L(j\omega) = G_{PD}(j\omega)S(j\omega), \tag{5.14}$$

and $G_{L,m}(j\omega)$ denotes the model of the linear dynamics $G_L(j\omega)$. Then the inversion-based ILC filter $L(j\omega)$ is designed as

$$L(j\omega) = \alpha_{opt}(\omega) \cdot G_{L,m}^{-1}(j\omega), \tag{5.15}$$

where $\alpha_{opt}(\omega)$ is the optimal frequency-dependent gain to compensate for the dynamics uncertainty of the system $G_L(j\omega)$, i.e., the optimal gain $\alpha_{opt}(j\omega)$ is sought to minimize the feedforward tracking error, $|1 - G_{PD}(j\omega)S(j\omega)L(j\omega)|$, with the presence of the dynamics uncertainty $\Delta G(j\omega)$,

$$\min_{L(j\omega)} \sup_{\Delta G} \left|1 - G_{PD}(j\omega)S(j\omega)L(j\omega)\right| = \min_{\alpha(j\omega)} \sup_{\Delta G} \left|1 - \alpha(\omega)\Delta G(j\omega)\right| \ \rightarrow \alpha_{opt}(\omega). \tag{5.16}$$

It can be shown that the optimal gain $\alpha_{opt}(j\omega)$ is given as [75]

$$\alpha_{opt}(\omega) = \begin{cases} \frac{2\cos(\Delta\theta_m(\omega))}{\Delta r_{\min}(\omega)+\Delta r_{\max}(\omega)} & \omega \in \Omega_c, \\ 0 & \text{otherwise.} \end{cases} \tag{5.17}$$

where $\Delta r_{\min}$, $\Delta r_{\max}$ and $\Delta\theta_m$ are the bounds to quantify the system uncertainties, i.e.,

$$\begin{aligned} \Delta r(j\omega) &\in [\Delta r_{min}(j\omega), \Delta r_{\max}(j\omega)] \\ |\Delta\theta(j\omega)| &\leq |\Delta\theta_m(j\omega)| < \pi/2 \qquad \text{for } \omega \in \Omega_c \end{aligned}$$

and the set Ω_c contains the frequencies where the phase variation is less than $\pi/2$, i.e.,

$$\Omega_c \triangleq \left\{\omega \in \Omega_c \middle| |\Delta\theta(j\omega)| < \pi/2 \text{ for } \omega \in \Omega_c\right\}. \tag{5.18}$$

Then with the robust inverse filter (5.15, 5.17), the term $|1 - G_{PD}(j\omega)S(j\omega)L(j\omega)|$ is minimized for bounded dynamics uncertainties,

$$\min_{\alpha} \sup_{\Delta G} \left|1 - G_{PD}(j\omega)S(j\omega)L(j\omega)\right| = \begin{cases} \sqrt{1 - \frac{4\cos^2(\Delta\theta_m(\omega))\Delta r_{\min}(\omega)\Delta r_{\max}(\omega)}{(\Delta r_{\min}(\omega)+\Delta r_{\max}(\omega))^2}} & \omega \in \Omega_c, \\ 1 & \text{otherwise.} \end{cases} \tag{5.19}$$

Design of the roll-off ILC filter $Q(j\omega)$

Secondly, we design the roll-off ILC filter $Q(j\omega)$ as a zero-phase low-pass filter to ensure the convergence of the CCF-ILC algorithm, and render a small ultimate error $e_\infty(j\omega)$ (see Eq. (5.4)). To facilitate the implementation, the zero-phase low-pass filter $Q(j\omega)$ is given in z-transfer function in the discrete-time:

$$Q(z) = b_0 + \sum_{k=1}^{N}(b_k z^k) + \sum_{k=1}^{N}(b_k z^{-k}) \tag{5.20}$$

where the coefficients $b_k \in \Re$. It can be easily verified that the frequency response of $Q(e^{j\omega T})$ is real—thus the phase of $Q(z)$ is zero, i.e.,

$$Q(e^{j\omega T}) = b_0 + \sum_{k=1}^{N}(2b_k \cos\omega NT) \in \Re. \tag{5.21}$$

It is evident from (5.20) that the zero-phase FIR filter is noncasual. Such a noncausal filter, however, is implementable in the proposed CCF-ILC framework because the signal to be filtered is the sample profile from the previous scanline, thereby completed known ahead—as long as the filter order N is not larger than the total sampling points on one scanline. The ILC roll-off filter $Q(j\omega)$ is realized by combining a linear phase FIR low-pass filter with a linear phase lead,

$$Q(z) = Q_l(z) \times z^P \tag{5.22}$$

where $Q_l(z)$ is the linear-phase FIR low-pass filter (Matlab command "firpm"). Note that the phase lead term z^P in Eq. (5.22) is simply a P-step forward shift in discrete-time implementation. Also the signal $L(j\omega)e_k(jw)$ and the feedforward control signal $u_{k,FF}(j\omega)$ from the

previous scanline was delayed by one scanning period and applied as the input in the CCF-ILC algorithm, i.e., the residual error signal was delayed by N-step (N: number of sampling points per scanline) in implementations. Therefore, the P-step phase lead can be combined with the N-step delay in implementations (denoted as the delay term "$D(j\omega)$" in Fig. 5.1(c)).

5.4 Tracking improvement

To show that the CCF-ILC approach can enhance the total imaging performance over feedback control alone, the tracking error of using the CCF-ILC approach is compared with that of using the feedback control alone (the second design objective). We first discuss the enhancement when the line-to-line sample variation is ignored (i.e., when using the CCF-ILC algorithm to repetitively image on the same scanline).

5.4.1 No line-to-line sample variation case

It can be shown that in this case the ultimate error of the CCF-ILC approach, $|e_\infty(\cdot)|$, is less than or equal to the residual error with feedback only, $|e_{FB}(\cdot)| = |S(j\omega)d(j\omega)|$, when the noise is negligible, i.e., $\delta(\omega) = 0$. By Eq. (5.4), when the noise is ignored, the ratio of the ultimate error of the CCF-ILC approach with respect to the feedback control error, $q(\omega)$, becomes

$$\begin{aligned} q(\omega) &= \frac{|e_\infty(j\omega)|}{|e_{FB}(j\omega)|} \\ &= \frac{|1 - Q(j\omega)|}{|1 - |Q(j\omega)|\,|1 - G_{PD}(j\omega)S(j\omega)L(j\omega)||} \\ &= \frac{|1 - Q(j\omega)|}{|1 - \rho(\omega)|}. \end{aligned} \tag{5.23}$$

Then the discussion is proceeded by considering the tracking within and outside the frequency set Ω_c separately,

1. In the frequency set Ω_c where the dynamics variation is small and the CCF-ILC controller $L(j\omega)$ is applied, the term $|1 - G_{PD}(j\omega)S(j\omega)L(j\omega)|$ in the error ratio (5.23) is less than one (as shown in (5.19)). Consequently, the error ratio is less than one, $q(\omega) < 1$, because the ILC filter $Q(j\omega)$ is a zero phase low-pass filter and $Q(j\omega) \leq 1$ for frequency $\omega \in \Omega_c$;

2. At other frequencies where the dynamics variation is large and the CCF-ILC controller $L(j\omega)$ is set to zero, the term $|1 - G_{PD}(j\omega)S(j\omega)L(j\omega)| = 1$ (see (5.19)), and thereby the error ratio $q(\omega)$ equals to one.

Thus by the continuity of the system dynamics, the above discussion implies that when the noise/disturbance is small and the line-to-line variation is ignored, the use of the proposed CCF-ILC approach will enhance the tracking performance.

5.4.2 Line-to-line variation case

Next, we consider the more general case where the line-to-line sample profile variation occurs at each iteration, i.e., $|d_k - d_{k+1}| \geq 0$ for $k \geq 1$. Similar in Section 5.4.1, the CCF-ILC ultimate error, $e_\infty(j\omega)$, is compared with the error of feedback only, $|e_{FB,max}(\cdot)| \triangleq |S(j\omega)|\,|d_{\max}|$, where $d_{\max} = \max_k d_k$ (Note the ultimate error $e_\infty(j\omega)$ is the upper bound of the limit of the residual error when using the CCF-ILC). The following lemma provides a sufficient condition to guarantee that the CCF-ILC approach will improve the tracking over feedback alone.

Lemma 7 *Let the noise effect n_k be negligible, the use of the proposed CCF-ILC approach will enhance the tracking performance, i.e.,*

$$|e_\infty(j\omega)| \leq |e_{FB,max}(j\omega)| \ \ \textit{for } \omega \in \Omega_c, \tag{5.24}$$

if the relative line-to-line sample variation $\Delta R_d(\%)$ is bounded as

$$\Delta R_d(\%) \triangleq \left| \frac{\widehat{\Delta d}_{\max}(j\omega)}{d_{\max}(j\omega)} \right| \leq |1 - \rho(\omega)| \times 100\% \tag{5.25}$$

Lemma 7 can be easily proved by using Eq. (5.4) in Lemma 6. Note that in the low frequency range, the dynamics uncertainty tends to be small, so are the noise/disturbance effects. As a result, the inversion-based ILC filter $L(j\omega)$ can be chosen to render the iterative coefficient $\rho \to 0$, and the roll-off filter $Q(j\omega)$ can be chosen to be one. Therefore, the above Eq. (5.25) implies that large line-to-line sample variation can be allowed in the low-frequency range (or alternatively, when the imaging speed is relatively low). Next, we introduce a more conservative sufficient condition which quantifies the allowable line-to-line sample variation in terms of the

line-to-line variation directly (instead of the modified line-to-line variation $\widehat{\Delta d}_{\max}(j\omega)$, which depends on the ILC filter $Q(j\omega)$).

Corollary 4 *Let the noise signal n_k be negligible, there exist a positive frequency dependent coefficient*

$$\eta_v(\omega) \triangleq [|1-\rho(\omega)| - |Q(j\omega)-1|]\,|d_{\max}(\omega)| > 0 \quad \textit{for } \omega \in \Omega_c, \tag{5.26}$$

such that when the line-to-line variation is bounded by η_v, i.e.,

$$\max_k |d_k(j\omega) - d_{k+1}(j\omega)| < \eta_v(\omega), \tag{5.27}$$

the use of the proposed CCF-ILC approach will enhance the tracking performance.

Proof The discussion right after Eq. (5.23) shows that the Inequality (5.26) holds for frequencies $\omega \in \Omega_c$, therefore (5.27) leads to

$$\max_k |d_k - d_{k+1}| < \eta_v = [|1-\rho| - |Q-1|\,|]\,d_{\max}|\,. \tag{5.28}$$

By the definition of $d_{\max}$, the above equation yields

$$\max_k [|d_k - d_{k+1}| + |(Q-1)d_k|] < |1-\rho|\,|d_{\max}| \tag{5.29}$$

Then the Corollary follows by applying the triangle inequality to the above equation and Lemma 7 (Eq. (5.25)). ■

Obviously Corollary 4 shows that the CCF-ILC approach improves the tracking when the line-to-line variation is small, which agreed with our expectation. Since frequency dependent iterative coefficient $\rho(\omega)$ is less than one and the roll-off ILC filter $Q(j\omega)$ has low pass characteristics, it can be seen that the allowable line-to-line variation is larger in the low frequency range than that in high frequency range.

Remark 19 *Note that the discussion in this Section—the proposed CCF-ILC approach will improve the tracking over feedback only— holds regardless the type of the feedback controller $G_{FB}(j\omega)$, as long as the feedback controller $G_{FB}(j\omega)$ is a stabilizing controller.*

In [84], an observer that uses both feedforward signal $u_{ff}(\cdot)$ and deflection error $d(\cdot)$ to estimate the sample profile is proposed. The observer also accounts for the dynamics-coupling effect [84, 1] of vertical z-axis motion caused by the lateral input. On the contrary, the image is obtained through a quasi-static scaling on current commercial AFM (the sample profile is obtained by scaling the z-axis control input by the DC-Gain of the z-axis piezoactuator). Thus, the observer proposed in [84] can achieve better sample image than such quasi-static method, particularly in high-speed imaging (the third design objective). This is illustrated through experiments in the next section.

5.5 Experimental Example

We implement the proposed CCF-ILC approach on an AFM system ($Dimension^{TM}$ 3100, Veeco Inc.). The efficacy of the CCF-ILC approach to improve the imaging on one scanline (over using feedback control only) has been demonstrated through experiments in [84]. In this paper, we focus on the use of CCF-ILC method to obtain an entire image.

The CCF-ILC law was designed by following the procedure described in Sec. 5.3, similar to the experiment example described in [84]. First, a stabilizing feedback controller $G_{FB}(s)$ was obtained (using robust-control technique). Secondly, the model uncertainty (variation) was quantified by using the measured system dynamics. The quantified uncertainty then was used to design the inversion-based ILC filter $L(j\omega)$. Finally, the roll off ILC filter $Q(j\omega)$ was designed as a zero-phase low pass filter. The readers are referred to [84] for details.

The experimental implementation was conducted in two stages. First, to exclude the effects due to the lateral-to-vertical dynamics coupling [1, 83] and lateral tracking errors [54, 17], "One point imaging" was conducted, where a trajectory that mimiced a calibration sample profile was applied as a disturbance input to the z-axis piezo actuator. This experiment allowed us to investigate the performance of the proposed CCF-ILC approach in z-axis tracking only (as similarly done in [76]). Then secondly, the proposed method was used to obtain an entire

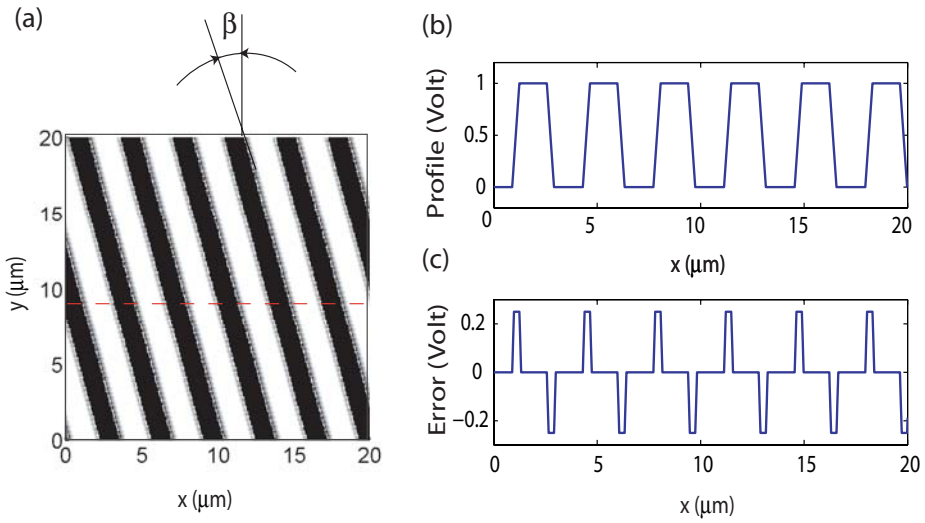

Figure 5.2 (a) The computer generated 'sample profile'; and (b) the cross section of one scanline; and (c) the line-to-line sample variation.

image of a calibration sample.

5.5.1 One point imaging

The disturbance trajectory was generated by mapping a simulation-generated sample profile (with no surface slope) to the lateral scanning period. Four different scan rates were used in the experiments, 8 Hz, 16 Hz, 32 Hz, and 64 Hz. The obtained 'sample profile' is shown in Fig. 5.2 (a) for the entire image and (b) one cross-section scanline, respectively. As seen in Fig. 5.2 (a), the 'sample profile' consists of array of steps, where the angle of the arrays with respect to the y-axis, $\beta = 15°$, quantified the existing line-to-line sample variation. Specifically, such a line-to-line sample variation is also shown in Fig. 5.2 (c). Here we assume the lateral equivalent scan range is 20×20 (μm $\times$ μm), and total of 64 scanlines (in y slow scan axis) was used in the experiment, the obtained "equivalent image" is shown in Fig. 5.2 (a). When using the CCF-ILC approach to image the generated 'sample profile', we iteratively imaged on the first scanline (until the residual error did not reduce further), then proceeded the imaging on the rest of the scanlines with no iteration. The residual deflection errors for the first 10

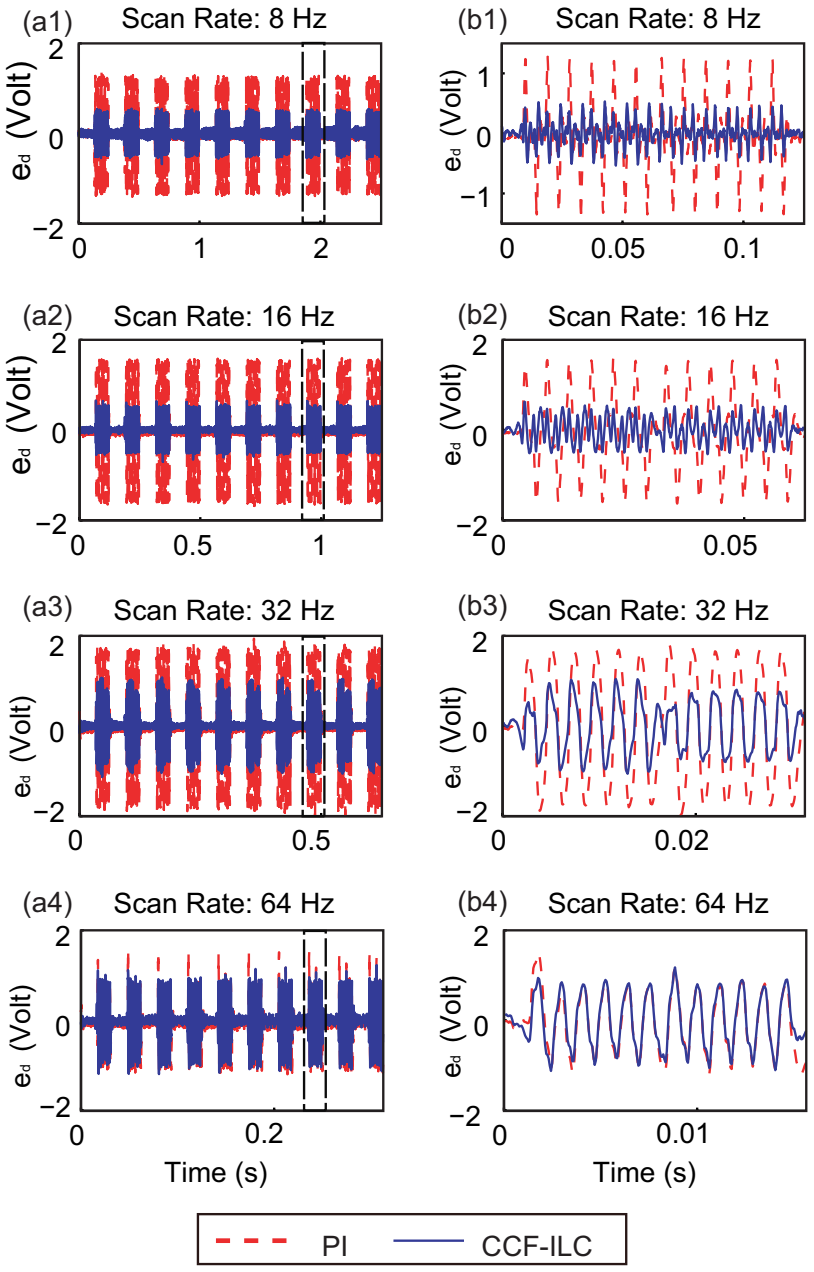

Figure 5.3 Comparison of the deflection error (the residual error) by using the proposed CCF-ILC approach with that by using the PI control for four different equivalent scan rates of (a1, b1) 8Hz, (a2, b2) 16Hz, (a3, b3) 32Hz, and (a4, b4) 64Hz in one point imaging, where the left column shows the total of 10 repeated scan result; and right column is the zoomed-in view of one scanline results within the dashed window in the left column.

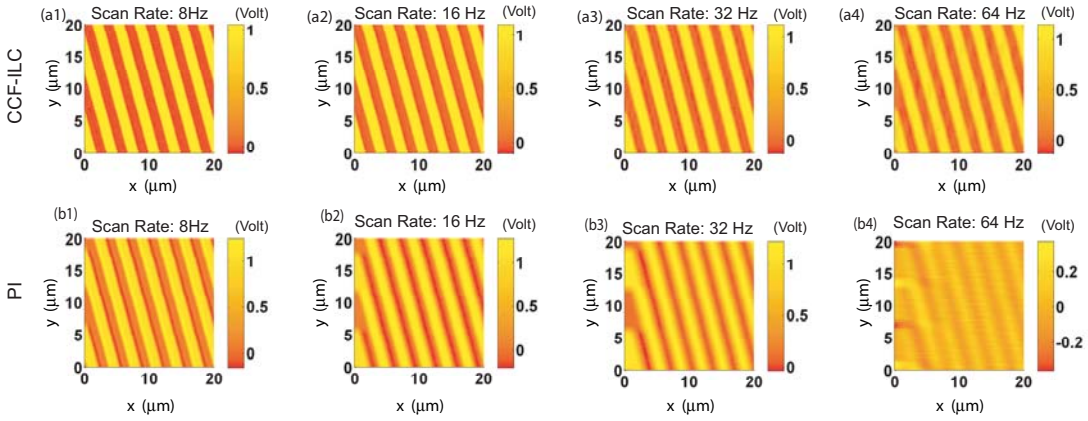

Figure 5.4 Comparison of the sample estimation results by using by using (the upper row) the proposed CCF-ILC approach with that by using (the bottom row) the PI control for four different equivalent scan rates of (a1, b1) 8Hz, (a2, b2) 16Hz, (a3, b3) 32Hz, and (a4, b4) 64Hz. The effective lateral scan range was assumed as 20 μm.

scanlines are compared with the errors obtained by using a PI controller in Fig. 5.3. Note that one flat scanline was added between each scanlines in Fig. 5.3 (a) to allow the batch calculation of the feedforward controller because of the hardware limitation (The feedforward controller was implemented in frequency-domain using fast Fourier transform (FFT)). The PI controller was carefully designed as in [84] and the convergence of the first scanline was also shown in [84]. Then, the 'sample profile' can be estimated by using a sample observer as described in [84]. The obtained sample estimation is compared with that by using the commercial method (along with PI control) in Figs. 5.4, 5.5.

The experimental results show that the proposed CCF-ILC approach improved the AFM z-axis precision positioning when there existed line-to-line sample variation. For the four scan rates, much smaller residual error (i.e., the deflection signal change) was obtained when using the CCF-ILC approach than that when using the PI feedback control only. As shown in Fig. 5.3 (a1), (b1), for 'sample profile' at the equivalent scan rate of 8 Hz, the maximum residual

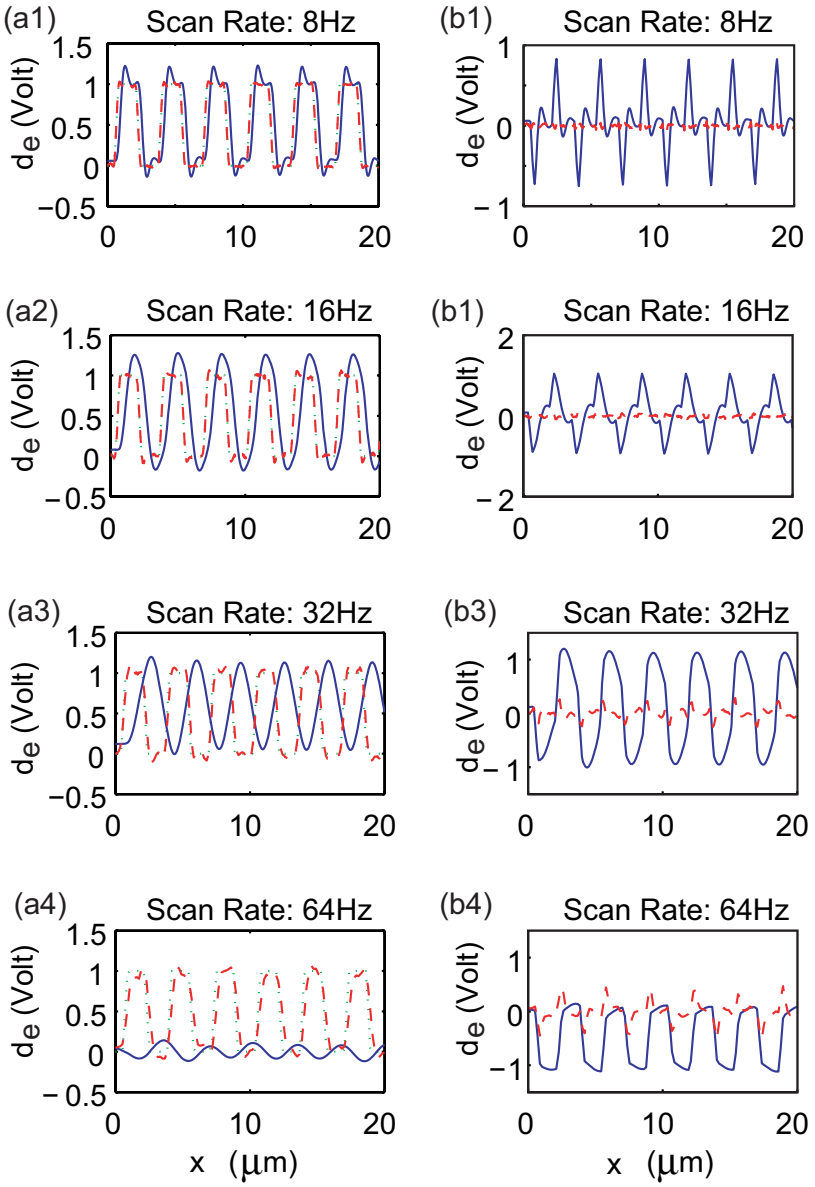

Figure 5.5 Comparison of the sample estimation results of cross section by using the proposed CCF-ILC approach with that by using the PI control for four different equivalent scan rates of (a1, b1) 8Hz, (a2, b2) 16Hz, (a3, b3) 32Hz, and (a4, b4) 64Hz in one scanline imaging, where the left column shows sample estimation; and the right column shows the estimation error. The effective lateral scan range is 20 μ m.

error with the CCF-ILC approach was less than half of that with the PI feedback control only. Particularly, we note that this positioning precision was achieved where there exists relatively large line-to-line sample variation (see Fig. 5.2). Such large reduction of the residual error with the use of the proposed CCF-ILC technique over the PI control was maintained even when the equivalent scan rate was doubled (16 Hz) and tripled (32 Hz) as shown in Fig. 5.3 (a2), (b2), (a3) and (b3). When the 'scan rate' was further increased to 64 Hz, significant frequency components of the disturbance signal moved beyond the feedback bandwidth, thereby larger residual error was generated under the feedback control only. For the same 'scan rate', tracking error was a little smaller than that by using feedback control only, because the main frequency component of sample profile was out of the feedforward bandwidth of the proposed CCF-ILC approach, which was limited by the system noise level. Therefore, by using CCF-ILC approach, the vertical z-axis positioning precision during high-speed scanning can be improved from using feedback control only.

The experimental results also show that the CCF-ILC approach can significantly improve the sample profile estimation over the commercial PI-control approach. When the 'scan rate' was relatively low (8 Hz), the estimated disturbance trajectory (i.e., the estimated sample profile) obtained by the PI control and the CCF-ILC approach were both close to the 'true' sample profile (see Fig. 5.4 (a1) (b1) for the obtained topography imaging and Fig. 5.5 (a1) (b1) for the corresponding cross section plot). However, the estimation error with the use of the CCF-ILC approach was still over 10 times smaller than that with the use of the PI control (see Fig. 5.5 (b1)). When the 'scan rate' was increased, imaging distortion become more and more serious with the use of the PI control, whereas the same imaging quality was maintained with the use of the proposed CCF-ILC approach. As shown in Fig. 5.4, by using the proposed CCF-ILC approach, the edge of the arrays was much clearer than that by using the PI control at the "scan rates" of 8 Hz, 16 Hz and 32 Hz (compare Fig. 5.4 (a1) (a2) and (a3), to (b1) (b2) and (b3), respectively), and relatively good image can still be obtained even when the "scan rate" was increased to 64 Hz. On the contrary, when using the PI control, the image became

significantly fuzzy at the "scan rate" of 16 Hz (Fig. 5.4 (b2)), and the sample feature was almost completely lost at the "scan rate" of 64 Hz (Fig. 5.4 (b4)). Especially, for the equivalent scan rate of 64 Hz, the imaging error was 8 times smaller under the proposed CCF-ILC approach than that under the PI approach (see Fig. 5.5 (a4), (b4)), and the imaging error under the CCF-ILC approach is only 4.4% of the sample profile size. Therefore, the experiment results demonstrate that precise sample estimation can be obtained by using the proposed CCF-ILC approach for high-speed AFM imaging even when there existed significant line-to-line sample variation.

5.5.2 Sample imaging

Next, the proposed CCF-ILC technique was implemented to scan a calibration sample (TGZ02, from MikroMasch) where the nominal pitch size is 3 μm, and the nominal step height is 84 nm. The image area is 20 μm $\times$ 20 μm, and the precision positioning in the lateral x-y scanning was achieved by using the inversion-based iterative control (IIC) approach [54]. It has been shown [54] that this IIC technique can effectively compensate for both the vibrational dynamics and the hysteresis effects simultaneously during high-speed, large-range lateral scanning. In this experiments, less than 1% of the maximum relative tracking error in the lateral scanning was achieved by using the IIC technique for the three different scan rates, 16 Hz, 32 Hz, and 64 Hz (The imaging results of lower scan rate at 8 Hz was not shown). The obtained deflection error signals are compared with those obtained by using the PI control in Fig. 5.6 (the left column is for the total of ten repetitive scanlines, and the right column is for the zoomed-in view of the result on one of the scanline).

The experimental results show that the imaging speed can be significantly improved by using the proposed CCF-ILC approach — much smaller residual error was obtained than that by using the feedback control only. At the scan rate of 16 Hz, the maximum residual error under the CCF-ILC approach was 3 times smaller than that under the PI control, as shown in Fig. 5.6 (a1) (b1). Such large reduction of the residual error by using the proposed CCF-ILC technique over the PI control was maintained even when the equivalent scan rate was doubled

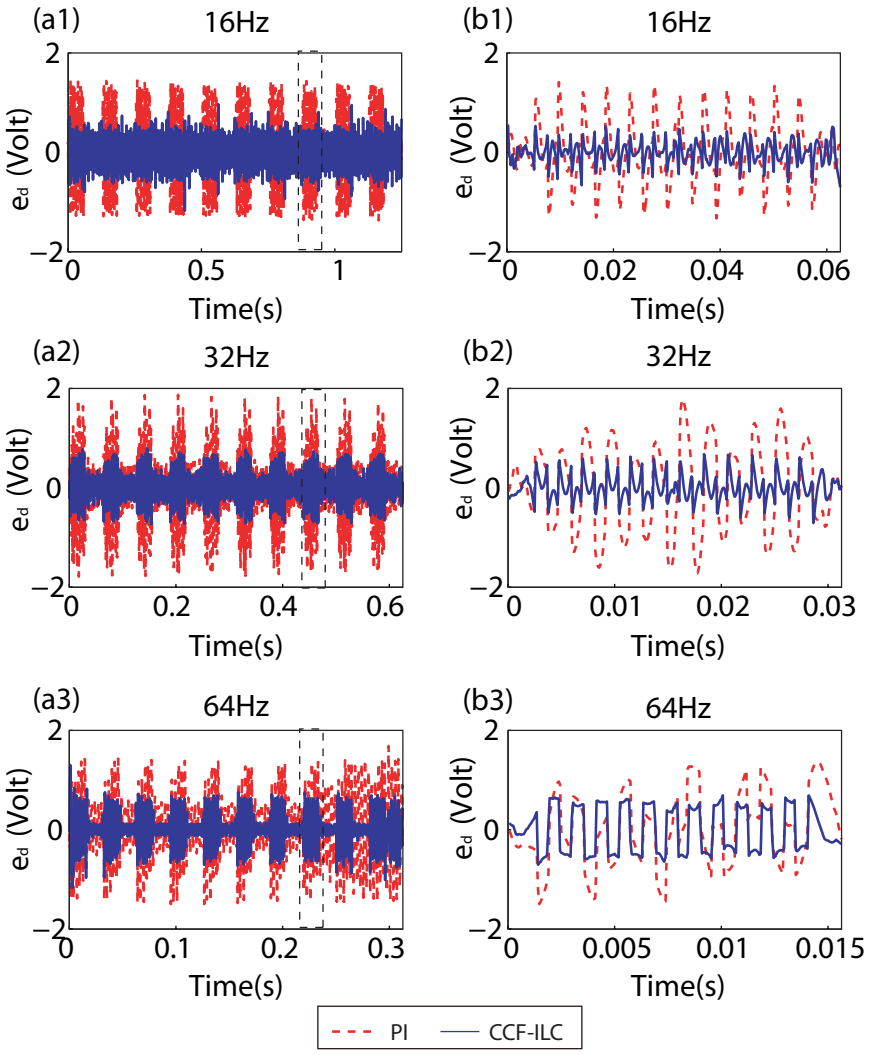

Figure 5.6 Comparison of the deflection error (the residual error) by using the proposed CCF-ILC approach with that by using the PI control for four different equivalent scan rates of (a1, b1) 8Hz, (a2, b2) 16Hz, (a3, b3) 32Hz, and (a4, b4) 64Hz in sample imaging, where the left column shows the total of 10 repeated scan result; and the right column is the zoomed-in view of the one scanline result in the dashed window in the left column. The effective lateral scan range is 20 μ m.

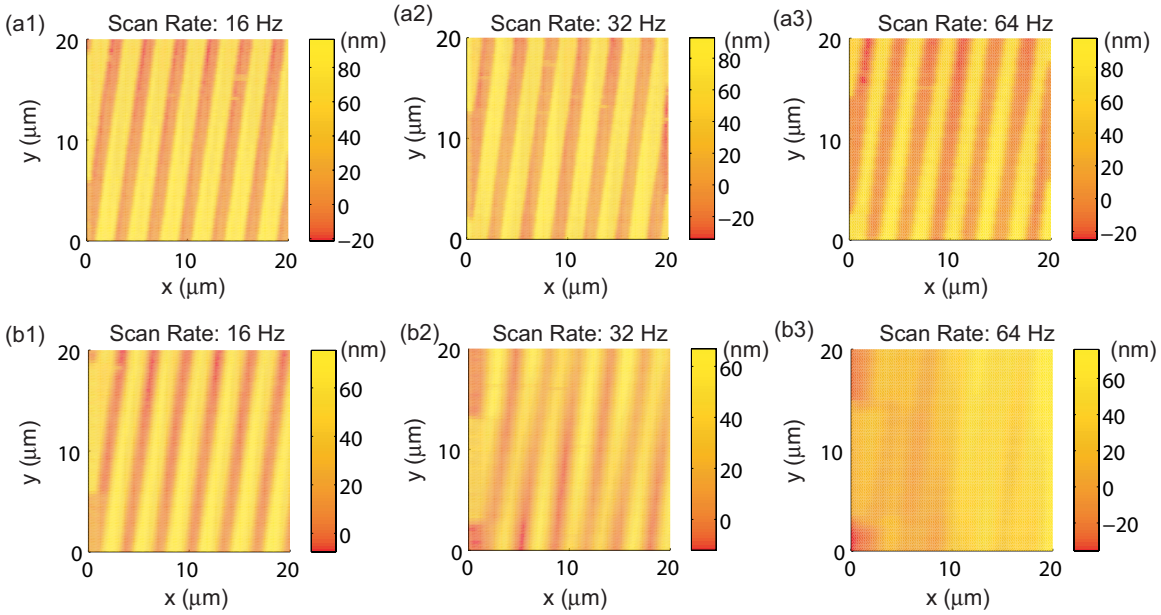

Figure 5.7 Comparison of the sample estimation results by using (the upper row) the proposed CCF-ILC approach with that by using (the bottom row) the PI control for three different equivalent scan rates of (a1, b1) 16Hz, (a2, b2) 32Hz, and (a3, b3) 64Hz. The lateral scan range is 20 μ m.

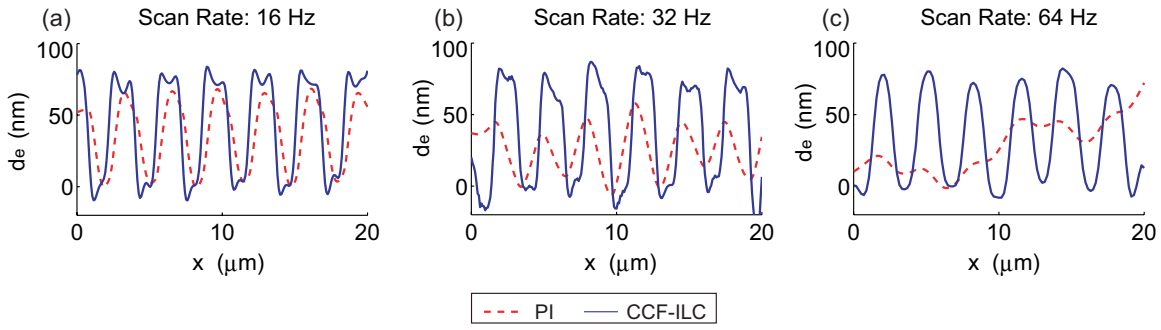

Figure 5.8 Comparison of the sample estimation results (cross section view) by using the proposed CCF-ILC approach with that by using the PI control for three different equivalent scan rates of (a) 16Hz, (b) 32Hz, and (c) 64Hz. The lateral scan range is 20 μm.

(32 Hz) and tripled (64 Hz) as shown in Fig. 5.6 (a2), (b2), (a3) and (b3). It is noted that during the high speed imaging (scan rate at 64 Hz), the reduction of the residual error obtained in the sample imaging was much larger than that in one point imaging experiment. Such a larger reduction was because the surface slope and the x-to-z axis dynamics coupling effect [83, 1] (which did not exist in one-point-imaging case) existed and became more pronounced in the sample imaging. As a result, much larger residual error occurred when using feedback control only. On the contrary, these effects were efficiently compensated for with the use of the proposed CCF-ILC approach. Therefore, the experimental results demonstrated the efficacy of the proposed CCF-ILC approach in improving the AFM imaging speed.

The experimental results also showed that the sample estimation at high-speed can also be significantly improved with the use of the CCF-ILC approach, even when there existed large cross-axis dynamics-coupling effect. The sample estimation results obtained by using the CCF-ILC approach and those by using the PI control approach are compared in Fig. 5.7 for the three different scan rates. Note that the dynamics coupling effect were removed from the sample estimation for the CCF-ILC approach as in [84]. At the scan rate of 16 Hz, the estimated sample profile obtained by using the CCF-ILC approach was close to the true sample profile (the rectangle pitches can be clearly identified), whereas the estimated sample profile by using the PI control showed pronounced sample distortions (the top of the pitches were cornered around instead of being flat, see Fig. 5.7 (a)). As the scan rate increased (to 32 Hz), the estimation error became larger by using the PI control (where not only the top but also the bottom of the pitches were cornered around), while the sample profile can still be relatively well estimated by using the proposed approach. When the scan rate was increased to 64 Hz, the imaging distortion was even more pronounced under the PI control—the basic shape of the sample surface can not be recognized, and large variations occurred among the estimated pitches. On the contrary, by using the CCF-ILC approach, the sample estimation signal was still relatively close to the sample profile. Therefore, the experiment results showed that the proposed CCF-ILC approach can achieve a smaller tracking error as well as a better sample

estimation than those obtained by using the feedback control alone.

5.6 Conclusion

A new CCF-ILC approach was proposed in this chapter to achieve the vertical z-axis precision positioning during AFM-imaging. First, the convergence (stability) of the CCF-ILC law was analyzed for the general case where the line-to-line sample profile variation (i.e., the desired trajectory in general) occurred at each iteration. The conditions for the convergence of the CCF-ILC approach were characterized. Secondly, the CCF-ILC system was designed for repetitively imaging on the same scanline (i.e., with no line-to-line sample variation) as in the authors' recent work. Then the allowable line-to-line sample variation was quantified for the CCF-ILC approach so that the imaging on the rest of the scanlines can be proceeded with no iterations. The performance of the CCF-ILC was discussed by comparing the tracking error with the proposed CCF-ILC technique to that with feedback control only. It was shown that the CCF-ILC approach can improve the tracking even when there existed significant line-to-line sample profile variations. The proposed CCF-ILC control approach was illustrated by implementing it to the z-axis direction control in AFM imaging. Experimental results show that the imaging speed as well as the sample estimation can be significantly improved by using the proposed approach.

CHAPTER 6. Conclusion

The dissertation demonstrated the use of advanced control approaches, e.g. iterative learning control and inversion-based control, to achieve high speed AFM imaging. The main contribution of this dissertation is following

1. Inversion-based iterative learning approach (IIC) was utilized to compensate for both the nonlinear hysteresis and the vibrational dynamics effects of piezo actuator in AFM lateral direction positioning. The convergence of the iterative approach was investigated by capturing the hysteresis and the vibrational dynamics effects with a cascade model consisting of the rate-independent hysteresis at the input followed by the linear dynamics of the piezo actuator. The size of the hysteresis effect and the vibration dynamics variation that can be compensated for by using the IIC method is quantified. The IIC algorithm was also implemented on piezotube actuator of an AFM system to validate the convergence requirement as well as to show that high-speed, large-range lateral direction precision positioning can be achieved.

2. A robust-inversion-based 2DOF control design approach was proposed for output tracking. A novel robust-inversion technique is developed, which, when used as a feedforward control, achieved a guaranteed tracking precision in the presence of bounded dynamics variations from the feedforward control. The bounded feedforward gain-error was then used in the H_∞ robust feedback control to design a robust feedback controller to complement the feedforward control and increase the feedback bandwidth under the robust stability requirements. Therefore, the proposed approach systematically integrated the system-inversion-based feedforward control with the H_∞ robust feedback control to-

gether. The implementation of the proposed method on piezotube actuator of an AFM is presented to show that the proposed approach achieved a larger feedback-bandwidth of the entire system than that by using the regular robust H_∞ design; and high-speed precision output tracking can be achieved by using the proposed robust-inversion-based 2DOF control technique.

3. A CCF-ILC approach was developed to achieve the vertical z-axis precision positioning during AFM-imaging. The convergence of the CCF-ILC approach was analyzed and the conditions for the convergence were characterized. The performance of the CCF-ILC was discussed by comparing the tracking error with the proposed CCF-ILC technique to that with feedback control only, and the allowable line-to-line sample variation was quantified. It was shown that the CCF-ILC approach can improve the tracking even when there existed significant line-to-line sample profile variations. The proposed CCF-ILC control approach was illustrated by implementing it to the z-axis direction control in AFM imaging. Experimental results show that the imaging speed as well as the sample estimation can be significantly improved by using the proposed approach.

Bibliography

[1] S. Tien, Q. Zou, and S. Devasia. Control of dynamics-coupling effects in piezo-actuator for high-speed AFM operation. *IEEE Trans. on Control Systems Technology*, 13(6):921–931, 2005.

[2] Jayati Ghosh and Brad Paden. Pseudo-inverse based iterative learning control for non-linear plants with disturbances. *IEEE conference on Decision and Control*, 11:5206–5212, December 1999.

[3] D. Croft, G. Shedd, and S. Devasia. Creep, hysteresis, and vibration compensation for piezoactuators: Atomic force microscopy application. *ASME Journal of Dynamic Systems, Measurement and Control*, 123(1):35–43, March, 2001.

[4] Kam K. Leang and Santosh Devasia. Design of hysteresis-compensating iterative leaning control for atomic force microscopes. *Mechatronics*, 16:141–158, 2005.

[5] S. Devasia, D. Chen, and B. Paden. Nonlinear inversion-based output tracking. *IEEE Trans. on Automatic Control*, 41(7):930–942, 1996.

[6] Giovanni Marro, Domenico Prattichizzo, and Elena Zattoni. Convolution profiles for right-inversion of multivariable non-minimum phase discrete-time systems. *Automatica*, 38(10):1695–1703, 2002.

[7] Q. Zou, K. K. Leang, E. Sadoun, M. J. Reed, and S. Devasia. Control issues in high-speed AFM for biological applications: Collagen imaging example. *Special Issue on "Advances in Nano-technology Control", Asian Journal Control*, 8(2):164–178, June 2004.

[8] S. Devasia. Should model-based inverse input be used as feedforward under plant uncertainty? *IEEE Trans. on Automatic Control*, 47(11):1865–1871, Nov. 2002.

[9] J. S. Dewey, K. K. Leang, and S. Devasia. Experimental and theoretical results in output-trajectory redesign for flexible structures. *ASME Journal of Dynamic Systems, Measurement and Control*, 120:456–461, Dec. 1998.

[10] Mark Verwoerd, Gjerrit Meinsma, and Theo de Vries. On admissible pairs and equivalent feedback – Youla parameterization in iterative learning control. *Automatica*, 42:2079–2089, 2006.

[11] R. Wiesendanger, editor. *Scanning Probe Microscopy and Spectroscopy*. Cambridge University Press, 1994.

[12] P. Ge and M. Jouaneh. Tracking control of a piezoceramic actuator. *IEEE Trans. on Control Systems Technology*, 4(3):209–216, May 1996.

[13] Ram Venkataraman Iyer, Xiaobo Tan, , and P. S. Krishnaprasad. Approximate inversion of the preisach hysteresis operator with application to control of smart actuators. *IEEE Trans. on Automatic Control*, 50(6):798–810, 2005.

[14] JinHyoung Oh and Dennis S. Bernstein. Semilinear duhem model for rate-independent and rate-dependent hysteresis. *IEEE Trans. on Automatic Control*, 50:631–645, 2005.

[15] R. C. Barrett and C. F. Quate. Optical scan-correction system applied to atomatic force micropscopy. *Review of Scientific Instruments*, 62:1393–1399, 1991.

[16] C. Rotsch, K. Jacobson, and M. Radmacher. Dimensional and mechanical dynamics of active and stable edges in motile fibroblasts investigated by using atomic force microscopy. *Proc. Natl. Acad. Sci. USA*, 96:921–926, Feb. 1999. Cell Biology.

[17] S. Salapaka, A. Sebastian, J. P. Cleveland, and M. V. Salapaka. High bandwidth nano-positioner: A robust control approach. *Review of Scientific Instruments*, 73(9):3232–3241, Sept., 2002.

[18] G. Schitter, P. Menold, H.F. Knapp, F. Allgower, and A. Stemmer. High performance feedback for fast scanning atomic force microscopes. *Review of Scientific Instruments*, 72(8):3320–3327, 2001.

[19] A. Sebastian and S. Salapaka. Design methodologies for robust nano-positioning. *IEEE Trans. on Control Systems Technology*, 13(6):868–876, 2005.

[20] Q. Zou and S. Devasia. Preview-based optimal inversion for output tracking: Application to scanning tunneling microscopy. *IEEE Trans. on Control Systems Technology*, 12(3):375–386, May 2004.

[21] J. A. Main, E. Garcia, and D. V. Newton. Precision position control of piezoelectric actuators using charge feedback. *AIAA, Journal of Guidance Control, and Dynamics*, 18(5):1068–1073, 1995.

[22] A. J. Fleming and S. O. R. Moheimani. Sensorless vibration suppression and scan compensation for piezoelectric tube nanopositioners. *IEEE Trans. on Control Systems Technology*, 14(1):33–44, 2006.

[23] Qingze Zou, Clint Vander Giessen, Joseph Garbini, and Santosh Devasia. Precision tracking of driving waveforms for inertial reaction devices. *Review of Scientific Instruments*, 76(1):23701–23709, 2005.

[24] I. Mayergoyz. *Mathematical Models of Hysteresis*. New York:Springer-Verlag, 1991.

[25] George Zames. On the input-output stability of time-varying nonlinear feedback systems part I: Conditions derived using concepts of loop gain, conicity, and positivity. *IEEE Trans. on Automatic Control*, AC-11(2):228–238, 1962.

[26] Walter Rudin. *Real and Complex Analysis*. McGraw-Hill, New York, third edition, 1966.

[27] Claude Gasquet and Patrick Witomski. *Fourier Analysis and Applications: Filtering, Numerical Computation, Wavelets*. Springer, 1999.

[28] AG. Khurshudov, K. Kato, and H. Koide. Wear of the AFM diamond tip sliding against silicon. *WEAR*, 203:22–27, 1997.

[29] Manfred Radmacher. Measuring the elastic properties of biological samples with the AFM. *IEEE Engineering in Medicine and Biology Magazine*, pages 47–57, March/April 1997.

[30] Ram V. Iyer and Matthew E. Shirley. Hysteresis parameter identification with limited experimental data. *IEEE Trans. on Magnetics*, 40(5):3227–3239, 2004.

[31] M.-S. Tsai and J.-S. Chen. Robust tracking control of a piezoacuator using a new approximate hysteresis model. *ASME Journal of Dynamic Systems, Measurement and Control*, 125:96–102, March 2003.

[32] Ying Wu and Qingze Zou. Iterative control approach to compensate for the hysteresis and the vibrational dynamics effects of piezo actuators. In *Proceedings of American Control Conference*, pages 424–429, Minneapolis, June 2006.

[33] D. Kwon and W. J. Book. A time-domain inverse dynamic tracking control of a single-link flexible manipulator. *ASME Journal of Dynamic Systems, Measurement and Control*, 116(2):193–200, June 1994.

[34] Q. Zou and S. Devasia. Preview-based stable-inversion for output tracking of nonlinear nonminimum-phase systems: The VTOL example. *Automatica*, 43(1):117–127, 2007.

[35] Saif A. Al-Hiddabi and N. Harris McClamroch. Aggressive longitudinal aircraft trajectory tracking using nonlinear control. *Journal of Guidance, Control, and Dynamics*, 25(1):26–32, 2002.

[36] W. Yim and S. N. Singh. Nonlinear inverse and predictive end point trajectory control of flexible macro-micro manipulators. *ASME Journal of Dynamic Systems, Measurement and Control*, 119(3):412–420, Sept. 1997.

[37] Dante C. Youla and Joseph J. Bongiorno Jr. A feedback theory of two-degree-of-freedom

optimal wiener-hopf design. *IEEE Trans. on Automatic Control*, TAC-30(7):652–665, 1985.

[38] Emmanuel Prempain and Ian Postlethwaite. Feedforward control: a full-information approach. *Automatica*, 37(1):17–28, 2001.

[39] Duncan McFarlane and Keith Glover. A loop-shaping design procedure using h_∞ synthesis. *IEEE Trans. on Automatic Control*, 37(6):759–769, 1992.

[40] J. W. Howze and S. P. Bhattacharyya. Robust tracking, error feedback, and two-degree-of-freedom controllers. *IEEE Trans. on Automatic Control*, 42(7):980–983, 1997.

[41] Carsten Scherer, Pascal Gahinet, , and Mahmoud Chilali. Multiobjective output-feedback control via lmi optimization. *IEEE Trans. on Automatic Control*, 42(7):896–911, 1997.

[42] I. Yaesh and U. Shaked. Two-degree-of-freedom h_∞-optimization of multivariable feedback systems. *IEEE Trans. on Automatic Control*, 36(11):1272–1275, 1991.

[43] G. Schitter, A. Stemmer, and F. Allgower. Robust 2DOF-control of a piezoelectric tube scanner for high-speed atomic force microscopy.

[44] L. Qiu and E. J. Davison. Performance limitations of non-minimum phase systems in the servomechanism problem. *Automatica*, 29:337–349, March 1993.

[45] Sigurd Skogestad and Ian Postlethwaite. *Multivariable Feedback control: Analysis and Design*. Wiley, New York, second edition, 2005.

[46] S. Devasia and B. Paden. Stable inversion for nonlinear nonminimum phase time-varying systems. *IEEE Trans. on Automatic Control*, 43(2):283–288, Feb. 1998.

[47] Gunter Stein. Respect the unstable. *IEEE control system magazine*, 23(4):1225, 2003.

[48] Q. Zou and S. Devasia. Preview-based stable-inversion for output tracking of linear systems. *ASME Journal of Dynamic Systems, Measurement and Control*, 121(1):625–630, Dec. 1999.

[49] Thomas Kailath. *Linear Systems*. Prentice-Hall, Inc., Englewood Cliffs, N.J., 1980.

[50] M. Browning, K. Wadu-Mesthrige, V. Hari, and G.-Y. Liu. AFM study of specific antigen-antibody binding. *Langmuir*, 12:343–350, 1997.

[51] Gi Hun Seong, Tomohisa Niimi, Yasuko Yanagida, Eiry Kobatake, and Masuo Aizawa. Single-molecular AFM probing of specific DNA sequencing using reca-promoted homologous pairing and strand exchange. *Analytical Chemistry*, 72:1288–1293, 2000.

[52] D. P. Allison, P. S. Kerper, M. J. Doktycz, T. Thundat, P. Modrich, F. W. Larimer, D. K. Johnson, P. R. Hoyt, M. L. Mucenski, and R. J. Warmack. Mapping individual cosmid DNAs by direct AFM imaging. *Genomics*, 41:379–384, 1997.

[53] Guangyong Li, Ning Xi, Mengmeng Yu, and Wai-Keung Fung. Development of augmented reality system for AFM-based nanomanipulation. *IEEE/ASME Transactions on Mechatronics*, 9(2):358–365, 2004.

[54] Ying Wu and Qingze Zou. Iterative control approach to compensate for both the hysteresis and the dynamics effects of piezo actuators. *IEEE Trans. on Control Systems Technology*, 15:936–944, 2007.

[55] J. K. H. Hörber1 and M. J. Miles. Scanning probe evolution in biology. *Science*, 302:1002–1005, 2003.

[56] Richar D. Piner, Jin Zhu, Feng Xu, Seunghun Hong, and Chad A. Mirkin. "Dip-Pen" nanolithography. *Science*, 283:661–663, Jan. 1999.

[57] RICARDO GARCA, ROBERT MAGERLE, and RUBEN PEREZ3. Nanoscale compositional mapping with gentle forces. *Nature Materials*, 6:405–411, June 2007.

[58] Chun M. Chew, Radoljub I. Ristic, Robert D. Dennehy, and James J. De Yoreo. Crystallization of paracetamol under oscillatory flow mixing conditions. *Crystal Growth & Design*, 4:1045–1052, 2004.

[59] Osamah M. El Rifai and Kamal Youcef-Toumi. Trade-offs and performance limitations in mechatronic systems: A case study. *Annual Reviews in Control*, 28(2):181–192, 2004.

[60] Shuiqing Hu and Arvind Raman. Chaos in atomic force microscopy. *Physical Review Letters*, 96(3):0361072, 2006.

[61] H. Lin, D. O. Clegg, and R. Lal. Imaging real-time proteolysis of single collagen i molecules with an atomic force microscope. *Biochemistry*, 38:9956–9963, 1999.

[62] F. El Feninat, T.H. Ellis, E. Sacher, and I. Stangel. A tapping mode AFM study of collapse and denaturation in dentinal collagen. *Dental Materials*, 17:284–288, 2001.

[63] M. J. Rost, D. A. Quist, and J.W.M. Frenken. Grains, growth, and grooving. *Physical Review Letters*, 91:026101–026106, 2003.

[64] Peter G. Vekilov. Self-assembly of apoferritin molecules into crystals: thermodynamics and kinetics of molecular level processes. *Progress in Crystal Growth and Characterization of Materials*, 45:175–199, 2002.

[65] Terry A. Land and James J. De Yoreo. The evolution of growth modes and activity of growth sources on canavalin investigated by in situ atomic force microscopy. *Journal of Crystal Growth*, 208:623–637, 2000.

[66] Y. Xia and G. M. Whitesides. Soft lithography. *Angewandte Chemie, International Edition*, 37:550–575, 1998.

[67] Andrew D. Pris and Marc D. Porter. Nanoparticle coding: Size-based assays using atomic force microscopy. *Langmuir*, 20:6969–6973, 2004.

[68] Guanghua Wu, Ram H. Datar, Karolyn M. Hansen, Thomas Thundat, Richard J. Cote, and Arun Majumdar. Bioassay of prostate-specific antigen (psa) using microcantilevers. *Nature: Biotechnology*, 19:856–860, 2001.

[69] T. Ando, N. Kodera, E. Takai, D. Maruyama, K. Saito, and A. Toda. A high-speed atomic force microscope for studying biological macromolecules. *Proceedings of the National Academy of Sciences of the USA*, 98(22):12468–12472, Oct., 2001.

[70] M. J. Rosta, L. Crama, P. Schakel, E. van Tol, G. B. E. M. van Velzen-Williams, C. F. Overgauw, H. ter Horst, H. Dekker, B. Okhuijsen, M. Seynen, A. Vijftigschild, P. Han, A. J. Katan, K. Schoots, R. Schumm, W. van Loo, T. H. Oosterkamp, and J. W. M. Frenken. Scanning probe microscopes go video rate and beyond. *Review of Scientific Instruments*, 76:53710–53718, 2005.

[71] Andrew D. L. Humphris, Jamie K. Hobbs, and Mervyn J. Miles. Ultrahigh-speed scanning near-field optical microscopy capable of over 100 frames per second. *Applied Physics Letters*, 83(1):6–8, 2003.

[72] M. B. Viani, T. E. Schaffer, Ami Chand, M. Rief, H. E. Gaub, and Hansma P. K. Small cantilever for force spectroscopy of single molecules. *Journal of Applied Physics*, 86(4):2258–2262, 1999.

[73] T. Sulchek, R. Hsieh, J. D. Adams, G. G. Yaralioglu, S. C. Minne, C. F. Quate, J. P. Cleveland, A. Atalar, and D. M. Adderton. High-speed tapping mode imaging with active q control for atomic force microscopy. *Applied Physics Letters*, 76(11):1473–1475, March 2000.

[74] G. Schitter, K.J. Astrom, B.E. DeMartini, P.J. Thurner, K.L. Turner, and P.K. Hansma. Design and modeling of a high-speed afm-scanner. *IEEE Trans. on Control Systems Technology*, 15(5):906–915, 2007.

[75] Ying Wu and Qingze Zou. Robust-inversion-based 2DOF-control design for output tracking: Piezoelectric actuator example. In *IEEE conference on Decision and Control*, pages 2451–2457, New Orleans, LA, Dec., 2007 2007.

[76] M. Srinivasa Salapaka, Tathagata De, and Sebastian Abu. A robust control based solution

to the sample-profile estimation problem in fast atomic force microscopy. *International Journal of Robust and Nonlinear Control*, 15:821–837, 2005.

[77] Hendrik Rothe, Dorothee Hueser, Andree Kasper, and Thomas Rinder. Investigations of smooth surfaces by measuring the brdf with a stray light sensor in comparison with PSD curves evaluated from topography of large AFM scans. pages 112–120, San Jose, CA, Janurary 1999. SPIE.

[78] Matt J. Kipper, Elizabeth Shen, Amy Determan, and Balaji Narasimhan. Design of an injectable system based on bioerodible polyanhydride microspheres for sustained drug delivery. *Biomaterials*, 23(4405-4412), 2002.

[79] Shinichi Machida and Tomonobu Nakayama. Temperature-dependent growth of smooth DNA film. *Japanese Journal of Applied Physics, Part 1: Regular Papers and Short Notes and Review Papers*, 45(6):5183–5185, 2006.

[80] Osamah M. El Rifai and Kamal Youcef-Toumi. Dynamics of atomic force microscopes: Experiments and simulations. Scotland, September 2002. IEEE.

[81] K. Zhou, J. Doyle, and K. Glover. *Robust and optimal control*. Prentice Hall, 1995.

[82] Jianwu Li and Tsu-Chin Tsao. Robust performance repetitive control systems. *Journal of Dynamic Systems, Measurement, and Control*, 123:330–337, September 2001.

[83] O. M. El Rifai and K. Youcef-Toumi. Coupling in piezoelectric tube scanners used in scanning probe microscopes. In *Proceedings of the American Control Conference*, pages 3251–3255, 2001.

[84] Ying Wu, Qingze Zou, and Chanmin Su. A current cycle feedback iterative learning control approach to AFM imaging. In *Proceedings of American Control Conference*, pages 2040–2045, Seattle, Washington, June 2008.

[85] G. Binnig, C. F. Quate, and Ch. Gerber. Atomic force microscope. *Physical Review Letters*, 56(9):930–934, 1986.

[86] Ki-Bum Lee, So-Jung Park, Chad A. Mirkin, Jennifer C. Smith, and Milan Mrksich. Protein nanoarrays generated by dip-pen nanotithography. *Science*, 295(5560):1702–1705, 2002.